Coversheet for EarthArXiv

SOLUBILITY PRODUCT CONSTANTS FOR NATURAL DOLOMITE (0-200°C) THROUGH A GROUNDWATER-BASED APPROACH USING THE USGS PRODUCED WATER DATABASE – PART A

Authors
Hamish Robertson, University of Bristol, UK - corresponding author:
h.robertson@bristol.ac.uk, twitter - @hamish95
Fiona Whitaker, University of Bristol, UK
Hilary Corlett, Grant MacEwan University, Canada
Cathy Hollis, Manchester University, UK - @carbonatesUoM

SOLUBILITY PRODUCT CONSTANTS FOR NATURAL DOLOMITE (0-200°C) THROUGH A GROUNDWATER-BASED APPROACH USING THE USGS PRODUCED WATER DATABASE – PART A

H.A. ROBERTSON*, H. CORLETT**, C. HOLLIS***, F.F. WHITAKER*

ABSTRACT. The calculation of a reliable temperature dependent dolomite solubility product constant ($K_{sp°-dol}$) has been the subject of much research over the last 70 years. This study evaluates $\log_{10}(^aCa^{2+}/^aMg^{2+})$ using PHREEQC (Pitzer approach) for a screened subset (n=11,480) of formation waters in the U.S. Geological Survey National Produced Waters Geochemical Database V2 (PWGD), an extensive inventory of 165,960 formational waters from a range of sedimentary lithologies in North America up to 6.6 km depth (Blondes and others, 2016). Through extensive ground-truthing against datasets sourced from Texas Gulf Coast basin and the Mississippi Salt Dome basin we establish that both the geochemical data from the PWGD and a new geothermal model of the US that is used to determine temperatures at-formation-depth to be reliable data sources.

The vast majority (at least 90%) of PWGD samples have $\log_{10}(^aCa^{2+}/^aMg^{2+})$-temperature values that are interpreted to be indicative of calcite-dolomite equilibrium and controlled by bulk mineral equilibria rather than Mg-calcite surface phases. Using statistical models with different parameterizations (different Maier-Kelly formulas, mixed-effects models with various random effects and linear models) $\log_{10}(^aCa^{2+}/^aMg^{2+})$ values (outcome variable) are regressed against temperature (fixed effect) calculating $K_{sp°-dol}$ between 0-200°C using the well constrained calcite solubility product ($K_{sp°-cal}$).

Local effects that modify $\log_{10}(^aCa^{2+}/^aMg^{2+})$ values are evaluated through the addition of random effects to the mixed model which improves the statistical reliability of the $K_{sp°-dol}$ estimate and enables the determination of $K_{sp°-dol}$ for local dolomite phases. The nature of these local effects is open to interpretation, but we suggest the primary influence on $\log_{10}(^aCa^{2+}/^aMg^{2+})$ values is the stoichiometry of the equilibrium dolomite phase within individual fields that systematically modifies $\log_{10}(^aCa^{2+}/^aMg^{2+})$ values. We discount the influence on $\log_{10}(^aCa^{2+}/^aMg^{2+})$ values from the ionic strength of the solution, the equilibration with anhydrite and chlorite group minerals, the illitization of smectite and albitization of feldspar.

For the dolomite solubility equation;

$$CaMg(CO_3)_{2\,(s)} \leftrightarrow Ca^{2+}_{\,(aq)} + Mg^{2+}_{\,(aq)} + 2CO_3^{\,2-}_{\,(aq)} \qquad (1)$$

the mixed-effects model chosen as most representative yields a $pK_{sp°-dol}$ ($\log_{10}K_{sp°-dol}$);

$$pK_{sp\text{-}dol} = 1.47545 \times 10^1 - 6.24959 \times 10^{-2} \cdot T(K) - 3.99350 \times 10^3 \cdot \frac{1}{T(K)} \quad (2)$$

At 25°C $pK_{sp°\text{-}dol} = $ -17.27±0.35, which is close to prior estimates including the most recent experimental value reported by Bénézeth and others, 2018 ($pK_{sp°\text{-}dol} = $ -17.19±0.3). This validates this study's approach and enables conclusions to be drawn via a meta-analysis of a contaminated, though expansive dataset.

INTRODUCTION

The solubility product constant is defined as 'the product of the ion activities raised to appropriate powers of an ionic solute in its saturated solution, expressed with due reference to the dissociation equilibria involved and the ions present' (McNaught, 1997). Ideally the solubility product should be determined analytically using a saturated solution under the temperature/pressure conditions for which the constant is desired (Hefter and Tomkins, 2003). However, even with high degrees of supersaturation, it has proved difficult to unequivocally precipitate well-ordered, stoichiometric dolomite near standard state conditions (25°C, 1 atm) that correspond with conditions at which significant volumes of dolomite are thought to have formed (Land, 1998; Warren, 2000). This necessitates an extrapolation from higher temperatures, where equilibrium is achieved within the timescale of laboratory experiments, using Maier-Kelley regressions (Maier and Kelley, 1932). Whilst pragmatic, this approach suffers from increased uncertainty for conditions outside the experimental range.

We present a review of the experimental complexities in evaluating $K_{sp°\text{-}dol}$. An alternative to the experimental method for determining $pK_{sp°\text{-}dol}$ is the groundwater method, which assumes calcite-dolomite equilibrium has been attained based on the substantial residence times of subsurface fluids. Evaluation of $K_{sp°\text{-}dol}$ from the perspective of either dolomite or calcite-dolomite equilibrium has significant implications for both the experimental and groundwater methods. For the calcite-dolomite system we review impacts on the evaluation of $K_{sp°\text{-}dol}$ from variations in bulk thermodynamics, including stoichiometry and ordering, and surface complexation.

This study determines the solubility constant by evaluating $\log_{10}(^aCa^{2+}/^aMg^{2+})$-temperature relationships using the groundwater method for a subset (n=11,480) of fluids from the USGS produced water database. Deviations from the average value are interpreted to reflect variations in the composition of the equilibrium dolomite phase. Temperatures at-formation-depth are estimated by interpolating and merging subsurface geothermal gradients from the SMU Heatflow database (Blackwell and others, 2011) and mean annual land surface temperatures across North America (Bechtel, 2015). The thermal conditions under which most sedimentary dolomites form overlap with the range of temperatures for which this study proposes a dolomite solubility product constant (0-200 °C) suggesting a wide applicability for this meta-analysis.

SUMMARY OF PAST WORK

The Ca-Mg-CO₂-H₂O-Calcite-Dolomite System

There are two dominant mechanisms through which dolomite forms. The first is primary precipitation from a dolomite-supersaturated fluid;

$$CaMg(CO_3)_{2\,(s)} \leftrightarrow Ca^{2+}_{\,(aq)} + Mg^{2+}_{\,(aq)} + 2CO_3^{2-}_{\,(aq)} \quad (3)$$
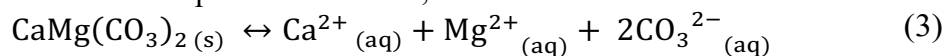
with the solubility product constant for dolomite $K_{sp°\text{-}dol}$;

$$K_{sp°\text{-}dol} = (aCa^{2+})(aMg^{2+})\left(aCO_3^{2-}\right)^2 \quad (4)$$

Primary dolomites precipitated from solution in the absence of a calcite buffer are found in pore spaces of sandstone lithologies (Spötl and Pitman, 1998), in metamorphic rocks (Bucher and Grapes, 2011) and as dolocretes (Khalaf, 2007). In natural systems primary dolomite is much less volumetrically significant than secondary (diagenetic) dolomite which is mostly found replacing limestones (Warren, 2000). Secondary dolomite forms via a dissolution-reprecipitation mechanism where a Mg-rich fluid enters a calcite bearing formation, calcite dissolves, the fluid becomes dolomite supersaturated and precipitates secondary dolomite;

$$2CaCO_{3(s)} + Mg^{2+}_{(aq)} \leftrightarrow CaMg(CO_3)_{2(s)} + Ca^{2+}_{(aq)} \qquad (5)$$
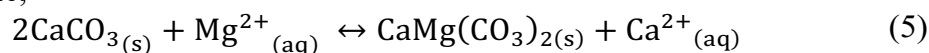
The molar ratio of dissolved calcite to precipitated dolomite is a function of both the solubility and stoichiometry of all equilibrium solid phases (including any common-ion effects), and the unbuffered original fluid composition (particularly aCa^{2+}, aMg^{2+} and aCO_3^{2-}). Calcite-dolomite equilibrium exists for given conditions at a unique $\log_{10}(aCa^{2+}/aMg^{2+})$ which is directly related to $K_{sp°-dol}$ through the relatively well-constrained $K_{sp°-cal}$. Equation (5) can be rewritten as simultaneous solubility equations for the dissolution of dolomite (eq 3) and of calcite;

$$CaCO_{3(s)} \leftrightarrow Ca^{2+}_{(aq)} + 2CO_3^{2-}_{(aq)} \qquad (6)$$
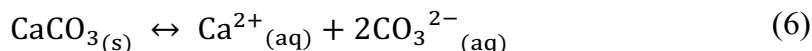
with the solubility product constant of equation (6) expressed in terms of ion activities;

$$(aCa^{2+})(aCO_3^{2-}) = K_{sp°-cal} \qquad (7)$$

The three phase (calcite-dolomite-solution) equilibrium (eq 5) can be stated in terms of solubility constants;

$$\frac{K_{sp°-dol}}{K_{sp°-cal}^2} = \frac{aMg^{2+}}{aCa^{2+}} = K_{sp°-dz} \qquad (8)$$

which can be rearranged to determine $pK_{sp°-dol}$;

$$pK_{sp°-dol} = 2\,pK_{sp°-cal} - p\left(\frac{aCa^{2+}}{aMg^{2+}}\right) \qquad (9)$$

Improvements in estimates of $K_{sp°-cal}$, and to a lesser extent ion activity models, have led to significant refinements of $K_{sp°-dol}$. For example, early work by Hsu (1963) estimated $pK_{sp°-dol}$ to be -16.69 using a $K_{sp°-cal}$ of 5.1 x 10^{-9} (Garrels and Drever, 1952). Recalculating (supplementary table 1) the data from Hsu (1963) using a $K_{sp°-cal}$ from SUPCRT92 (table 1; slop07.dat database - Johnson and others, 1992) of 3.31 x 10^{-9} ($pK_{sp°-cal}$=-8.48) results in a very substantial change in the $pK_{sp°-dol}$, which is determined to be -17.07. Several studies have recalculated $pK_{sp°-dol}$ values using different reference thermodynamic data and the reviews and updates by Sherman and Barak (2000) and Bénézeth and others (2018) form the basis for this studies review of $K_{sp°-dol}$ values (supplementary table 2). Utilizing $K_{sp°-cal}$ to determine $K_{sp°-dol}$ from the perspective of calcite-dolomite equilibrium has been employed for both experimental studies (Rosenberg and Holland, 1964; Baker and Kastner, 1981; Morrow and others, 1994; Usdowski, 1994; see 'Solubility (experimental)' supplementary table 2) and groundwater studies (Hsu, 1963; Barnes and Back, 1964; Hyeong and Capuano, 2001; Vespasiano and others, 2014; Blasco and others, 2018; see 'Solubility (groundwater)' supplementary table 2).

Complicating matters, Möller and De Lucia (2020) argue that because calcite and dolomite dissolve and precipitate incongruently, then $\log_{10}(aCa^{2+}/aMg^{2+})$ values and by extension equation (9), cannot be used to determine the thermodynamic properties of either

bulk mineral as the solution is only at equilibrium with the outermost surface layer of the carbonate phase. Möller and De Lucia (2020) state that the equilibrium is maintained between non-stoichiometric magnesian calcite and calcian dolomite surface phases;

$$2Ca_yMg_{1-y}CO_{3(s)} + (2y-x)Mg^{2+}_{(aq)} \tag{10}$$
$$\leftrightarrow Ca_xMg_{(2-x)}(CO_3)_{2(s)} + (2y-x)Ca^{2+}_{(aq)}$$
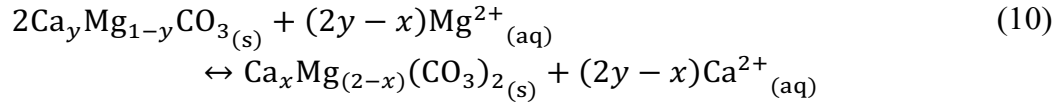
such that the $K_{sp°-dol}$ for the non-stoichiometric dolomite surface phase can be defined as;

$$pK_{sp°-dol_x} = 2\,pK_{sp°-cal_y} - (2y-x)p\left(\frac{aCa^{2+}}{aMg^{2+}}\right) \tag{11}$$

Assuming that the composition of neither surface carbonate phase is known the use of a single value of $\log_{10}(^aCa^{2+}/^aMg^{2+})$ generates an inherently non-unique solution. Bulk mineral calcite and dolomite compositions deviating from ideality pose a similar, but also potentially larger problem. For equations (3 and 10) there is an additional third unknown, the order of the dolomite phase, which is associated with variations in mineral solubility/composition and can buffer $\log_{10}(^aCa^{2+}/^aMg^{2+})$ values. We critically review the present understandings of the potential contribution to solution chemistry from variations in the bulk minerals and surface phases.

Dolomite Ordering and Stoichiometry

Ordering.—The crystallographic structure of ideal dolomite consists of alternating layers of covalently bonded Ca^{2+}, Mg^{2+} and $CO_3{}^{2-}$ ions (fig. 1) (Gregg and others, 2015; Deelman, 2003 *and references therein*). The level of homogeneity within individual cation monolayers is described as the degree of characteristic (substitutional) order (s) for the dolomite phase, with unity representing total order ($s = 1$) and zero total disorder ($s = 0$). The different sizes and Coloumbic attraction profiles of Ca^{2+} and Mg^{2+} ions mean for disordered locations of either ion this results in thermodynamically unfavourable tilting and rotation of adjacent carbonate anions, straining the lattice structure (Althoff, 1977; Deelman, 2003; Antao and others, 2004).

There exists a dynamic equilibrium where cations are constantly swapping locations though overall ordering remains constant. This is the mean-field assumption (ordering parameter homogeneity across an infinite lattice) that is the basis of the Bragg-Williams model (Bragg and Williams, 1934; Chaikin and others, 1995) seminally applied to dolomite by Navrotsky and Loucks (1977). The Bragg-Williams model enables both thermodynamic and kinetic components of dolomite ordering to be considered. Order (s) is described by the relationship (eq 3, Navrotsky and Loucks, 1977);

$$s = \tanh\left(\frac{T_c s}{T}\right) = \tanh\left(\frac{Ws}{2RT}\right) \tag{12}$$

where R is the gas constant and W is an energy parameter constant (eq 4, Navrotsky and Loucks, 1977);

$$W = 2RT_c \tag{13}$$

Higher temperatures decrease the difference in the potential energy between any two sites and the locations of Ca^{2+} and Mg^{2+} ions tend toward randomness, with the probability of an ion occupying a lattice location proportional to overall stoichiometry. As energy is absorbed through disordering, the enthalpy of disorder (ΔH_{dis}) is positive (eq 5, Navrotsky and Loucks, 1977);

$$\Delta H_{dis} = H(s=s) - H(s=1) = \frac{1}{4}W(1-s^2) \tag{14}$$

such that the energy required for $s = 0$ is $\frac{1}{2}W$ per mole $CaMg(CO_3)_2$ (Navrotsky and Loucks, 1977). Disorder increases up to the critical temperature (T_c = 1373K-1473K, Goldsmith and Heard, 1961; Luth, 2001; Antao and others, 2004) whereupon there is total disorder ($s \rightarrow 0$ as $T \rightarrow T_c$; fig. 2). The loss of XRD-peaks (lattice-plane reflections) 101, 015 and 021 at T_c is also interpreted to reflect a second-order phase change to very-high magnesium calcite associated with a space group transformation from $R\bar{3}$ (dolomite) to $R\bar{3}c$ (calcite) (Antao and others, 2004; Gregg and others, 2015). Based on solutions to equation (12) derived by Chaikin and others (1995), for the Bragg-Williams model well-ordered dolomite ($s \geq 0.96$) is the most stable state at temperatures $\leq 500°C$ (fig. 2).

For a synthetic ideal dolomite with a T_c of 1473K (Goldsmith and Heard, 1961), Helgeson and others (1978) determined the enthalpy of complete disordering (ΔH°_{dis}) at reference state conditions to be 12.25kJ mol^{-1}, whilst Navrotsky and others (1999) determine the average ΔH°_{dis} for a suite of dolomites (natural and synthetic) is even higher at 33 ± 6 kJ mol^{-1}. High enthalpies of disorder are interpreted to contribute to substantial differences in the reactivity (solubility) of dolomite, though only for reactions occurring at temperatures >500°C where significant disorder occurs (Helgeson and others, 1978).

Helgeson and others (1978) suggested the thermodynamics of natural dolomites, that have (metastable) cation disorder acquired at low-temperatures, could be approximated by extrapolating high-temperature measurements of disorder to reference state conditions; this yielded pK$_{sp°-dol}$ values (25°C) of -18.14 and -16.60 for ordered and disordered dolomite phases respectively (supplementary table 2). Helgeson and others (1978) observed that prior estimates of pK$_{sp°-dol}$ ranged from -16.4 to -19.3, though most were close to -17 (see supplementary table 2) and interpreted that this value corresponded to a partially ordered dolomite with an s of 0.7. Helgeson and others (1978)'s ordered, disordered and naturally-ordered ($s = 0.7$) dolomite phases are included in a number of thermodynamic databases valid between 0-300°C, particularly those derived from SLOP databases (Shock and Helgeson, 1988). Most thermodynamic datasets are in some way derived from the SLOP databases including EQ3/6 which is the source of many TOUGHREACT and PHREEQC compatible databases and slop07.dat which, in conjunction with SUPCRT92, generates the solubility data for the disordered and ordered dolomite phases used by this study (Wolery and others, 1990; Parkhurst and Appelo, 1999; Xu, 2008). The disordered, natural and ordered dolomite phases have been extensively used in a variety of simulations (André and others, 2007; Whitaker and Xiao, 2010; Al-Helal and others, 2012; Gomez-Rivas and others, 2014; Blasco and others, 2017; Hirani and others, 2018; Benjakul and others, 2020).

The metastable naturally-ordered ($s = 0.7$) phase Helgeson and others (1978) interpreted to be *probably typical of modern sedimentary dolomite* is confusing. Most work on what is now considered to be 'modern' (Holocene) dolomite was conducted after Helgeson and others (1978) and pre-Holocene dolomites typically have an $s > 0.7$ (see below). The range of K$_{sp°-dol}$ values referenced by Helgeson and others (1978) encompasses both experimental studies and groundwater studies; the groundwater studies are primarily comprised of samples from the Floridan aquifer which is not modern, being Eocene to Miocene in age (Hsu, 1963; Barnes and Back, 1964). We discuss the relationships between, and the complexity of, dolomite ordering and compositions arguing that the later is the most significant property in determining the solubility of (pre-Holocene) dolomites.

Holocene dolomites are found with an $s \ll 1$, though in many cases the $s > 0.7$. For a near surface sediment core Gregg and others (1992) determined through Rietveld analysis that the youngest, nearest surface, calcian (60-54% $CaCO_3$) dolomites had an s of 0.7 and s increased with depth to a maximum of 0.9 (30cm beneath the surface). Rietveld structural analysis iteratively refines a mineralogy to fit XRD data whilst, the simpler more commonly

applied technique of Goldsmith and Graf (1958) determines s using the ratio of the intensities of the $(10\bar{5})$ and (110) reflections. The new method of Fang and Xu (2019) accounts for variations in stoichiometry and suggests that the Goldsmith and Graf (1958) based s estimations for calcian dolomite underestimates s. Fang and Xu (2019) determines that Holocene dolomites from Canada have an $s < 0.5$ whilst those from the Coorong Lake area, South Australia, have an $s \geq 0.5$ (with a maximum $s \sim 0.8$).

Stoichiometric pre-Holocene dolomites are typically completely ordered (i.e. $s \sim 1$) and have, though not always (*see* Miser and others, 1987), homogenous microstructures observed by transmission electron microscopy (TEM) (Reeder and Wenk, 1983; Reeder, 1992; Reeder, 2000). This is unsurprising as the thermodynamic drive for an ordered phase at diagenetic temperatures (0-300°C) is high (Helgeson and others, 1978; Navrotsky and others, 1999). Where cation disorder is interpreted it is often associated with calcian dolomite compositions, though Fang and Xu (2019) conclude that, regardless of stoichiometry, a dolomite with an $s > 0.5$ will have a $(10\bar{5})$ diffraction peak in XRD analysis. This is supported by experimental evidence of a close correlation between the cation disorder and calcian dolomite compositions (Kaczmarek and Thornton, 2017; Kell-Duivestein and others, 2019).

For pre-Holocene dolomites, from a wide variety of compositions, Pina and others (2020) observe all samples to have a $(10\bar{5})$ diffraction peak suggesting at a minimum all pre-Holocene dolomites have an $s > 0.5$, though they also note a range of disorder in stoichiometric dolomite. For Cretaceous calcian dolomites ($\sim$54.5-53.5% $CaCO_3$) Manche and Kaczmerak (2019) determine, using the Goldsmith and Graf (1958) technique, a high degree of disorder (mean of facies $0.43 < s < 0.56$; total range $0.32 < s < 0.84$). We argue that the calculated disorder for these calcian dolomites would likely increase if reanalysed using the Fang and Xu (2019) methodology and that significant cation disorder, defined as $s < 0.5$, resolves on short (Holocene) timescales regardless of stoichiometry.

Hyeong and Capuano (2001), Vespasiano and others (2014), and Blasco and others (2018) interpolate between the Helgeson and others (1978) ordered and disordered dolomite phases to determine the s value (and $K_{sp°-dol}$ value) for the equilibrium dolomite phase (supplementary table 2). All three studies indicate high levels of disorder; Hyeong and Capuano (2001) determine s to be 0.4, whilst reported thermodynamic properties suggest the dolomites in the studies of Vespasiano and others (2014) and Blasco and others (2018) are marginally more ordered. Respectively the dolomites sampled are interpreted to be Oligocene (Hyeong and Capuano, 2001), Mesozoic (Vespasiano and others, 2014), and Triassic-Upper Jurassic (Blasco and others, 2018) in age and these values, particularly that of Hyeong and Capuano (2001), do not appear to be consistent with the aforementioned interpretations of s values for pre-Holocene dolomites being typically > 0.5. Instead, we interpret that these phases, and the Helgeson and others (1978) naturally ordered ($s = 0.7$) phase (or rather the dolomite phase in the Floridian aquifer), reflect equilibration with a natural dolomite phase, of an unknown stoichiometry and order (but probably slightly calcian and slightly disordered).

Stoichiometry.—Many dolomites have microstructural heterogeneity (typically lamellar-like modulations with wavelengths $\sim$100-200Å observed by TEM) and XRD signals that are attenuated and diffuse, and are interpreted to reflect the presence of lattice disorder (Gregg and others, 1992; Navrotsky and others, 1999; Gregg and others, 2015). The degree of this apparent disorder and microstructural heterogeneity is most significant in calcian dolomites with unique signatures respectively for Holocene dolomite, pre-Holocene dolomite and saddle dolomite (Reeder, 1992; Reeder, 2000). Metastable, calcian dolomite is extremely long-lived, being present in samples throughout the Phanerozoic, unlike significant cation disorder that

appears to resolve on short (Holocene) timescales (Lumsden and Chimahusky, 1980, Sperber and others, 1984).

There are two competing theories surrounding the incorporation of Ca into dolomite, but both invoke high-Ca zones. The full range of natural stoichiometric variability in dolomite is limited ($Ca_{1.16}Mg_{0.84}(CO_3)_2$ to $Ca_{0.96}Mg_{1.04}(CO_3)_2$; Land, 1985) and bimodally distributed (fig. 3) with the largest mode centered on ideality and a smaller mode at 54-56% $CaCO_3$ (Lumsden and Chimahusky, 1980; Sperber and others, 1984; Reeder, 2000; Deelman, 2003). To account for the overall mineral stoichiometry, both theories suggest that high-Ca zones are proportionally small with the vast majority of the crystal consisting of stoichiometric well ordered ABABAB... (alternating monolayers of (A) Ca and (B) Mg) dolomite.

1) Ca is systematically incorporated into an ordered, dolomite-like, structure consisting of either variations in the sequence of basal cation layers (otherwise known as stacking disorder, stacking faults or mixed-layer effects) or mixed cation (Ca:Mg 1:1) monolayers (Reeder, 2000; Deelman, 2003 *and references therein*). Both structures destroy $R\bar{3}$ symmetry but computer simulations favor stacking disorder (Wright and others, 2002). For the regular ABABAB... dolomite lattice structure the main proposed stacking disorder is the δ structure ABAAABA... with the Ca:Mg ratio for the unit cell rising from 1:1 to 2:1 (Van Tendeloo and others, 1985; Reeder, 1992).

2) For an Ordovician Ca-rich (45% $MgCO_3$) dolomite Fang and Xu (2018) observe the TEM modulations to be comprised of thick zones of well ordered ($s = 0.9$) stoichiometric dolomite and smaller zones of Ca-rich areas. However, whilst Fang and Xu (2018) do not fully resolve the crystallographic structure of the Ca-rich lamellae, they characterize these zones as Mg-calcite nanoprecipitates as they do not appear to have an ordered structure. Shen and others (2013) proposed Mg-calcite nanoprecipitates in dolomite form through exsolution of separate lamellae of magnesian calcite and stoichiometric ordered dolomite. However, substantial solid state lattice diffusion generating lamellae typically only occurs at high-temperatures as it obeys a temperature-dependent exponential kinetic rate function; for example, pyroxene exsolution during cooling typically occurs at ~800−1000°C (Bragg and Williams, 1934; Grove, 1982). At diagenetic temperatures (<300°C) solid state lattice reordering is by far the slowest mechanism through which dolomite could achieve a more ordered state, with recrystallization (fastest) and surface diffusion (slightly slower) operating several orders of magnitude faster (Usdowski, 1994).

We suggest that the Ca-rich zones, be they the δ structure and/or Mg-calcite, are not generated by solid state exsolution processes and instead are primarily incorporated during the initial crystal growth phase (later recrystallisation typically produces more stoichiometric dolomite). These small zones not only significantly affect XRD and TEM signals, so generating arguably misleading interpretations of the overall s of the dolomite phase based on Goldsmith and Graf (1958), but also appear to cause significant lattice strain modifying the solubility of dolomite (Chai and others, 1995). The transition from stoichiometric dolomite to calcian dolomite is extremely energetic with 56% $CaCO_3$ requiring a ΔH_f° of 15kJ mol^{-1}(Chai and others, 1995). This is similar in magnitude to the aforementioned estimates of the enthalpies of disorder (Helgeson and others, 1978; Navrotsky and others, 1999). The incorporation of 6% $MgCO_3$ into calcite is comparatively favourable requiring a ΔH_f° of 1.2kJ mol^{-1} (eq 3, Navrotsky and Capobianco, 1987).

Dolomite phases.— In the context of an Ostwald-step model the overall reaction of the precipitation of stoichiometric ordered dolomite remains equation (3), but metastable and increasingly insoluble intermediary phases provide a catalytic pathway (Nordeng and Sibley, 1994; Kaczmarek and Sibley, 2007). A wide variety of intermediary metastable phases are

suggested, including magnesite (Chou and others, 1989; Sherman and Barak, 2000), amorphous phases (Kaczmarek and Sibley, 2007; Rodriguez-Blanco and others, 2015), very-high magnesium calcite (Gregg and others, 2015), protodolomite (Graf and Goldsmith, 1956) and calcian/disordered dolomite (Goldsmith, 1983; Reeder, 1992; Kaczmarek and Sibley, 2007; Kaczmarek and Thornton, 2017; Kell-Duivestein and others, 2019). Of these calcian dolomite is by far the most stable, long lasting and commonly encountered so is the most potentially consequential to natural dolomite thermodynamics.

The concept of metastable dolomite phases was first incorporated by Graf and Goldsmith (1956) into their definition of protodolomite; 'single phase rhombohedral carbonates which deviate from the composition of the dolomite that is stable in a given environment, or are imperfectly ordered, or both, but which would transform to dolomite if equilibrium were established'. Protodolomite is commonly used to describe Holocene dolomites which display significant cation disorder (see Fang and Xu, 2019), though Land (1980) and Gregg and others (2015) vociferously reject 'protodolomite' on the basis that any phase without ordering cannot be considered dolomite. Instead, they define rhombohedral Ca–Mg carbonates with near-dolomite stoichiometry, but lacking cation ordering, as very high-magnesium calcite (VHMC). Dolomite in contrast must have evidence of cation ordering; specifically including 'ordering reflections' (Bradley and others, 1953; Graf and Goldsmith, 1956) that cannot occur in the $R\bar{3}c$ space group.

For pre-Holocene dolomites, the vast majority of which have ordering reflections, the present dolomite definition arguably focuses too much on order and too little on composition. Gregg and others (2015) permit the 'near-dolomite stoichiometry' continuum, stemming from Land (1980)'s assertion that 'Ideal, stoichiometric dolomite is the exception, not the rule'. This assertion conflicts with aforementioned frequencies of natural dolomite stoichiometries that indicate the modal dolomite composition is stoichiometric dolomite (fig. 3). Undoubtedly there is complexity in the relationship of cation ordering and stoichiometry but, with reference to the natural stoichiometric modes identified by Sperber and others (1984), for the purposes of this study we consider dolomite as being either stoichiometric (well-ordered) or calcian (with a potentially variable, though indeterminate, level of cation disorder potentially consequential to solubility).

Calcite Stoichiometry

The incorporation of a variable amount of Mg into the calcite structure is typically described as a non-ideal solid solution between the end-members $CaCO_3$ and $MgCO_3$ (see Deelman (2003) for an alternative mixed crystal theory). The dissolution of $MgCO_3$ is described as;

$$MgCO_{3(s)} \leftrightarrow Mg^{2+}_{(aq)} + 2CO_3^{2-}_{(aq)} \qquad (15)$$

with the solubility product constant;

$$(aMg^{2+})(aCO_3^{2-}) = K_{sp°\text{-}mag} \qquad (16)$$

where $pK_{sp°\text{-}mag}$ = -8.035 (table 1). The dissolution of an arbitrary non-stoichiometric calcite ($Ca_xMg_{(1-x)}CO_3$) is described by Thorstenson and Plummer (1977) as;

$$Ca_xMg_{(1-x)}CO_{3(s)} \leftrightarrow (1 \qquad (17)$$
$$- x)Mg^{2+}_{(aq)} + xCa^{2+}_{(aq)}Ca_xMg_{(2-x)}(CO_3)_{2(s)}$$
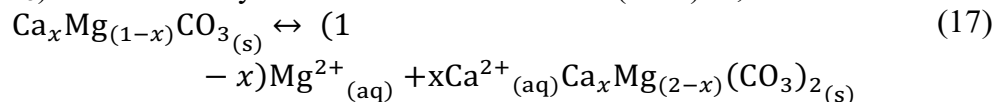
with the solubility product constant;

$$K_{eq(x)} = a^{(1-x)}Ca^{2+}_{(aq)}a^xMg^{2+}_{(aq)}aCO_3^{2-}_{(aq)} \qquad (18)$$

For any value of x, equation (18) can be satisfied by many different combinations of $a\text{Ca}^{2+}$, $a\text{Mg}^{2+}$ and $a\text{CO}_3^{2-}$ such that any saturated solution satisfying equation (18) is said to be at stoichiometric saturation (see Lippmann, 1977; Gresens, 1981a; Gresens, 1981b; Gamsjäger and others, 2000). However metastable or stable thermodynamic equilibrium only occurs at a singular ratio between $a\text{Ca}^{2+}:a\text{Mg}^{2+}:a\text{CO}_3^{2-}$ when every component (end-member) in every phase is at thermodynamic equilibrium such that;

$$a_{\text{Ca}^{2+}\,(aq)} a_{\text{CO}_3^{2-}\,(aq)} = (K_{\text{calcite}})\left(a_{\text{CaCO}_{3(\text{Mg}-\text{calcite})}}\right) \qquad (19)$$

and;

$$a_{\text{Mg}^{2+}\,(aq)} a_{\text{CO}_3^{2-}\,(aq)} = \left(K_{\text{magnesite}}\right)\left(a_{\text{MgCO}_{3(\text{Mg}-\text{calcite})}}\right) \qquad (20)$$

Substituting equations 19 and 20 into equation 18;

$$\log K(x) = (1 - x) \log a_{\text{CaCO}_{3(\text{Mg}-\text{calcite})}} \qquad (21)$$
$$+ x \,\log a_{\text{MgCO}_{3(\text{Mg}-\text{calcite})}} + (1-x)\log K_{\text{CaCO}_3} + x \log K_{\text{MgCO}_3}$$

The solubility of magnesian calcite solid solutions of varying compositions was first evaluated by Thorstenson and Plummer (1977) through a reinterpretation of the calcite solubility data of Plummer and Mackenzie (1974). This reinterpretation by Thorstenson and Plummer (1977) was notably critiqued by Gresens (1981a) for generating far too great a range in equilibrium $\frac{a\text{Ca}^{2+}}{a\text{Mg}^{2+}}$. For reference the solubility of non-ideal solid solutions, such as magnesian calcite, where the activity of each end-member in the solid phase $\neq 1$ (eq 21) and there is a substantial enthalpy of mixing between the end-members is now estimated using Equal-G methods developed by Lippmann (1980) and Königsberger and Gamsjäger (1992). The inclusion of this erroneous data from Thorstenson and Plummer (1977) by Möller and De Lucia (2020) is detrimental to their critique of Bénézeth and others (2018) (see below).

Magnesian calcite is either described as low-Mg calcite (LMC ~ 1-4% - MgCO$_3$ though commonly around 2%), high-Mg calcite (HMC 4-30% MgCO$_3$) or, typically observed only during experimental synthesis, very-high Mg calcite (VHMC ~ 30 to 51 % MgCO$_3$ that includes dolomitic calcite ~ 50% MgCO$_3$), and huntitic calcite (75% MgCO$_3$) compositions (Gregg and others, 2015; Möller and De Lucia, 2020). HMC, in contrast to LMC, is only produced by biogenic processes and is poorly preserved, commonly undergoing multiple episodes of fabric-preserving or -destructive recrystallisation to LMC (Bischoff and others, 1993). HMC typically loses $\geq$50% of the initial Mg content in $10^1 - 10^4$ years depending on conditions (Dickson, 1995 *and references therein*). Thus, the vast majority of subsurface lithologies that contain calcite, are likely to be primarily composed of LMC. For the majority of this study we consider the LMC phase to be pure calcite, though in some cases we consider the effect of LMC on equilibrium $\log_{10}(^a\text{Ca}^{2+}/^a\text{Mg}^{2+})$ values. We assume an ideal solid solution as the difference between calcite and magnesite solubilities is small, LMC compositions are close to the calcite end-member, and the difference between non-ideal and ideal solid solutions decrease as a composition tends towards an end-member (Königsberger and Gamsjäger, 1992). For an ideal solid solution equation (21) reduces to;

$$\log K(x) = (1 - x) \log a_{\text{CaCO}_3} + x \,\log a_{\text{MgCO}_3} \qquad (22)$$

Surface Complexities

The dissolution of any magnesian calcite should be incongruent, such that the more soluble magnesite end-member dissolves until no Mg remains whereupon the calcite end-member starts to dissolve. Due to slow ionic lattice diffusion this process does not occur, and

increases in both Ca^{2+} and Mg^{2+} in solution indicate that the calcite and magnesite end-members dissolve concurrently. The phenomena of non-equilibrium apparent congruent dissolution is described by two competing models (Gresens, 1981a);

1) Congruent dissolution; the solid solution dissolves congruently, behaving as a pure one component phase of a fixed stoichiometry. Stoichiometric saturation is the point at which no further dissolution occurs.

2) Incongruent dissolution; a thermodynamic equilibrium, that can be/is described by a thermodynamic distribution function, is maintained through a surface coating of incongruent dissolution products from the bulk mineral to the solution. The surface coating migrates into the bulk. This model is favoured by Möller and De Lucia (2020) for the dissolution of both magnesian calcite and dolomite.

The experiments of Möller (1973), reinterpreted by Möller and De Lucia (2020), involved monitoring (^{45}Ca) Mg-absorption on a calcite surface in a variable-$MgCl_2$ solution already saturated in calcite, which prevents dissolution of the bulk. In response to the addition of $MgCl_2$, the $\log_{10}(^{a}Ca^{2+}/^{a}Mg^{2+})$ decreases and the Mg content of the surface phase increases linearly across a range of Mg-calcite compositions ($0 < x < 50\%$ $MgCO_3$). However, across a range of low $\log_{10}(^{a}Ca^{2+}/^{a}Mg^{2+})$ values surface compositions were discrete, being either dolomitic calcite (50% $MgCO_3$) or huntitic calcite (75% $MgCO_3$).

At high $\log_{10}(^{a}Ca^{2+}/^{a}Mg^{2+})$ values whilst the surface is clearly able to buffer $\log_{10}(^{a}Ca^{2+}/^{a}Mg^{2+})$ values, but the capacity is essentially limited by the reactive thickness of the surface layer and by the possible compositions of the surface Mg-calcite phases. This is evident at low $\log_{10}(^{a}Ca^{2+}/^{a}Mg^{2+})$ values which correspond to equilibrium discrete surface compositions where surface capacity to buffer solution $\log_{10}(^{a}Ca^{2+}/^{a}Mg^{2+})$ values in response to any addition or removal of Mg^{2+} is non-existent. The $\log_{10}(^{a}Ca^{2+}/^{a}Mg^{2+})$ values that correspond to a ~50% (49.5-50.5%) $CaCO_3$ dolomite surface composition range widely from -0.30 to -0.78.

There are clearly outstanding questions surrounding the interplay between compositions of the bulk mineral, reactive surface layers, and the solution during times of significant mass transfer between phases. At one extreme, if the entire bulk mineral were to completely dissolve in a closed system the $\log_{10}(^{a}Ca^{2+}/^{a}Mg^{2+})$ value will equal the bulk mineral [Ca]/[Mg]. As the mass transfers between phases increase it seems reasonable to conclude that $\log_{10}(^{a}Ca^{2+}/^{a}Mg^{2+})$ values will increasingly reflect equilibrium with the bulk composition and the composition of the thin surface phase responds arbitrarily to the solution $\log_{10}(^{a}Ca^{2+}/^{a}Mg^{2+})$ value, maintaining its role as a catalytic intermediary phase for the overall dissolution reaction (eq 3). The relationships between reaction progress, insoluble surface phases migrating into the bulk and equilibrium solutions have been extensively explored for LMC (Sinclair, 2011; Sinclair and others, 2012).

Möller and De Lucia (2020) suggest that the Möller (1973) $\log_{10}(^{a}Ca^{2+}/^{a}Mg^{2+})$ value for a calcite surface phase with a dolomitic-composition is the same as the $\frac{aCa^{2+}}{aMg^{2+}}$ value in equilibrium with the Bénézeth and others (2018) dolomite phase (fig. 4b). As Möller and De Lucia (2020) plot the Möller (1973) $\log_{10}(^{a}Ca^{2+}/^{a}Mg^{2+})$ values and those from Bénézeth and others (2018) on the same scale as the erroneous Thorstenson and Plummer (1977) data, they do appear to be identical. However the $\log_{10}(^{a}Ca^{2+}/^{a}Mg^{2+})$ values for the Bénézeth and others (2018) dolomite phase at 25°C in 0.1M NaCl and the highest $\log_{10}(^{a}Ca^{2+}/^{a}Mg^{2+})$ value for a dolomitic surface composition (49.5-50.5% $CaCO_3$; Möller (1973)) are -0.01 and -0.30 respectively (fig. 4b). Möller and De Lucia (2020) state the Bénézeth and others (2018) dolomite phase ($pK_{sp°-dol}$) actually reflects equilibrium between calcite (observed during experiment 8 of Bénézeth and others

(2018)) and a disordered dolomite, with the surface phases of both minerals interpreted to be different and also stated to be in equilibrium with the solution. We note the precipitation of calcite is inconsequential to the determination of $pK_{sp°-dol}$ (eq 4) so long as aCa^{2+}, aMg^{2+} and aCO_3^{2-} are accurately observed. Supporting the view that the Bénézeth and others (2018) dolomite phase primarily reflects equilibrium with a bulk dolomite phase, if it is modelled to be at simultaneous equilibrium with calcite the calculated equilibrium $\log_{10}(^aCa^{2+}/^aMg^{2+})$ value rises to 0.20 which agrees well with the range of prior literature estimates of $\log_{10}(^aCa^{2+}/^aMg^{2+})$ values at calcite-dolomite equilibrium (fig. 5b). When contextualized against the relatively narrow range of $\log_{10}(^aCa^{2+}/^aMg^{2+})$ values recorded by prior studies the magnitude of the difference in $\log_{10}(^aCa^{2+}/^aMg^{2+})$, be it 0.29 (dolomite-only) or 0.50 (calcite-dolomite), between the Bénézeth and others (2018) dolomite phase and the Möller (1973) dolomitic calcite surface phase is clearly significant and not the same (as Möller and De Lucia (2020) conclude).

The equilibration of the solution with the Mg-calcite surface phase may be of significance to the accuracy of the $pK_{sp°-dol}$ estimate where the degree of mass transfer between the bulk and solution is low, which may be the case during experimental synthesis. Using XPS data Bénézeth and others (2018) confirmed that the surface dolomite precipitates phases had near (though not ideal) dolomite stoichiometry. In contrast to XRD data, XPS does not give information on ordering and thus whether the surface phase is dolomite, and not VHMC, is equivocal.

Möller and De Lucia (2020) argue that surface phases of calcite or dolomite typically have a greater $MgCO_3$ mol% than the bulk mineralogy since Mg^{2+} replaces surface Ca^{2+} as it is more strongly bound. As a result, the presence of Mg^{2+} in solution increases Ca^{2+} concentrations (Möller, 1973; Möller and De Lucia, 2020). With respect to the experiments of Plummer and Mackenzie (1974), as the biogenic calcite with a bulk $HMC_{(18.4\%MgCO_3)}$ transitions to $HMC_{(11.7\%MgCO_3)}$ (fig. 4a) the solution is interpreted by Möller and De Lucia (2020) to be at equilibrium with a $HMC_{(30\%MgCO_3)}$ surface phase. There appear to be two problems with the interpretation, which Möller and De Lucia (2020) state has wide implications, where the end stage solution with a $\log_{10}(^aCa^{2+}/^aMg^{2+}) = 0.95$ primarily reflects an equilibrium with a $HMC_{(30\%MgCO_3)}$ surface phase and cannot be used to identify the bulk carbonate composition;

1-Non-uniqueness of solutions.— The non-uniqueness of $\log_{10}(^aCa^{2+}/^aMg^{2+})$ caused by incongruent dissolution of HMC can be exemplified by interpreting solution $\log_{10}(^aCa^{2+}/^aMg^{2+})$ through a steady state mass balance of co-eval magnesian calcite phases. The interpretation by Plummer and Mackenzie (1974) that the initial phase of the bulk calcite ($HMC_{(18.4\%MgCO_3)}$) undergoing dissolution has a composition of $HMC_{(23.8\%MgCO_3)}$ and the end stage phase is $HMC_{(11.7\%MgCO_3)}$ was derived by modelling the rates of change of Ca^{2+} and Mg^{2+} in solution during dissolution. We recognise that without temporal data the $\log_{10}(^aCa^{2+}/^aMg^{2+})$ value of 0.95 could not be used to identify either the $HMC_{(23.8\%MgCO_3)}$ *or* $HMC_{(11.7\%MgCO_3)}$ compositions as this is a non-unique solution. Spot EMPA determined compositions of similar unreacted carbonate grains and XRD of both the unreacted, and to a lesser extent, reacted samples correspond well to the calculated $HMC_{(23.8\%MgCO_3)}$ and $HMC_{(11.7\%MgCO_3)}$ phases (Plummer and Mackenzie, 1974). This supports the interpretation of Plummer and Mackenzie (1974) that $\log_{10}(^aCa^{2+}/^aMg^{2+})$ is directly correlated to the composition of the bulk phase.

Assuming a steady state reaction between $HMC_{(23.8\%MgCO_3)}$ and $HMC_{(11.7\%MgCO_3)}$ a mass balanced solution can fix $\frac{[Ca^{2+}]}{[Mg^{2+}]}$ (and $\log_{10}(^aCa^{2+}/^aMg^{2+})$ at least in early reaction stages where activities approximate concentrations) to 0.95;

$$aCa_{0.762}Mg_{0.238}CO_3 \leftrightarrow bCa_{0.883}Mg_{0.117}CO_3 + cCa^{2+} + dMg^{2+} + eCO_3{}^{2-}; \frac{c}{d} \quad (23)$$
$$= 0.95$$
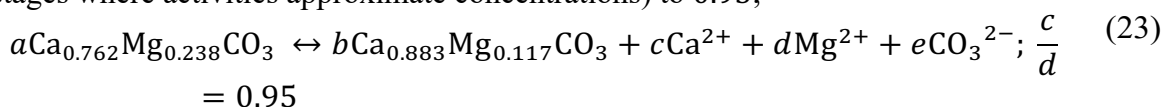
which results in the solution;
$$3.27Ca_{0.762}Mg_{0.238}CO_3 \qquad\qquad\qquad\qquad\qquad (24)$$
$$\leftrightarrow 2.27Ca_{0.883}Mg_{0.117}CO_3 + 0.49Ca^{2+} + 0.51Mg^{2+} + CO_3{}^{2-}$$
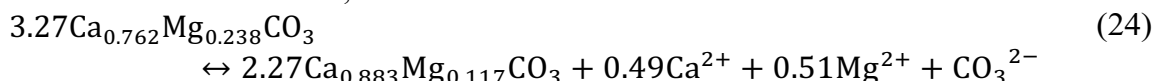
2- Observations of Mg-fractionation into the solution phase.— Multiple measurements of the Mg partition coefficient (Kd_{Mg}) for magnesian calcite during both dissolution or precipitation find that Mg heavily fractionates into the solution over the crystal phase (Kd_{Mg} ~ 0.014-0.06; Huang and Fairchild, 2001 *and references therein*). Such extreme fractionation is consistent with the incongruent precipitation of nearly pure calcite (i.e.~ $CaCO_3$) that occurs early in the Plummer and Mackenzie (1974) experiment. The final incongruent steady state $HMC_{(11.7\%MgCO_3)}$ precipitate that accounts for the bulk of the mass transfer results from the increasing aMg^{2+} in the closed system derived from the $HMC_{(23.8\%MgCO_3)}$ phase. The presence of a thin $HMC_{(30\%MgCO_3)}$ intermediary phase seems at odds with observations of overall Mg fractionation into solution during incongruent precipitation/dissolution, but can be reconciled through mineral surface processes and crystallization kinematics.

The surface buffering capacity for $\log_{10}(^aCa^{2+}/^aMg^{2+})$ will not only reflect changes in the surface monolayer composition but also any changes in the electrical double layer. The surface potential derives from 'potential determining ions' (PDIs). PDIs are absorbed dehydrated ions with adjacent vacancies caused by preferential dissolution of surrounding ions, adsorbed hydrated surface complexes, and adsorbed charged ions (Prédali and Cases, 1973; Derkani and others, 2019). The surface potential is notably sensitive to;

1) Changes in background ionic strength. The accumulation of 'indifferent' ions such as Na^+ and Cl^- in the electric double layer leads to effective electrostatic screening, such that the zeta potential tends towards zero with increasing ionic strength (Strand and others, 2006; Derkani and others, 2019). As such at high ionic strength surface absorption/adsorption is increasingly irrelevant in buffering $\log_{10}(^aCa^{2+}/^aMg^{2+})$. As the Möller (1973) experiment only evaluates equilibrium using distilled water, arguably the purported $\left(\frac{Ca}{Mg}\right)_{surface} - \left(\frac{Ca}{Mg}\right)_{solution}$ relationship maybe extremely sensitive to any changes in ionic strength.

2) The bulk crystal composition. Ca^{2+} and Mg^{2+} are interpreted as PDIs for calcite whilst they are probably not PDIs for dolomite (see Derkani and others (2019) *and references therein*). This suggests that the dolomite surface has no potential to buffer $\log_{10}(^aCa^{2+}/^aMg^{2+})$ through adsorption/absorption and that only recrystallisation (or ion-exchange with the monolayer) can modify $\log_{10}(^aCa^{2+}/^aMg^{2+})$ values.

For dolomite, aCa^{2+} controls dissolution rates. During early stages of dissolution there is an initial spike in $\log_{10}(^aCa^{2+}/^aMg^{2+})$ and thus, the rate limiting step is interpreted to be the dissolution of Mg-surface complexes (Pokrovsky and Schott, 2001; Gautelier and others, 2007). Although the kinetics of calcite dissolution in general are poorly constrained (Pokrovsky and others, 2009), this is likely to also be the case for magnesian calcite. The reason for the lower solubility of the Mg-surface complexes is interpreted to be the larger enthalpy of hydration for Mg^{2+} relative to Ca^{2+} (Busenberg and Plummer, 1982; Pokrovsky

and Schott, 2001; Gautelier and others, 2007). Thus, in agreement with Möller and De Lucia (2020), there is merit in suggesting that the surface compositions of both calcite and dolomite are likely to be Mg-rich. However, for dolomite after the initial release of Ca^{2+}, steady state quickly establishes, the overall dissolution and equilibrium $\log_{10}(^aCa^{2+}/^aMg^{2+})$ values appear to reflect congruent dissolution of stoichiometric dolomite, and the surface [Ca]/[Mg] overall remains constant (Pokrovsky and Schott, 2001). This assertion of a constant surface [Ca]/[Mg] is critiqued by Möller and De Lucia (2020) who argue that the Pokrovsky and Schott (2001) XPS measurements sample 20-25 layers whilst the Möller (1973) Ca^{45} measurements record compositional variation of only a single monolayer (albeit of magnesian calcite) (Möller and Sastri, 1974; Möller and De Lucia, 2020). Mixed cation layers, which could easily buffer $\log_{10}(^aCa^{2+}/^aMg^{2+})$ through ion exchange, are not observed in dolomite (see above) so the ability of the dolomite surface monolayer to buffer $\log_{10}(^aCa^{2+}/^aMg^{2+})$ values is likely to be smaller than that envisaged for calcite surfaces.

We disagree with Möller and De Lucia (2020) and support the view of Pokrovsky and Schott (2001) that dolomite dissolution is likely to be congruent and surface dolomite compositions comparable to the bulk phase. We acknowledge the potential for modification of $\log_{10}(^aCa^{2+}/^aMg^{2+})$ values through equilibrium with variable composition calcite surface phases and the subsequent detrimental effect on the determination of $K_{sp°-dol}$ through the use of an erroneous $K_{sp°-cal}$ value. However, we suggest that the potential for significant mass transfer in groundwaters should lead to $\log_{10}(^aCa^{2+}/^aMg^{2+})$ values that reflect equilibrium with bulk phases. Equilibrium with a wide variety of differently composed surface phases should lead to a wide, scattered range of $\log_{10}(^aCa^{2+}/^aMg^{2+})$-temperatures as interpreted by Möller and De Lucia (2020) for their meta-analysis (n=242) of groundwaters. We suggest that the potential for significant mass transfer in groundwaters should lead to equilibrium with bulk phases and a narrower range of $\log_{10}(^aCa^{2+}/^aMg^{2+})$ values for a given temperature.

Determination of $K_{sp°\text{-}dol}$

There are two contrasting approaches to calculating $K_{sp°-dol}$;

1) Indirectly determining $K_{sp°-dol}$ by combining free energies of ions and compounds, including dolomite (see 'Thermal decomposition\Database' in supplementary table 2). Enthalpies of non-aqueous reactions (decomposition/oxidation) involving dolomite are made at high temperatures and pressures (e.g., 700 °C and 1-2 kb CO_2 Chai and Navrotsky, 1993). These values are extrapolated to standard state conditions and combined with ionisation/hydration enthalpies for Ca^{2+} and Mg^{2+} to determine $K_{sp°-dol}$. Similarly, new or existing thermodynamic data (potentially including thermal decomposition data) of minerals, including dolomite, can be combined and regressed to produce new databases of updated thermodynamic properties of minerals (Holland and Powell, 1990; Holland and Powell, 1998). New aqueous models, such as Miron and others (2017), can also lead to updated estimates of $K_{sp°-dol}$.

2) Directly, experimentally determining $K_{sp°-dol}$ in aqueous solutions is thought to be more accurate and applicable to natural conditions than indirect approaches (Hefter and Tomkins, 2003). Observations of aqueous mineral solubility are ideally made over a wide temperature range using controlled experiments (see 'Solubility (experimental)' in supplementary table 2), though sluggish kinetics may inhibit the attainment of equilibrium at lower temperatures in reasonable time frames (<100°C, Gregg and others, 2015). Dolomite equilibrium has been measured at 80°C by Gautelier and others (2007) and at 53°C by Bénézeth and others (2018). However, Gautelier and others (2007) only approach equilibrium through dissolution, and there remains uncertainty (Möller and De Lucia, 2020) around the

composition of the precipitating phase in Bénézeth and others (2018). An alternative approach based on groundwater composition, and on the assumption that the residence time of subsurface fluids is sufficient for the attainment of calcite-dolomite equilibrium, has the potential to determine $K_{sp°-dol}$ over a wide temperature range (see 'Solubility (groundwater)' in supplementary table 2). We further review the experimental and the groundwater methods for deriving $K_{sp°-dol}$ below.

Solubility.— The $K_{sp°-dol}$ can be determined from conditions of undersaturation *via* dissolution or from supersaturation *via* precipitation, with equilibrium ideally approached from both directions so demonstrating thermodynamic reversibility (Hefter and Tomkins, 2003). A secondary effect of determining the temperature dependence of the solubility product with a Maier-Kelley regression is that the difference between the two approaches is averaged. This is known as the quasi-static method, and the smaller the difference between the two approaches the more precise the measurement (Hefter and Tomkins, 2003). Most experimental estimates of $pK_{sp°-dol}$, are based only on approaching equilibrium from conditions of undersaturation because of the difficulty in precipitating *unequivocally* ordered stoichiometric dolomite on realistic experimental timescales, particularly at lower temperatures.

Bénézeth and others (2018) suggest that, aside from Gautelier and others (2007) at 80°C, no values for $K_{sp°-dol}$ have been reported for temperatures greater than 25°C. This leads to the belief that a reliable determination of $K_{sp°-dol}$ by classical, single-phase solubility experiments is impossible at higher temperatures due to the retrograde solubility of dolomite. Whilst technically correct, this ignores the work of Rosenberg and Holland (1964), Baker and Kastner (1981), Morrow and others (1994), and Usdowski (1994) (see 'Solubility (experimental)' in supplementary table 2) who determined $K_{sp°-dol}$ through evaluating the calcite-dolomite boundary (60-420°C) in $CaCl_2$-$MgCl_2$ solutions. These studies unequivocally (based on XRD evidence) precipitated dolomite from a calcite seed. Rather than hindering determination of $K_{sp°-dol}$, higher temperatures reduce the kinetic impediments for dolomite precipitation (Usdowski, 1994; Debure and others, 2021).

Groundwater.—The groundwater approach represents not only an opportunity to evaluate $K_{sp°-dol}$ at near-equilibrium conditions due to long residence times, but can be seen complementary to experimental approaches as it offers an opportunity to understand natural variations in calcite-dolomite equilibrium. However, whilst in an experiment both the solute and solvent can be analysed, for the groundwater approach these parameters are less well-constrained.

Defining $K_{sp°-dol}$ assuming the system is only-dolomite buffered (eq 4) is complicated by sample degassing and/or equilibration with atmospheric CO_2 which result in pH and HCO_3^- measurements being of poor quality (Hyeong and Capuano, 2001). Thus, the calculated activity of CO_3^{2-} can be in error, which typically results in higher estimates of $K_{sp°-dol}$ (supplementary table 1). The advantage of assuming the solution is at calcite-dolomite equilibrium is the independence from pCO_2 and pH measurements that results from using $K_{sp°-cal}$ (eq 8) (Hyeong and Capuano, 2001). Moreover, by multiplying the activities for the dolomite-only buffered equation (4) system the errors on each term are cumulated, whereas if calcite-dolomite equilibrium (eq 8) is assumed the errors on each term are reduced and compensatory (Hsu, 1963).

Prior studies applying the groundwater approach (Hsu, 1963; Barnes and Back, 1964; Hyeong and Capuano, 2001; Vespasiano and others, 2014; Blasco and others, 2018; see 'Solubility (groundwater)' supplementary table 2) are site specific and establish *a priori* the presence of both calcite and dolomite in host aquifers. In particular, Hyeong and Capuano (2001) established a $\log_{10}(^aCa^{2+}/^aMg^{2+})$ - temperature relationship for samples taken at

multiple depths in different sites consistent with prior estimations of calcite-dolomite equilibrium. However, as is similarly observed for the Möller and De Lucia (2020) meta-analysis of global brines (n=242) there remained considerable apparent scatter in $\log_{10}(^aCa^{2+}/^aMg^{2+})$ values.

The objective of this study is to undertake a meta-analysis of a much more substantial groundwater database (n=11,480) focussing in particular on the scatter of $\log_{10}(^aCa^{2+}/^aMg^{2+})$ – temperature values. Through in-depth evaluations of $\log_{10}(^aCa^{2+}/^aMg^{2+})$ - temperature relationships at a range of spatial scales we establish that calcite-dolomite equilibrium is extremely common in subsurface fluids. $K_{sp°-dol}$ is then accurately evaluated using a mixed modelling statistical approach. Variations in $\log_{10}(^aCa^{2+}/^aMg^{2+})$ - temperature relationships are interpreted to relate to the composition of the equilibrium dolomite phase, with equilibria with other minerals in particular discounted.

METHODOLOGY

To evaluate the dolomitizing potential of subsurface fluids, geochemical data is sourced from the U.S. Geological Survey National Produced Waters Geochemical Database (PWGD V2; Blondes and others, 2016). This is an extensive geochemical inventory of formation waters from a range of sedimentary lithologies across North America to a maximum 6.6 km depth. The PWGD has previously been used for a variety of purposes including to investigate the potability of produced water (Aines and others, 2011), hydrogeological history of formational fluids (Engle and Blondes, 2014) and for mineral exploration (Ray, 2016).

The PWGD dataset of 165,960 waters is filtered using a set of criteria (supplementary table 3) adapted from Hitchon and Brulotte (1994) and Blondes and others (2016), leading to the rejection of 93% of samples. The remaining 11,846 samples are categorized into 5 lithological groups; Sandstone, Dolomite, Limestone, Mixed Carbonate and Shale (supplementary table 4).

The PWGD includes the temperature at which the pH was recorded, albeit very rarely (3% of samples with an average of 24°C) and we set this temperature to 25°C if not provided. Of more critical importance the PWGD lacks data on temperatures at-formation-depth. We use the Southern Methodist University Heat Flow (SMUH) database to estimate temperature at-formation-depth. This database contains both geothermal observations and calculated thermal gradients for 99,044 records (fig. 6b) of drilled wells across North America (Blackwell and others, 2011). The database is filtered to include only records that have bottom hole temperature-Harrison correction (BHT-Harrison) geothermal gradients between 0°C/km and 200°C/km (Harrison and others, 1983). Geothermal gradients are down-sampled to 0.1°x0.1° Lat/Long areas then interpolated (SciPy griddata linear method) to provide local geothermal gradients across the US (fig. 6a).

At-formation-depth temperatures are calculated from sample depth measurements (PWGD) using the corrected geothermal gradients (SMUH) and the mean annual surface temperature (see Shope and others (2012) for a similar method). Surface temperatures are derived from mean annual land surface temperature (MAST) for North America between 2003-2014 (Bechtel, 2015) and processed to a 0.1°x0.1° Lat/Long resolution (fig. 6e). The combined surface temperatures (MAST) and corrected geothermal gradients (SMUH) are referred to as the geothermal model. Of the filtered PWGD samples, 11,480 samples (96.9%) are successfully matched to both the SMUH and MAST datasets; the geochemical composition and lithological classification of samples in this dataset that are used in subsequent PHREEQC modelling are summarized in supplementary tables 4 and 5. The majority of unmatched samples represent locations outside the contiguous continental states.

Using PHEEEQC with the Pitzer database (Plummer and others, 1988; Parkhurst and Appelo, 1999), which is valid up to 200°C and halite saturation, fluids are driven from the temperature at which the pH was measured (or 25°C) to their estimated at-formation-depth

temperature. The Pitzer database is appropriate here as the median (P50) total dissolved solids is 42,745 mg/l and the median (P50) Pitzer calculated ionic strength is 0.85 mol/kg (supplementary table 5). The data (n=11,480) is then filtered such that the subset of samples with $\log_{10}(^aCa^{2+}/^aMg^{2+})$ -temperature values outside of the range between SUPCRT92 (slop07.dat) calcite - ordered dolomite & calcite - disordered dolomite equilibriums (termed hereafter the 'SUPCRT92-filter') are excluded as they are determined unlikely to be at calcite-dolomite equilibrium. The remaining samples (n=10,343) constitute the main dataset for the principal regression analysis (supplementary table 4).

Both generalized linear mixed-effects models that use fixed and random effects (lme4; Bates and others, 2014), and linear models that contain only fixed effects, were constructed using R (Team, 2000) to evaluate the relationship between fluid temperature (fixed effect) and $\log_{10}(^aCa^{2+}/^aMg^{2+})$ (outcome variable) (table 2). The relationship is evaluated using variations of the Maier-Kelley thermodynamic regression formula;

$$\log K = a + bT + \frac{c}{T} + d \log T + \frac{e}{T^2} \qquad (25)$$

Models utilizing the full five term Maier-Kelley thermodynamic regression formula are found to produce spurious changes, particularly at temperatures <25°C, and are not presented. For most analyses in this study a three term (a, b and c) expansion, as used by Bénézeth and others (2018), is supported by goodness of fit tests, in particular the Akaike information criterion (AIC) (see below). Typically, a three-term model generates very similar results to a two-term (a and b) model but provides the additional benefit of being able to estimate the heat capacity coefficient (C_p°). This is the primary equation used for most models presented below.

The application of a mixed-effect model evaluates the variation in the fixed effects for each 'group' of samples which share an identical descriptive attribute such as a commonality in the field or the type of lithology. These group-level descriptive attributes are modelled as random effects. This study evaluates the effect of up to 7 different group-level effects present for the majority (missing data is inconsequential) of all samples; the depth, the formation, the field, the basin, the lithology and the age (broken down into period and series) of a sample.

As an example, the representative mixed model (J21) that utilizes all 7 random effects is coded into R as follows;

$$\text{lmer}\left(\frac{a Ca^{2+}}{a Mg^{2+}} \sim 1 + T + I(T^{-1}) + (1|\text{DepthID}) + (1|\text{Field}) + (1|\text{Formation}) \right. \qquad (26)$$
$$+ (1|\text{Basin}) + (1|\text{Lithology}) + (1|\text{Period})$$
$$\left. + (1|\text{Series}), \text{data} = \text{dataset}\right)$$

For a single sample in the PWGD there is a 3-level hierarchical structure for geographical data. This is implemented in the mixed model as a series of nested random effects though this nesting is not explicitly coded into R (as it is implemented at a database level). Samples from different wells are collated into groups sourced from a common field (n=2,168; unless otherwise stated, all group sizes reported, are for the post-SUPCRT filter dataset i.e. n=10,343) and fields are nested together by shared basin (n=53). Similarly, the series age attribute (n=35) is nested within a geological period (n=13).

Samples within a field are collated into groups with similar depths on the assumption of a commonality in formation/fluid. This assumption works best where, at a field scale, the subsurface geology is laterally homogenous and hydrologically connected. There are 9,049 unique depth groups (i.e. all samples taken from exactly the same reported depth in an individual well), which suggests that there are 1294 (10,343-9,049) repeat measurements. By

collating samples taken from similar depths the number of groups is significantly reduced. For example, for a 300m depth interval grouping, where all samples for a particular field between 600-900m are grouped together, the number of groups reduces to 3,296.

For the representative model (model J21) the simplified (i.e presenting all random effects as crossed random effects) formal statistical notation of this 3-term Maier-Kelly regression, 7 random effect model is as follows;

$$\frac{a\text{Ca}^{2+}}{a\text{Mg}^{2+}}_{ijklmnpq} = \beta_0 + \beta_1.T_{ijklmnpq} + \beta_2.T^{-1}_{ijklmnpq} + U_j + U_k + U_l + U_m + U_n \qquad (27)$$

$$+ U_p + U_q + \epsilon_{ijklmnpq}$$

Where $\frac{a\text{Ca}^{2+}}{a\text{Mg}^{2+}}_{ijklmnpq}$ represents the ith value of the response variable $\log_{10}(^a\text{Ca}^{2+}/$ $^a\text{Mg}^{2+})$, β_0 is the global intercept, β_1 and β_2 are the coefficients for the temperature (K) which is modelled as a fixed effect and $U_{(j...p)}$ are the 7 random intercepts with the subscripts denoting depth(j), field(k), basin(l), formation(m), lithology(n), period(p) and series(q). $\epsilon_{ijklmnpq}$ is the residual or error term for the ith value after accounting for the random effect terms.

The mixed model returns three sets of results that are of interest. At the global-level, the model generates a global intercept (β_0) and global fixed effect coefficients (β_1 and β_2) which effectively describe the properties of the average sample. At a group-level the mixed model returns information that describes how much of the model variance can be attributed to each group-level random effect (e.g. 'field' or 'formation') that is implemented. As each random effect is implemented the residual variance ($\epsilon_{ijklmnpq}$) typically reduces. For each group, for example all samples from the Soso Field, Mississippi, the model returns coefficients that describe the deviation of the group from the global-level model. Mixed models that only evaluate the deviation of group data away from the global-level model by generating a new (β_0) intercept are random intercept (RI) models. By inserting RI values for different groups into the place of the global intercept, with the global fixed effects remaining the same, separate models for different groups can be generated by an end user. Models can incorporate the dependence of the fixed effect terms (β_1 and, though not used in this study, β_2) on the random effects such that each group has both a unique RI value and gradient for the change in $\log_{10}(^a\text{Ca}^{2+}/^a\text{Mg}^{2+})$ with temperature; these are termed random slope models.

A primary feature of mixed modelling is partial pooling. Partial pooling stands in contrast to the alternative strategies of complete and no pooling. Complete pooling disregards the influence of groups and models all data as a single group (e.g. a linear model (model K1) of the entire PWGD dataset). However, the variations between groups are suppressed and information for individual groups, which may be of significant interest, is lost. Moreover, the suppression of group information can have deleterious effects on uncertainty estimates. A no-pooling approach models each group separately (e.g. a linear model for each group in the PWGD) and overstates the variation between different groups making individual groups appear to be more different than they actually are. The partial pooling approach represents a compromise; all three sets (levels) of model results are informed by both the group size and data contained within each group. Groups with small numbers of sample carry less information so both influence the group-level and global level results less, whilst coefficients for small sample size groups are closer to group-level/global-level results (see Gelman and Hill, 2006).

The application and statistical validity of mixed models for datasets with limited numbers of observations and groups is an active area of research as applied research is frequently data limited (Bell and others, 2010, Hox and others, 2017). If the focus of the model is on the global level fixed effect coefficients, mixed models are not overly sensitive to

the numbers of samples and groups present in the model (Bell and others, 2010). There are however several general guidelines for the minimum numbers of groups and samples, particularly when there is interest in the random component. Hox and others (2017) suggest that the ratio of the number of groups to the number of individuals in each group be on the order of 100/10, 50/20 or 30/30. The mixed models (A1-I1) presented in the ground-truthing section below all fail these rules of thumb and the linear models in these cases are thought to be more statistically valid. However, the small sample size mixed models correlate well with the linear model results, and they are included mainly because they demonstrate important widely recognised features of mixed model on a more relatable small scale. The models for the PWGD (n=10,343 or 11,480) easily surpass minimum group and sample requirements. Groups with small numbers of samples (n<5) are not thought to significantly affect fixed and random effects (Hox and others, 2017). This is a particular issue for the PWGD analysis where many groups, particularly depth-specific groups, may have only 1 sample.

Model selection aims for the simplest model to describe the relationship between temperature and $\log_{10}(^aCa^{2+}/^aMg^{2+})$, and whilst guided by statistical tests remains inherently subjective. The Akaike information criterion (AIC), the R^2, 95% confidence intervals, and the intraclass correlation coefficient (ICC) are statistical tests that are used to assist selection by evaluating goodness of fit and model uncertainty. In particular, the AIC compares differently parameterized models that use identical datasets. The model with the lowest AIC value (AIC_{min}) is regarded as the best, but differences between models with AIC values smaller than 10 are not regarded as sufficient criteria for model rejection and differences smaller than 2 suggest support for both models (Burnham and Anderson, 2002).

We frequently observe that samples from an individual field appear to have strong 'within-group(field)' similarities but there are differences 'between-groups(fields)'. This is the case even for fields that are immediately adjacent. The intraclass correlation coefficient (ICC) describes how strongly within-group observations resemble each other or, more specifically, the fraction of total variation of a dataset that can be accounted for by variation between-groups (Gelman and Hill, 2006). The ICC is implemented using the method of Nakagawa and others (2017) and (as is typical) we report only the adjusted ICC value, which is the percentage of total variance explained by groups (excluding fixed effect variance) and in essence the reproducibility of replicate measures from each group. ICC values < 0.4 indicate poor reproducibility, values $0.4 \leq ICC < 0.75$ indicate fair to good reproducibility and values of ICC ≥ 0.75 indicate excellent reproducibility. For an ICC of zero, observations within-groups are no more similar than observations between-groups. If the ICC~0 there is no difference between a mixed model and a linear model and as such the ICC is used as a discriminator for determining whether to apply a mixed model technique. Whilst the fixed effects may change little if moving from a linear to a mixed model, as is the case in many instances in this study, the larger the ICC, the larger the impact on the standard error of a regression term and other measures of model uncertainty such as 95% confidence intervals. It is well recognised that mixed modelling demonstrates significant improvements in accurately quantifying uncertainty for clustered datasets over linear models (Gelman and Hill, 2006).

For linear models only, the adjusted R^2 value is reported. For mixed models the method of Nakagawa and others (2017) is used to determine the marginal and conditional R^2. The marginal R^2 describes the variance explained by the model that is a product of only the fixed effects. This is generally very similar/identical to the R^2 of a comparative linear model. The conditional R^2 of a mixed model describes the variance explained by both fixed and random effects and is typically higher than the marginal R^2 as random effects can account for more of the variance.

RESULTS

The PWGD samples (n=11,480) come from a wide range of locations and depths across 30 of the contiguous US continental states, though historically prolific oil producing states such as Wyoming (n=2,946) and Texas (n=2,495) are heavily represented (fig. 6d). The range in annual surface temperatures is relatively small (-5-21°C) compared to the range of geothermal gradients (11-88°C/km) (supplementary table 5; fig. 6a and e). With a median formation depth of 1.9km, the contribution to the uncertainty in the estimated at-formation-depth temperature from the geothermal gradient ($\sigma = 6$°C / km) is typically at least twice that from the surface temperature ($\sigma = 6$°C).

The relationship between $\log_{10}(^aCa^{2+}/^aMg^{2+})$ and temperature is initially evaluated for two areas where prior studies have demonstrated that pore waters are at calcite-dolomite equilibrium, allowing ground truthing of the approach. The areas are the north-eastern section of the Texas Gulf Coast (TGC) basin, studied by Hyeong and Capuano (2001) and to a lesser extent by Morton and Land (1987), and the Mississippi Salt Dome (MSD) basin studied by Kharaka and others (1987). To evaluate the reliability of this study's geochemical and geothermal methodology within these areas we compare both groundwater chemistry data in the PWGD and the at-formation-depth temperatures derived by this study's geothermal model with the geochemical and temperature observations in the published studies.

Ground Truthing: Thermal Gradients in the Texas Gulf Coast

Datasets from the test area within the north-eastern TGC include samples from two formations; the Oligocene Frio Fm. and the Miocene Fm.. The Frio Fm. is comprised of sand-rich fluvio-deltaic sediments that have a variable mineral composition (Loucks and others, 1984), including both detrital carbonate grains (caliche clasts) and diagenetic carbonate cements (Loucks and others, 1980). The Miocene Fm., otherwise known as the Miocene Major Stratigraphic Unit, is comprised of similar fluvio-deltaic sandstones. Both formations are locally cemented by carbonate which comprise ≤15% of the total rock volume (Land, 1984; Hyeong and Capuano, 2001). Carbonate cements are primarily calcite, ankerite and dolomite; dolomite constitutes 10 - 15% of the cement and therefore ≤0.8% of the total rock volume (Land, 1984; Hyeong and Capuano, 2001). However, mineralogical variations, both regionally and with depth, are poorly understood.

Within the Frio Fm. Morton and Land (1987) define four regions of typically distinct end-member water compositions, thought to reflect local geochemical processes, influx of waters from deeper aquifers, and structural discontinuities (faults and diapirs) that restrict regional fluid flow. Our Test Area A (bounding box W94°48'-W96°00'/N28°48'-N29°30' totalling some 9059km²) lies within the most northerly of Morton and Land's (1987) sub-regions and is referred to here as the 'north-eastern TGC' (fig. 7a and b). It includes samples with a wide range of temperatures (43-150°C) and depths (651- 4,740m), from the three fields in the seminal high-resolution study of Hyeong and Capuano (2001); the West Columbia, Chocolate Bayou and Halls Bayou fields (the latter collated into the 'Chocolate/Halls Bayou field' presumably due to the small sample size of the Halls Bayou field (n=2), the proximity and the stratigraphic equivalence of the two fields).

For the 21 PGWD samples from 9 different oil fields within Test Area A the geothermal model yields a mean surface temperature of 16°C (range 15-16°C) and a mean geothermal gradient of 33°C/km (range 29-35°C/km) (fig. 8a). This is steeper than the geothermal gradient of 25.7°C/km which is determined using a surface temperature of 16°C and the subsurface temperature observations of Morton and Land (1987) for the upper 3 km of the Chocolate Bayou field. In contrast, using the same surface temperature (16°C), the more recent and detailed subsurface temperature measurements of Hyeong and Capuano (2001) for the Chocolate Bayou field yield a local gradient of 31°C/km (range 27-34°C/km)

which is more in Hyeong and Capuano's (2001) interpretation of the average local geothermal gradient (30°C/km) and this study's determination of the gradient for Test Area A (33°C/km).

Hyeong and Capuano (2001) suggest significant vertical variation in thermal gradients; samples from the West Columbia field have a high local gradient of 39°C/km (range 32-51°C/km), attributed primarily to high temperatures (43-58°C) recorded in samples from shallower Miocene Fm. (651-921m), that represent effective geothermal gradients between 40-51°C/km. Such vertical heterogeneities in thermal gradients for the TGC were noted by Morton and Land (1987). The high observed geothermal gradients for the Miocene Fm. are significantly greater than the maximum gradient (35°C/km) generated by the geothermal model for Test Area A. This comparison suggests that the methodology adopted here generates at-formation-depth temperatures broadly consistent with *in situ* observations, but also highlights potential limitations in the application of simple linear geothermal gradients in areas of complex hydrogeology.

Ground Truthing: Calcite-Dolomite Equilibrium in the Texas Gulf Coast Frio Formation
All 21 samples from Test Area A in the PWGD are from the Frio Fm. (fig. 7b). These samples are compared with Hyeong and Capuano (2001) data from the West Columbia (43-85°C; n=16) and Chocolate/Halls Bayou fields (94-150°C; n=35), the majority (88%) of which are also from the Frio Fm.. This area lies within the north-eastern TGC that is characterized by NaCl-type waters derived primarily from the dissolution of salt diapirs (Morton and Land, 1987). It is for these NaCl-type waters (Ca 1,490 mg/l, Ca/Mg molar ratios ~ 10) that Hyeong and Capuano (2001) interpret $\log_{10}(^{a}Ca^{2+}/^{a}Mg^{2+})$ - temperature trends to be consistent with the presence of calcite-dolomite equilibrium.

A primary concern of Hyeong and Capuano (2001) is evaluating the extent to which the relationship between $\log_{10}(^{a}Ca^{2+}/^{a}Mg^{2+})$ and temperature reflects either fluid mixing processes or water-rock reactions in the north-eastern TGC reservoirs. Comparing Ca, Mg against conservative ions Cl and Br, Hyeong and Capuano (2001) reasonably conclude that $\log_{10}(^{a}Ca^{2+}/^{a}Mg^{2+})$ values in both fields are unlikely to have resulted from mixing, despite active salt recrystallisation in the Frio Fm. (Morton and Land, 1987). They identify near identical $\log_{10}(^{a}Ca^{2+}/^{a}Mg^{2+})$-temperature relationships in both fields which are consistent with prior estimations of the calcite-dolomite equilibrium boundary. Any mixing that may have occurred is now irrelevant as calcite-dolomite equilibrium is (re)established in both fields. This interpretation would be inaccurate if mixing were to generate a calcite and/or dolomite undersaturated fluid within a host formation that lacks sufficient calcite and/or dolomite to enable the attainment of calcite-dolomite saturation, yet has $\log_{10}(^{a}Ca^{2+}/^{a}Mg^{2+})$ -temperature values serendipitously coincident with calcite-dolomite equilibrium. This situation may theoretically occur in very clean clastic formations. However, as the number of brine samples increases, there seems a very low probability that mixing can result in sizeable numbers of samples with near identical $\log_{10}(^{a}Ca^{2+}/^{a}Mg^{2+})$ - temperature values coincident with prior estimations of calcite-dolomite equilibrium yet out of equilibrium with either mineral. By extension, as the sample size increases, so does the confidence with which $\log_{10}(^{a}Ca^{2+}/^{a}Mg^{2+})$ - temperature profiles can reliably be converted into $K_{sp°-dol}$ values.

Combining data from the two fields Hyeong and Capuano (2001) construct a 2-term Maier-Kelley linear model (herein termed model A1) to determine the thermodynamic properties, including the ordering parameter (*s* = 0.4), of the local dolomite over a wide temperature range (43 - 150°C). Key model parameters for this literature model and all models constructed by this study are summarized in table 2 and fully reported in supplementary table 6.

Hyeong and Capuano (2001) use the following Maier-Kelly regression;

$$\log\frac{a\text{Ca}^{2+}}{a\text{Mg}^{2+}} = a + b\,\frac{T(°C)}{1000} \tag{28}$$

to determine the relationship between temperature and $\log_{10}(^a\text{Ca}^{2+}/^a\text{Mg}^{2+})$ (as calculated by SOLMNEQ88-Pitzer) evaluating a as -0.22 and b as 7.21 (model A1). We recalculate the Hyeong and Capuano (2001) dataset using a PHREEQC-Pitzer approach and (as with all models in this study) use the eq (25) Maier-Kelly regression formula (replacing the $\frac{T(°C)}{1000}$ term with T(K)). A two-term linear model (model A2) is almost identical to model A1 (fig. 9a). This indicates that a) PHREEQC-Pitzer determined activities are largely consistent with those determined by SOLMNEQ88-Pitzer analysis (supplementary figure 1), and b) the usage of different statistical packages and regression formulas generates relatively consistent results, including for goodness of fit measurements (model A1 R^2=0.94 and model A2 R^2=0.86).

Comparing mixed models of the recalculated Hyeong and Capuano (2001) dataset, a three-term Maier-Kelly expansion (model A3 AIC=-107.4) provides a better fit to the dataset than a two-term expansion (model A4 AIC=-84.4). However, given the small size of the dataset (n=51), three-term models (such as model A3) generate spurious extrapolations beyond the data range (fig. 9a). A two-term expansion is the regression formula used for small (n<400) individual and amalgamated datasets. There are minimal differences between the random intercept mixed model A4 and a random slope mixed model A5 (fig. 9a) including for group level results, and AIC favours model A4 (A4=-84.4 and A5=-77.1). Random slope models such as model A5 are likely to be a better representation of variations in $\log_{10}(^a\text{Ca}^{2+}/^a\text{Mg}^{2+})$-temperature relationships as, for example, fields are likely to see variations in local effects within different formations. However at present the causes for variations in $\log_{10}(^a\text{Ca}^{2+}/^a\text{Mg}^{2+})$-temperature gradients are poorly constrained and this type of model is not further evaluated at present.

Using linear models to separately (no pooling approach) evaluate the Chocolate/Halls Bayou (model B1, n=35) and West Columbia (model C1, n=16) fields reveals significant variations between the $\log_{10}(^a\text{Ca}^{2+}/^a\text{Mg}^{2+})$ - temperature profiles (fig. 8b). At 25°C $\log_{10}(^a\text{Ca}^{2+}/^a\text{Mg}^{2+})$ is 0.31 higher for the West Columbia field (model C1) whilst the $\log_{10}(^a\text{Ca}^{2+}/^a\text{Mg}^{2+})$ - temperature gradient is steeper for the Chocolate/Halls Bayou field (model B1). This reflects the inclusion of samples from the Miocene Fm. within the West Columbia field dataset. Comparing linear models of the separate formations (fig. 9c) suggests that Frio Fm. samples from both fields (model D1) are similar. Samples from the Miocene Fm. have a very different $\log_{10}(^a\text{Ca}^{2+}/^a\text{Mg}^{2+})$ trend with temperature (model E1), but the significance of this is limited (R^2 of -0.24) due to the small size (n=6) and limited temperature range (43-58°C) of samples from the Miocene Fm.

Hyeong and Capuano (2001) established the precedent of combining observations from different fields and formations to increase the reliability and temperature range of the model. Whilst this complete pooling approach is valid, there are several benefits (discussed above) from a mixed modelling (partial pooling) approach, particularly in modelling data from small groups, like the Miocene Fm., within large populations. Application of the mixed model approach to the Hyeong and Capuano (2001) dataset (n=51) (model A4) generates an adjusted ICC value of 0.441, indicating that grouping explains a significant amount of the variance (44.1%; good to fair reproducibility for grouped data – Rosner (2015)). As is expected for grouped data, the conditional R^2 of mixed model A4 (0.90) is larger than the marginal R^2 (0.83), indicating that the application of random effects improves model fit; note the marginal R^2 of the mixed model approximates the R^2 of the linear model A2 (0.84). Model A4 and model A2 have very similar profiles (fig. 9a) however the uncertainty is substantially larger for model A4. The standard error on the intercept $\log_{10}(^a\text{Ca}^{2+}/^a\text{Mg}^{2+})$ value rises from 1.49×10^{-1} log units for model A2 to 2.44×10^{-1} log units for model A4.

Similarly, the width of the 95% confidence interval at 25°C rises from 0.13 (model A2) to 0.39 (model A4) (fig. 9a). This is consistent with the view that uncertainty determined by a linear model can be an erroneous underestimate. However, AIC indicates that linear model A2 (-107.1) is better than the mixed model A4 (-84.4), reflecting the overparameterization of a limited number of samples/groups. For only marginally larger datasets, AIC values favour mixed models over linear models, though the statistical validity of mixed models may not be assured until group/sample size criteria are met.

Application of mixed modelling reduces the significant disparities between groups that are observed with linear modelling (models C1, B1, D1 and E1), though these remain and can be quantified through the group results (fig. 9b and c). For example, the difference in $\log_{10}(^aCa^{2+}/^aMg^{2+})$ values (at all temperatures as M4 is a random intercept model) between the Chocolate/Halls Bayou and West Columbia fields is 0.04 (model A4), which contrasts with the difference between the B1 (Chocolate/Halls Bayou) and C1 (West Columbia) linear models of 0.31 at 25°C (fig. 9b).

This study reports only the mixed model random intercept values for individual groups (supplementary table 7). These are not combined straightforwardly if a group-level result is required for multiple attributes/random effects but R is capable of generating $\log_{10}(^aCa^{2+}/^aMg^{2+})$-temperature for such models. For example the Chocolate/Halls Bayou field only contains Frio Fm. samples, however the profiles of the A4 mixed model results for the group with a single random effect of 'Chocolate/Halls Bayou field' (fig. 9b) and the group result for 'Chocolate/Halls Bayou field & Frio Fm.' (fig. 9c) are noticeably different. This apparent quirk is due to the influence of Frio Fm. from the West Columbia field which have higher $\log_{10}(^aCa^{2+}/^aMg^{2+})$ values on the mixed model shifting the group-level result.

In contrast to the Hyeong and Capuano (2001) dataset, and as commonly observed in the PWGD dataset, PWGD samples from Test Area A (n=21) do not sample multiple depths in each of the 9 fields. Typically, if multiple samples are taken from a field they are from a singular or narrow range of depths where production is focused. This reveals that the considerable range of depths within closely spaced fields is a major strength of the Hyeong and Capuano (2001) dataset. In contrast, the limited of coverage in the PWGD means that it is poorly suited to such single field analyses. However, we can demonstrate consistency between the $\log_{10}(^aCa^{2+}/^aMg^{2+})$ - temperature profile of the PWGD samples in Test Area A with those within the Hyeong and Capuano (2001) dataset (fig. 9d). The global-level results for the F1 mixed model of Test Area A PWGD samples (n=21) and the A4 global-level results of the Hyeong and Capuano (2001) dataset (n=51) are extremely similar with $\log_{10}(^aCa^{2+}/^aMg^{2+})$ differing at 25°C by just 0.01 log units. The geochemical consistency of the two sets of samples serves to support the reliability of the PWGD data. In addition, expanding upon Hyeong and Capuano (2001) this study interprets that $\log_{10}(^aCa^{2+}/^aMg^{2+})$ in all waters within Test Area A are buffered by calcite-dolomite equilibrium. Moreover, as $\log_{10}(^aCa^{2+}/^aMg^{2+})$ values for all fields are comparable, the local effects across all fields in Test Area A are interpreted to be similar suggesting related geological and hydrological histories for these proximal fields.

Ground Truthing: Calcite-Dolomite Equilibrium in the Texas Gulf Coast Frio Formation – Southern Texas to Central Louisiana

In comparison to samples solely from Text Area A, a larger sample set encompassing all Frio Fm. samples from southern Texas to central Louisiana (fig. 6a) within the PWGD (n=117, including the 21 samples in Test Area A) records significantly higher $\log_{10}(^aCa^{2+}/^aMg^{2+})$ values at lower temperatures with a greater overall scatter in $\log_{10}(^aCa^{2+}/^aMg^{2+})$ (fig. 9d). This is consistent with Morton and Land's (1987) interpretation that Frio Fm. sandstones throughout the TGC have a wide variation in geochemistry. Nine samples

(7.7% of all Frio samples) within the PWGD have $\log_{10}(^{a}Ca^{2+}/^{a}Mg^{2+})$ values greater than SUPCRT92 calcite-ordered dolomite equilibrium and are deemed very unlikely to be at calcite-dolomite equilibrium. These samples are all in the southern TGC, and are compositionally similar to CaCl-type waters (Ca 22,260mg/l, Ca/Mg molar ratios >100 identified by Morton and Land (1987)).

The Frio Fm. dataset (n=117) covers 48 fields but 35 fields have 2 or less samples, and the largest single field dataset (n=21 from the Seeligson field) only spans a 15°C temperature range (66-81°C). This precludes a single field analysis utilizing only Frio Fm. samples to evaluate the presence of calcite-dolomite equilibrium based on a consistent increase in $\log_{10}(^{a}Ca^{2+}/^{a}Mg^{2+})$ values with temperature. We suggest that despite the substantial scatter in $\log_{10}(^{a}Ca^{2+}/^{a}Mg^{2+})$ values for all Frio Fm. samples taken over a wide area the vast majority of Frio Fm. samples could still be interpreted as representing a calcite-dolomite equilibrium and that a broad range of local effects are operating and influencing local $\log_{10}(^{a}Ca^{2+}/^{a}Mg^{2+})$ values.

The global-level $\log_{10}(^{a}Ca^{2+}/^{a}Mg^{2+})$ for the mixed model (G1) of the entire PWGD Frio Fm. dataset is at 25°C +0.46 log units (albeit with a shallower gradient) in comparison to the A4 global-level value for Test Area A samples which represents a substantial difference (fig. 9d). Having established in Test Area A that low $\log_{10}(^{a}Ca^{2+}/^{a}Mg^{2+})$ values are indicative of calcite-dolomite equilibrium the question is therefore whether higher $\log_{10}(^{a}Ca^{2+}/^{a}Mg^{2+})$ values remain consistent with an interpretation of calcite-dolomite equilibrium and by extension the range of equilibrium $\log_{10}(^{a}Ca^{2+}/^{a}Mg^{2+})$ values.

Higher $\log_{10}(^{a}Ca^{2+}/^{a}Mg^{2+})$ values are supported by Hyeong and Capuano's (2001) interpretation that the formational brines in the Cretaceous Edwards group of south-central Texas (Land and Prezbindowski, 1981; fig. 9d) are at calcite-dolomite equilibrium. These brines (49-176°C) have an increase in $\log_{10}(^{a}Ca^{2+}/^{a}Mg^{2+})$ values with temperature consistent with that observed in the West Columbia and Chocolate/Halls Bayou fields, but have $\log_{10}(^{a}Ca^{2+}/^{a}Mg^{2+})$ values ~0.1 log units higher. The Edwards group primarily consists of dolomitized limestones and Hyeong and Capuano (2001) interpret these relatively higher $\log_{10}(^{a}Ca^{2+}/^{a}Mg^{2+})$ values to have resulted from the equilibration with a more ordered dolomite phase than that found in the West Columbia and Chocolate/Halls Bayou fields. As such Hyeong and Capuano, (2001) state that their model (model A1) is not valid for equilibrium between calcite and more ordered dolomite phases.

Ground Truthing: Thermal gradients in the Mississippi Salt Dome Basin
The Mississippi Salt Dome (MSD) basin is predominantly located in central Mississippi and is separated from the TGC basin to the south by the Wiggins, South Mississippi, and La Salle uplifts (arches). The MSD basin is characterised by substantial faulting and salt tectonics that trapped hydrocarbons. Kharaka and others (1987) sample (n=17) a range of clastic and carbonate Upper Cretaceous (Stanley Fm.) to Upper Jurassic (Norphlet Fm.) reservoirs (70-120°C) in 7 MSD basin fields. In contrast to the high-resolution Hyeong and Capuano (2001) study, the Kharaka and others (1987) dataset is relatively low resolution and only the Reedy (1920-3485m; 68-102°C; n=5) and Soso (1965-2875m; 68-89°C; n=3) fields sample over a wide depth/temperature range.

Test Area B, which encompasses the 7 fields sampled by Kharaka and others (1987), spans the Alabama-Mississippi border and has an area of 13,224km^2 (fig. 7c, bounding box W88°12'-W90°00'/N31°30'-N32°12'). For the 204 PGWD samples, from 35 different oil fields, contained within Test Area B the geothermal model yields a mean surface temperature of 13°C (range 12-14°C) and a mean geothermal gradient of 27°C/km (range 22-34°C/km) (fig. 8b). Assuming a surface temperature of 13°C, the mean geothermal gradient for the Kharaka and others (1987) dataset is calculated to be 26°C/km (25-29°C/km). This mean

geothermal gradient is comparable to the mean gradient predicted by this study's geothermal model (fig. 8b) suggesting that the 'average field' is comparable in both datasets. Moreover, samples from the Soso field at similar depth present in both datasets (at 2031m in the PWGD and 1965m in Kharaka and others, 1987) have predicted (this study) and observed (Kharaka and others, 1987) temperatures of 69°C and 68°C respectively, further validating the approach used in this meta-analysis to estimate local temperatures at-formation-depth.

At-formation depth temperatures predicted for Test Area B show a greater degree of scatter than those for Test Area A (fig. 7a). This probably reflects both a wider sampling area and, speculatively, the influence of salt domes, which can substantially modify local geothermal gradients (Daniilidis and Herber, 2017). In contrast to Test Area A where the majority of fields are located at least 15km away from any salt domes in Test Area B several fields, including the Raleigh and Soso fields, are proximal (<5km) to salt domes.

Ground Truthing: Calcite-Dolomite Equilibrium in the Central Mississippi Salt Dome Basin
The presence of calcite-dolomite equilibrium has been interpreted using two separate standards, ideally both being accompanied by mineralogical data indicating the presence of calcite and dolomite. Firstly the observation of an increase in $\log_{10}(^aCa^{2+}/^aMg^{2+})$ values with temperature that is broadly consistent with prior estimates of calcite-dolomite equilibrium (Land and Prezbindowski, 1981; Dutton, 1987; Hyeong and Capuano, 2001; Vespasiano and others, 2014; Blasco and others, 2018). Typically, the analysis has focussed on small areas such as a single field, to minimise systematic shifts in $\log_{10}(^aCa^{2+}/^aMg^{2+})$ - temperature due to local effects. This method of interpretating the presence of calcite-dolomite has typically only occurred when evaluating $K_{sp°-dol}$ and/or the order of the natural dolomite phase (see 'Solubility (groundwater), supplementary table 2).

More commonly calcite-dolomite equilibrium has been interpreted by evaluating saturation indices. Kharaka and others (1987) interpreted all samples (n=17) to be at (SOLMINEQ.87) calcite-dolomite equilibrium (-0.5<SI<0.5) and attribute the attainment of equilibrium to relate to the substantial dolomitization of the limestone Smackover Formation (Carpenter and Trout, 1978; Kharaka and others, 1987). Within the Kharaka and others (1987) dataset there are consistent increases in $\log_{10}(^aCa^{2+}/^aMg^{2+})$ values with temperature for both the Reedy and Soso fields (fig. 9d). The PWGD data from Test Area B (n=204) is quite similar to the Kharaka and others (1987) dataset, further supporting the reliability of the PWGD geochemical dataset. The mixed model of both the PWGD dataset (model I1) and the linear model (H1) of the Kharaka and others (1987) dataset are more similar to both the global-level results (G1) of the Frio Fm. than the A4 model of the Hyeong and Capuano (2001) dataset though all models typically intersect each other around ~120°C.

Expanding upon Kharaka and others (1987) and Hyeong and Capuano (2001) this study interprets that these high $\log_{10}(^aCa^{2+}/^aMg^{2+})$ waters present within the Edwards Group, Test Area B and most, but not all, of the Frio Fm. are consistent with an interpretation of calcite-dolomite equilibrium. The range of $\log_{10}(^aCa^{2+}/^aMg^{2+})$ values at a specific temperature that could reasonably be considered to be consistent with an interpretation of calcite-dolomite equilibrium is therefore wide, the width being further evaluated below, and attributed to local effects.

Distribution of samples in the PWGD
Geothermal model.—The highest spatial resolution of this study's geothermal model (fig. 6a) is in hydrocarbon-producing basins as oil and gas wells are the primary source for the SMUH dataset (fig. 6b; Blackwell and others, 2011). Ground truthing for two such data-rich areas suggests that at-formation-depth temperatures generated by this study's geothermal model are reliable for two local areas. Our model is based on the same data used by Blackwell and

others (2011) to produce interpolated maps (fig. 6c) for heat flow and temperatures at two specific depths (6.5km and 9.5km). Although the two are very similar, there are a number of disparities. For example, in parts of northern Virginia, where this study's geothermal model and the Blackwell and others (2011) model respectively resolve high and low geothermal anomalies. Significant differences between the models are typically in data poor areas (note the absence of data in Virginia) and likely reflect differences in interpolation technique. In comparison marginal differences are observed in higher resolution areas, such as in south Texas, where the Blackwell and others (2011) interpolation appears to resolve finer resolution geothermal features than this study's model, suggesting there may be scope to increase the lateral resolution of the geothermal model. As discussed for the Miocene Fm. samples in Test Area A, linear geothermal gradients can over-simplify thermal variations with depth. The BHT-Harrison corrected geothermal gradients from Blackwell and others (2011) are determined for each well; as each well can have a different depth two proximal wells could have significantly different geothermal gradients. Significantly more processing, outside the scope of this study, would be needed to generate a higher-resolution interpolated 3D temperature distribution. However, the down-sampling of gradients to 0.1°x0.1° Lat/Long areas (~95km^2 at 40° North) followed by a linear interpolation we interpret to generate reasonably robust geothermal gradients that average 28°C/km (σ = 6°C/km).

Geochemistry.—For the entire temperature range the $\log_{10}(^{a}Ca^{2+}/^{a}Mg^{2+})$-temperature frequency distribution is leptokurtic (kurtosis >3) for all PWGD samples (n=11,480, kurtosis=8.0). The sandstone, dolomite, and limestone lithologies, that together account for 94% of PWGD samples (supplementary table 4), have kurtosis values of 7.5, 8.4 and 8.6 respectively. Moreover, leptokurtic distributions are seen at all temperatures between 20-120°C for all PWGD samples, and for each of the three common lithologies (fig. 10d). For the small proportion (7%) of samples outside this temperature range (fig. 10g) kurtosis values are lower. However, kurtosis and skewness are parametric tests for which the underlying data must be relatively consistent with a normal distribution which is typically not the case for datasets with small numbers of samples (Rosner, 2015).

Leptokurtic values are reflective of the presence of significant numbers of outliers, as expected given that 10% of PWGD samples have $\log_{10}(^{a}Ca^{2+}/^{a}Mg^{2+})$ values above or below the upper and lower bounds of the SUPCRT92-Filter. Kurtosis reflects little about the distribution of samples within 1 σ from the mean and is a poor descriptor of the 'peakedness' of the data (Westfall, 2014). A better quantitative descriptor of the peakedness of a distribution is the standard deviation of the data.

All PWGD samples are binned into equal interval bins of dimensions 0.05 $\log_{10}(^{a}Ca^{2+}/^{a}Mg^{2+})$ x 10°C to further evaluate the frequency distribution of $\log_{10}(^{a}Ca^{2+}/^{a}Mg^{2+})$-temperature responses (fig. 10a). We find that typically (including for the three lithologies) σ in $\log_{10}(^{a}Ca^{2+}/^{a}Mg^{2+})$ for each 10°C bin (thus an overestimate) is ~ 0.3 log units which represents a surprisingly narrow interval. The $\log_{10}(^{a}Ca^{2+}/^{a}Mg^{2+})$ value at the peak of the distribution, through which the mixed models of the entire PWGD presented below intersect, increases with temperature in a manner consistent with prior evaluations of calcite-dolomite equilibrium. This is also reflected in the modal values of each lithology (fig. 10b). The high peaks of the frequency distribution, combined with the increase of $\log_{10}(^{a}Ca^{2+}/^{a}Mg^{2+})$ with temperature, are interpreted as strong evidence that the vast majority of groundwaters in the database are at calcite-dolomite equilibrium; were the distribution to have a significantly wider spread we would conclude that $\log_{10}(^{a}Ca^{2+}/^{a}Mg^{2+})$ values were buffered by surface phases. Moreover as the majority (90%, n=10,343/11,480) of PWGD samples have $\log_{10}(^{a}Ca^{2+}/^{a}Mg^{2+})$ values between the upper and lower bounds of the SUPCRT92-Filter the application of the SUPCRT92-Filter, to

remove samples unlikely to be at calcite-dolomite equilibrium, appears to be an appropriate statistical filter to increase the reliability of the $K_{sp°-dol}$ estimation.

For the dolomite, limestone and sandstone lithologies the frequency distributions appear to be largely unimodal and there does not appear to be any significant disparity between modal $\log_{10}(^aCa^{2+}/^aMg^{2+})$ values (fig. 10b). As we have interpreted that the primary control on $\log_{10}(^aCa^{2+}/^aMg^{2+})$ values is the dolomite composition this is taken to reflect a broad similarity in the most common dolomite composition sampled in all lithologies. Closely examining frequency distributions there is some evidence for the presence of additional modes. The clearest potentially multimodal distribution, the sandstone 80-90°C bin, appears to be bimodal with peaks at $0.35 < \log_{10}(^aCa^{2+}/^aMg^{2+}) \leq 0.4$ (n=40) and $0.6 < \log_{10}(^aCa^{2+}/^aMg^{2+}) \leq 0.65$ (n=40) (fig. 10i). Nevertheless support for the presence of systematic additional modes is principally weak because of the relatively small fraction of samples on the tails of the distribution. Meaningful identification of any additional modes is also challenged in many cases by significant numbers of repeat samples from a single depth/formation. Note that repeat measurements strengthen the weighting of a grouping and are well accounted for by mixed models.

In contrast to modal values which are generally similar for the main lithologies, mean $\log_{10}(^aCa^{2+}/^aMg^{2+})$ values (fig. 10c) for the limestone population are systematically higher than the dolomite population, particularly between 50-100°C (which contains 44% of all limestone- and 25% of all dolomite-hosted samples). This disparity is primarily due to the skewed distribution of the limestone population, which for 50-100°C is categorised (Bulmer, 1979) as either moderately (skewness between -1 and -0.5 or +1 and +0.5) or heavily (skewness <-1 or >1) skewed, with values up to +2.73 for the 60-70°C temperature bin (fig. 10e). A positive skew indicates that the tail of the frequency distribution of $\log_{10}(^aCa^{2+}/^aMg^{2+})$ values is thicker on the side with higher $\log_{10}(^aCa^{2+}/^aMg^{2+})$ values and that the modal $\log_{10}(^aCa^{2+}/^aMg^{2+})$ value < median < mean.

For all limestone samples the skewness is +0.57, which is significant in comparison to the approximately symmetric values (skewness between -0.5 and +0.5, Bulmer, 1979) of +0.11 and +0.18 for the sandstone and dolomite lithologies respectively and +0.25 for all the PWGD data. Tentatively, we infer the presence of a systematic local effect that causes a positive skew in the limestone population which can be interpreted in terms of dolomite stoichiometry. The modal equilibrium dolomite composition is interpreted to be somewhat calcian. Few dolomites are significantly more calcian (i.e. have lower equilibrium $\log_{10}(^aCa^{2+}/^aMg^{2+})$ values) than the modal composition. A substantial number of dolomites have compositions that are significantly more stoichiometric (i.e. have higher equilibrium $\log_{10}(^aCa^{2+}/^aMg^{2+})$ values) than the modal calcian dolomite composition, such that the mean $\log_{10}(^aCa^{2+}/^aMg^{2+})$ value is higher than the mode.

PWGD Mixed Modelling

This stage of the analysis focuses on developing a representative statistical model between $\log_{10}(^aCa^{2+}/^aMg^{2+})$ and temperature for the entire PWGD to determine a representative $K_{sp°-dol}$ value. To appropriately parameterize the mixed model of PWGD data (all models below utilize the SUPCRT92-filtered, n=10,343, dataset unless otherwise stated) the number of random effects utilized is incrementally increased. The extent to which a particular model over- or under-fits data is evaluated using goodness of fit measurements and the model selection justified. Moreover, we modify the classification scheme by which samples are categorized into different groups; specifically we evaluate the range of the depth interval into which samples are grouped.

With respect to fixed effects, in contrast to the ground-truthing sections, the larger PWGD dataset enables the use of 3-term Maier-Kelly mixed models, and this is the main

regression formulae used unless otherwise stated. AIC indicates a greater level of support for 4- and 5-term Maier-Kelly expansions however results for these higher order models are spurious, particularly when extrapolated outside the data range, and higher order models are not reported.

Grouping by depth.— We compare a series of mixed models of the PWGD dataset utilizing only the depth random effect (models J2-J9) but with varying depth interval widths. Beginning with a model with no depth-dependent grouping of samples (no. of depth groups=8201; AIC=-2754; model J2) increasing the depth interval width results in AIC values up to 300m (no. of depth groups=3,296; AIC=-3197; model J7). Thereafter AIC values decline with further increases in the grouping interval width out to a maximum reported here of 500m (no. of groups= 3,040; AIC=-3153; model J9). The peak AIC value for the 300m grouping interval suggests this is an optimal balance between over- and under-parameterization of the model.

A 300m grouping interval seems to be a reasonable, though perhaps somewhat large, depth range from a geological/hydrological perspective. However the vast majority of depth groups contain samples from a relatively narrow range of depths (typically <50m) which correspond to particular production zones. The main purpose of the depth random effect is to incorporate the variance attributable to repeat sampling of similar formational fluids over a narrow range of depths into the mixed model. In comparison to other models that utilize only a single random effect (models J10-J15) the depth-only random effect model is clearly the best model.

A secondary purpose for using the depth random effect is the potential to evaluate variations in $\log_{10}(^aCa^{2+}/^aMg^{2+})$ values at different depths in a field, by using group-level RI values. This maybe particularly useful in fields where there is a) a lack of detail about the formations present or b) there are thick sequences of an identical formation which are discretely stratified into isolated reservoirs with potentially different fluid compositions.

We exemplify the relevance and applicability of the depth grouping with the example of the Seeligson field, Texas (n=51) which has both samples from 2 well recognised formations, in this case the Frio Fm. (n=20) and the Vicksburg Fm. (n=1), and samples (n=30) that have one of 13 less informative production-related formational names such as '3300 Water Sand' (n=7) and 'A' (n=1). In contrast to grouping by one of 15 formations, grouping of samples by 300m depth intervals generates 8 different depth groups which reasonably collate samples from similar production horizons and formations. The Frio formation samples are primarily split into two groups; depth groups 'AT4' (n=5; depth range of samples=1.44km) and 'AT5' (n=13; depth range of samples=1.79-1.86km) which respectively correspond to the Seeligson production zones '14' (channel-fill deposits) and '20' (floodplain deposits with carbonate nodules noted) (Ambrose and others, 1992). With respect to the results from the reference model (model J21; global RI = -1.91); for the Seeligson field the RI value for the field is -1.81 whilst RI values for the 'AT4' and 'AT5' groups are -1.58 and -1.89 respectively. For the Seeligson field limited information about the lithological differences between these two zones makes it hard to interpret the cause of the RI variation. This lack of detailed mineralogical/lithological information is a common problem encountered by this meta-analysis, but this case of the Seeligson field highlights the method and processes by which we seek to evaluate variations in the dolomite composition.

Combining random effects.—In comparison to a linear model (AIC=-1455; model J1) of the PWGD data, all single random effect mixed models (models J10-J15) have larger AIC values affirming both the use of mixed models and these specific attributes as meaningful random effects. There is, however, only limited support for the time-period-only (AIC=-1457; model

J14) and time-series-only (AIC=-1501; model J15) models. Unlike other attributes for which completeness is either a criterion for inclusion in the dataset (such as the sample lithology), or are commonly reported (n=10,308/10,343 records have formation details), the PWGD subset possesses series/period interpretations for only 55/59% of samples. Whilst absent data is not an issue for mixed models this is likely a significant contributing factor in the relative weakness of the time-period and time-series random effects.

A general trend is observed that, as the spatial resolution/number of groups that describe the data increases, so also do AIC values. In increasing order of AIC values, the single random effect models are ranked; time-period model (13 period groups; AIC=-1457; model J14), time-series model (35 period groups; AIC=-1457; model J15), lithology model (5 lithology groups; AIC=-1524; model J13), basin model (53 basin groups; AIC=-1815; model J11), formation model (1228 formation groups; AIC=-2640; model J12), field model (2,168 field groups; AIC=-2828; model J10), and the 300m interval depth model (3,296 depth groups; AIC=-3197; model J7). There are two exceptions; 1) the depth-only model with no sample groupings (model J2) has a lower AIC value than the field-only model (model J10). The lower AIC reflects the overparameterization and highlights the benefit of the implementation of the depth interval groupings, 2) the lithology model (model J13) appears to better characterise the data than the time-period (model J14) and time-series (model J15) models.

In contrast to the nested data structure with respect to basin-field-depth attributes, the lithology, time period and formation operate as partially crossed random effects. Random effects are completely crossed if there are samples present with every combination of values of the random effects; for example for a model in which the time period random effect is completely crossed with the field random effect, the field would need to have samples from every time period. This is clearly not the case and the partially crossed terminology describes the presence of some degree of nesting. The formation random effect in some cases, such as the Tensleep Fm. (n=659) which spans multiple basins (Big Horn, Central Montana Uplift, Denver, Green River, Powder River, Wind River and Yellowstone) will be substantially crossed against the basin and field random effects whilst in other cases, particularly local formations such as those related to production, will be completely nested within a single field.

Systematically combining multiple random effects, both model fit and the capability to reliably describe a wide a variety of sample attributes are progressively improved. As the number of random effects implemented changes so do the group-level results as variance is attributed to different random effects. The best fitting (as determined by AIC) model, the reference model (AIC=-3595; model J21), utilizes all 7 random effects (depth, field, basin, formation, lithology, time-period and time-series). AIC values are only marginally (i.e. <5) smaller for the 4-random effect (Depth-Field-Basin-Formation; -3591; model J18) and 5-random effect (Depth-Field-Basin-Formation-Lithology; -3590; model J19) mixed models, indicating some level of support for these models. However, the inclusion of lithology and time-period/time-series random effects have a relatively minimal effect on both the group-level and global-level results and the inclusion of these random effects is clearly not penalized by AIC for overparameterization. As such, the 7-random effect model (model J21) is selected as the representative model.

The global level model results are relatively stable across all models; the linear model (model J1) reports a $pK_{sp°-dol}$ of -17.24±0.36, with $pK_{sp°-dol}$ values marginally decreasing as additional random effects are added, such that the reference model (J21) has a $pK_{sp°-dol}$ of -17.27±0.35. The width of the confidence intervals also reduces as mixed models incorporate increasing numbers of random effects. The maximum confidence interval width is shared by the lithology and time period single random effect models (±0.45; models J13 and J14).

Whilst the confidence intervals are almost identical for the linear (model J1) and reference mixed model (model J21), this is arguably coincidental as discussed earlier uncertainty estimates for grouped data as calculated by linear models are unreliable (and the R statistical method which generates uncertainties is different for both models). The ICC value for the reference model J21 is 46.6% (good to fair reproducibility for grouped data – Rosner (2015)), which indicates that grouping is indeed significant for PWGD data. Results from single and multiple (2-5) random effect models are not further analysed and we focus primarily on results of the 7-random effect reference model (model J21), as changes in group-level and global-level results are insignificant between the different mixed models.

Reference model J21/J23: Global level results.— Expressed in terms of the fixed effects the 7-random effect representative model that describes calcite-dolomite equilibrium $\log_{10}(^{a}Ca^{2+}/^{a}Mg^{2+})$ values (model J21) is;

$$\log_{10}\left(\frac{aCa^{2+}}{aMg^{2+}}\right) = -1.92 - 5.84 \times 10^{-3} \cdot T(K) - 1.41 \times 10^{2} \cdot \frac{1}{T(K)} \qquad (29)$$

The Maier-Kelly expression for pK_{sp-dol} is more widely applicable. Each individual $\log_{10}(^{a}Ca^{2+}/^{a}Mg^{2+})$ value is converted to a pK_{sp-dol} value using SUPCRT92 pK_{sp-cal} (table. 1). A mixed model (model J23) is then constructed using these pK_{sp-dol} values using the same formulation, 7-random effects and 3-term Maier-Kelly, as model J21;

$$pK_{sp-dol} = 1.47545 \times 10^{1} - 6.24959 \times 10^{-2} \cdot T(K) - 3.99350 \times 10^{3} \cdot \frac{1}{T(K)} \qquad (30)$$

Converting back to equilibrium $\log_{10}(^{a}Ca^{2+}/^{a}Mg^{2+})$ values, using pK_{sp-cal} values from SUPCRT92, the values (model J23) are largely identical to model J21 (table 2; fig. 5a) though at temperatures >200ºC $\log_{10}(^{a}Ca^{2+}/^{a}Mg^{2+})$ values tend sharply lower which is likely to primarily be a function of extrapolation outside of the data range and we suggest that the validity of this study's constant is limited to temperatures <200ºC. For model J23, both the global and group-level results correspond directly to model J21 results.

DISCUSSION

The primary observation from this study is an overall increase in $\log_{10}(^{a}Ca^{2+}/^{a}Mg^{2+})$ with temperature for the majority of subsurface fluids in the contiguous continental states. Between 25°C to 200°C the representative model (J23) determines that US groundwaters, with $\log_{10}(^{a}Ca^{2+}/^{a}Mg^{2+})$ values between the SUPCRT92-Filter (n=10,343), show a +0.85 log unit increase in $\log_{10}(^{a}Ca^{2+}/^{a}Mg^{2+})$. Model K1 is identically parameterized to the reference model (model J21) but includes samples outside the range of the SUPCRT92-Filter (n=11,480). Between 25°C to 200°C model K1 determines a +0.52 log unit increase in $\log_{10}(^{a}Ca^{2+}/^{a}Mg^{2+})$ values, suggesting that the increase in $\log_{10}(^{a}Ca^{2+}/^{a}Mg^{2+})$ values is not an artifact of the implementation of the SUPCRT92-Filter (fig. 5a).

Calcite is, arguably, the most common and ubiquitous carbonate phase in rocks. Assuming any Mg present in the fluid is conservative and has a depth-independent constant concentration, equilibrium only with calcite whose solubility varies with temperature (retrograde solubility) could generate a $\log_{10}(^{a}Ca^{2+}/^{a}Mg^{2+})$ response with temperature. We simulate $\log_{10}(^{a}Ca^{2+}/^{a}Mg^{2+})$ values between 25°C to 200°C using PHREEQC (Pitzer database) of a solution, buffered only by calcite, with a constant concentration of Mg (0.01 M) and ionic strength (0.85 M – buffered by NaCl) that reflects the median ionic strength and Mg concentration of PWGD waters (supplementary table 5). The model determines that equilibrium $\log_{10}(^{a}Ca^{2+}/^{a}Mg^{2+})$ values increase by + 0.10 log units over this temperature range from -1.34 to -1.23 log units. Though a significant increase in the Mg content could increase

$\log_{10}(^aCa^{2+}/^aMg^{2+})$ values, in comparison over this temperature range model J21/J23 $\log_{10}(^aCa^{2+}/^aMg^{2+})$ values are substantially different increasing from +0.28 to +1.15 (+0.85 log units) consistent with a variety of literature estimations of the calcite-dolomite equilibrium (fig. 5b).

Although there appear to be few other mechanisms that can consistently buffer a wide variety of fluids to such a coincidental $\log_{10}(^aCa^{2+}/^aMg^{2+})$ - temperature profile, we further evaluate this interpretation in two ways. Firstly, we critique the interpretations of Möller and De Lucia (2020) who suggest that $\log_{10}(^aCa^{2+}/^aMg^{2+})$ values are reflective only of buffering with Mg-calcite surface phases. Secondly, we address other potential sources of error and local variations that could affect $\log_{10}(^aCa^{2+}/^aMg^{2+})$ - temperature profiles. Finally, we compare this study's estimates of the average dolomite's thermodynamic property with prior studies.

Comparison to the Möller and De Lucia (2020) meta-analysis.— The only significant previous meta-analysis of groundwater compositions from the perspective of calcite-dolomite equilibrium is that of Möller and De Lucia (2020) who consider 242 samples from 17 regions around the world. They similarly find that fluids from a wide variety of lithologies and locations have $\log_{10}(^aCa^{2+}/^aMg^{2+})$ values that are intermediate with respect to the SUPCRT92-filter. However, for the majority of subsets of the different locations they observe $\log_{10}(^aCa^{2+}/^aMg^{2+})$ -temperature profiles to be non-parallel (in some cases orthogonal) to the reference calcite-dolomite equilibria (SUPCRT92). They argue this is indicates a variety of Mg-calcite surface phases buffer $\log_{10}(^aCa^{2+}/^aMg^{2+})$ values to a wide range.

Möller and De Lucia (2020) recognise that a sizeable minority of their samples have $\log_{10}(^aCa^{2+}/^aMg^{2+})$ -temperature profiles that are parallel to the reference calcite-dolomite equilibria (SUPCRT92). These include those from the Red Sea, Meizar Wells/Yarmouk Gorge (Israel/Jordan), and the MSD basin. Nevertheless the presence of calcite-dolomite equilibrium is discounted, with an alternative, non-specific interpretation for these sites citing/invoking differences in environmental conditions and the exchange of Mg^{2+} due to reaction with siliceous rocks or sediments. The MSD basin dataset modelled and dismissed as lacking evidence for calcite-dolomite equilibrium is from Kharaka and others (1987). Our expanded analysis of samples contained in Test Area B strengthens the Kharaka and others (1987) interpretation of calcite-dolomite equilibrium buffering these waters.

The Meizar Wells/Yarmouk gorge dataset is from Siebert and others (2014) and Siebert and others (in prep). The dominant lithology in the Yarmouk gorge is limestone and, though Siebert and others (2014) mention that limestones are altered and interpret calcite-dolomite equilibrium for springs at the Shamir Artesian location, information of the diagenetic alteration of local carbonate aquifers is sparse. Most wells in the Siebert and others (2014) database appear to sample the Turonian-Cenomanian Ajloun group. Locally, dolomitization is identified in one well (Mukheibeh 4) in the upper part of the Ajloun group (Inbar and others, 2019). Slightly further south this group is described as primarily being composed of dolomitized shallow/restricted marine mudstone/wackestones, with dolomite typically replacing micrite and fairly fine grained (Khalifa and Abed, 2010). Evaluating the Meizar Wells/Yarmouk gorge dataset using the recorded temperatures (rather than estimating temperatures at-formation-depth), the $\log_{10}(^aCa^{2+}/^aMg^{2+})$ - temperature trend does appear to be consistent with a calcite-dolomite interpretation (fig. 9f). However, samples with temperatures <25°C show a significant scatter, and their removal results in a substantial improvement in goodness of fit for simple 2-term (Maier-Kelly) linear models. Including samples <25°C the R^2 is 0.05 and the p-value is 0.08 (model L1; n=42), whilst removing six samples with temperatures <25°C the R^2 rises to 0.38 and the p-value falls to 4.23×10^{-5} (model M1; n=36). This indicates that unlike model L1, model M1 can

explain much of the variation in the dataset (high R^2) and the model is significant (low p-value).

There appears to be a divide in the Möller and De Lucia (2020) dataset whereby regional subsets with temperatures >30°C show $\log_{10}(^aCa^{2+}/^aMg^{2+})$ -temperature trends largely parallel to the reference calcite-dolomite equilibria (SUPCRT92), whilst those with temperatures <30°C have non-parallel $\frac{aCa^{2+}}{aMg^{2+}}$ -temperature relationships. Only 22% of the samples (n=54) in the Möller and De Lucia (2020) dataset have recorded depths, with the majority appearing to be samples from relatively low temperature surface springs. This is reflected in the average sample temperature of the Möller and De Lucia (2020) samples of 32.4°C (a standard deviation of 24°C), which is substantially lower than this studies' average at-formation-depth temperature of 61.9°C (standard deviation of 29°C).

In contrast to this study, Möller and De Lucia (2020) determine $\log_{10}(^aCa^{2+}/^aMg^{2+})$ at the recorded sample temperature and do not try to evaluate the temperature at-formation-depth. The discrepancy between a recorded sample temperature and a likely at-formation-depth temperature increases with depth. For example, for the North East German basin Möller and De Lucia (2020) determine $\log_{10}(^aCa^{2+}/^aMg^{2+})$ values for samples from Tesmer and others (2007). Samples from <500 m depth (n=15, from 233±79m) have recorded temperatures that are lower than those from >500m depth (n=5, from 1298±258m), with average values of 17±12°C and 30±18°C respectively. Based on an average geothermal gradient of 32°C/km (Agemar and other, 2012) and an average surface temperature of 4°C (MAST), we calculate at-formation-depth temperatures for the average depths of 233m and 1298m to be 11°C and 45.5°C, respectively. Although the use of averages masks inherent variability, the aim here is to illustrate how thermal equilibration of samples at the surface leads to, in this case, over-estimation of temperatures for shallow samples and, more critically, under-estimation of temperatures for deeper samples. The most extreme example of this is from the Rheisberg well where $\log_{10}(^aCa^{2+}/^aMg^{2+})$ is determined at 16.6°C for a sample taken from 1600 m. Such inaccuracies in temperature have a minimal effect on $\log_{10}(^aCa^{2+}/^aMg^{2+})$ values as the temperature dependencies of Ca^{2+} and Mg^{2+} activities as calculated by Pitzer are identical. However, it imperative to contextualize $\log_{10}(^aCa^{2+}/^aMg^{2+})$ values with reference to the temperature at which equilibrium was established (at-formation-depth) to properly evaluate the $\log_{10}(^aCa^{2+}/^aMg^{2+})$ - temperature relationship.

The samples in the Möller and De Lucia (2020) meta-analysis are derived from both surface springs and boreholes, which we argue require separate methods of estimating at-formation-depth temperatures. For borehole samples Hyeong and Capuano (2001) utilize at-formation-depth temperatures taken at the well perforation during the formation shut in test or, lacking that data, from corrected well log measurements. This study's much larger meta-analysis uses a new geothermal model to estimate at-formation depth temperatures. Both Hyeong and Capuano (2001) and this study have good controls on the reservoir depth, which is assumed to be the depth at which equilibrium $\log_{10}(^aCa^{2+}/^aMg^{2+})$ values were established. We suggest that meaningful analysis of spring water samples requires a rigorous geothermometrical approach, as exemplified by Chiodini and others (1995), Vespasiano and others (2014), and Blasco and others (2018), who evaluate the dolomite order (supplementary table 2) and the temperature at which spring waters samples were last at equilibrium (saturated) using multiple reference minerals (such as calcite, dolomite, anhydrite, quartz, and feldspar) and isotopes. The $\log_{10}(^aCa^{2+}/^aMg^{2+})$ values for the reference J21 model of the PWGD data and global observations of groundwater are extremely similar supporting both the global applicability and methodology of this study. The difference between J21 and Hsu (1963), Hyeong and Capuano (2001), Vespasiano and others (2014), Blasco and others (2018) studies is +0.20 (25°C), +0.35 (at 25°C, though the difference reduces with increasing temperature), -0.01 (67°C), and -0.05 (80°C) respectively (fig. 5b).

Reflecting the PWGD's focus on oil production, there are relatively few low temperature (typically shallow) samples in the PWGD; the 25th percentile sample depth and temperature are 1.3 km and 39.6°C respectively (supplementary table 5). However for 20°C < T ≤ 30°C the PWGD distribution remains peaky and leptokurtic (the kurtosis for all samples is 13.6) suggesting that where residence times are long, such as in oil traps, calcite-dolomite equilibrium can be established even at these low temperatures. Hypothetically, substantial $\log_{10}(^aCa^{2+}/^aMg^{2+})$ scatter may still be present for spring water samples, particularly those that have circulated briefly at shallow depths and equilibrated at lower temperatures, as residence times may not be significantly greater than the 32 years over which Land (1998) failed to precipitate dolomite at 25°C. Lower temperatures kinetically hinder calcite-dolomite equilibration (certainly through precipitation of dolomite), such that $\log_{10}(^aCa^{2+}/^aMg^{2+})$ values are more likely to be scattered and potentially indicative of buffering by Mg-surface carbonate phases.

Sources of Local Effects

We evaluate the potential mechanisms that could control $\log_{10}(^aCa^{2+}/^aMg^{2+})$-temperature profiles including the presence of any common ion equilibria, kinetic effects on equilibrium/the residence time of the solution, the ionic strength and the solution composition, composition of the equilibrium calcite and dolomite phases, and other conceivable sources of error. We consider the implications of these mechanisms to modify a sample's the unique $\log_{10}(^aCa^{2+}/^aMg^{2+})$-temperature both at local scale and for the entire PWGD population.

A) Equilibrium with additional minerals.— Aside from equilibrium with Mg-surface phases there appear no other mineral equilibria that can buffer $\log_{10}(^aCa^{2+}/^aMg^{2+})$ values to the range observed by this study. However, the addition of any other minerals bearing Ca, Mg or CO_3 could conceivably generate substantial changes to the solubility of either calcite or dolomite in an equilibrium solution due to the common-ion effect. For the common ion effect to be significant the additional compound must have a solubility somewhat comparable to either calcite or dolomite. We evaluate the extent to which additional mineral phases can modify $\log_{10}(^aCa^{2+}/^aMg^{2+})$ values.

The illitization of smectite and albitization of feldspar, processes which release Mg and Ca respectively, have been variably discounted as significant processeses in modifying fluid compositions by both Hyeong and Capuano (2001) and Kharaka and others (1987). These diagenetic processes, which are particularly common in TGC sediments, are irreversible (at diagenetic temperatures) and therefore cannot buffer $\log_{10}(^aCa^{2+}/^aMg^{2+})$ values. The addition of Mg or Ca to the solution through either illitization or albitization will be buffered by calcite-dolomite equilibrium, and, assuming the buffering occurs faster than the release of Ca or Mg, the $\log_{10}(^aCa^{2+}/^aMg^{2+})$ values will remain constant. Illitization, in particular, may act as a source of Mg for dolomitization. As none of the minerals involved are particularly soluble there is also a negligible common ion effect.

Chlorite group minerals such as clinochlore ($Mg_5Al_2Si_3O_{10}(OH)_8$) are more soluble and of interest with respect to a potential common ion effect. Hyeong and Capuano (2001) conclude chlorite is unlikely to be a significant buffer in Frio Fm. sediments as though chlorite is abundant, it is only found in samples with at-formation-depth temperatures >90°C and there is no discrepancy in $\log_{10}(^aCa^{2+}/^aMg^{2+})$ values above and below 90°C.

We have evaluated the solubility of various chlorite group members at 25, 50, 75 and 150°C using PHREEQC with the LLNL and the Thermoddem (Blanc and others, 2012) databases for 0.1M NaCl buffered solutions in equilibrium with calcite and dolomite.

Hereafter, unless otherwise stated, we model dolomite using model J23 as a phase in PHREEQC. Clinochlore is present in both the Thermoddem and the LLNL database, but the latter contains two separate variants, clinochlore-14A and clinochlore-7A, which have identical formula but slightly different solubility constants. The phase clinochlore-14A was determined to be broadly similar in solubility to chlorite from Flagstaff Hill, California termed 'Chlorite (CCa-2)' (Zhang and others, 2015) and incorporated in the Thermoddem database. The Thermoddem database also includes another chlorite group mineral, sudoite ($Mg_2Al_4Si_3O_{10}(OH)_8$).

In solutions buffered solely by calcite and dolomite, all of the aforementioned chlorite phases are very insoluble. At 25°C, every kg of water will dissolve 1.056×10^{-4} moles of calcite, 1.062×10^{-4} moles of dolomite, and just 2.095×10^{-7} moles of sudoite (the most soluble chlorite phase). In comparison in the absence of sudoite the amounts of calcite (1.051×10^{-4} moles) and dolomite (1.065×10^{-4} moles) that dissolve are similar. For simulations with and without sudoite $\log_{10}(^aCa^{2+}/^aMg^{2+})$ values are 0.31. As the other chlorite phases (Chlorite (CCa-2), Clinochlore-14A and Clinochlore-7A) are more insoluble than sudoite, their effect on carbonate dissolved and $\log_{10}(^aCa^{2+}/^aMg^{2+})$ values is even smaller. Where the solution is buffered to lower pH values, such as in equilibrium with a CO_2 saturated brine, substantial dissolution of chlorite can occur (Zhang and others, 2015). This mechanism of Mg release is interesting both from the perspective of CO_2 sequestration, but also as a mechanism of generating Mg-rich fluids in sandstones that may drive dolomitization.

Ca-sulphates such as anhydrite ($CaSO_4$) are common in the subsurface and more soluble than either calcite or dolomite thus potentially could affect $\log_{10}(^aCa^{2+}/^aMg^{2+})$. Again, we evaluate equilibrium conditions at 25, 50, 75 and 150°C using PHREEQC with the Thermoddem database in a 0.1M NaCl buffered solution. At 25°C, for every kg of water 1.205×10^{-2} moles of dolomite and 3.775×10^{-2} moles of anhydrite dissolve. Meanwhile 2.407×10^{-2} moles of calcite precipitate due to the common ion effect as anhydrite is more soluble. However, $\log_{10}(^aCa^{2+}/^aMg^{2+})$ values remain at 0.31, the same as simulations involving only calcite and dolomite (see above), confirming that equation (5) is the primary control on fluid compositions where calcite and dolomite occur together.

The capacity of calcite-dolomite equilibrium to buffer $\log_{10}(^aCa^{2+}/^aMg^{2+})$ values does not appear to influenced by the addition of any other minerals bearing Ca or Mg. Mg-sulfates, such as epsomite ($MgSO_4{:}7H_2O$), are even more soluble than anhydrite and PHREEQC modelling suggests that calcite-dolomite-epsomite equilibrium cannot be established as the end state solution will be undersaturated in either epsomite or calcite. In situations where calcite remained (and epsomite completely dissolved) $\log_{10}(^aCa^{2+}/^aMg^{2+})$ values were consistent with simulations involving only calcite and dolomite.

Cation exchange with mixed-layer illite/smectite could also act to buffer $\log_{10}(^aCa^{2+}/^aMg^{2+})$ values. Hyeong and Capuano (2001), though noting the presence of mixed-layer illite/smectite, discount this effect in the Frio Fm., whilst Dutton (1987) and Engle (2014) suggest that the variable release of Ca^{2+} and Mg^{2+} ions, as Na^+ is adsorbed, is a key mechanism modifying San Andres Fm. brines and resulting in low $\frac{[Na^+]}{[Cl^-]}$ molar ratios. Variation in the clay composition results in a differences in the release Ca^{2+} and Mg^{2+} and could therefore buffer $\log_{10}(^aCa^{2+}/^aMg^{2+})$ values to a range of values. This is challenging to model using thermodynamic codes but we evaluate this process in future work.

B) Kinetic considerations and approach to equilibrium.— The approach to calcite-dolomite equilibrium from either conditions of supersaturation or undersaturation will result in $\log_{10}(^aCa^{2+}/^aMg^{2+})$ ratios varying around $pK_{sp°-dol}$ in a quasi-static equilibrium distribution.

For example, if the solution is supersaturated with respect to calcite but undersaturated with respect to dolomite, $\log_{10}(^aCa^{2+}/^aMg^{2+})$ will decrease as calcite-dolomite equilibrium is approached through dedolomitization (calcite precipitating at the expense of dolomite). The quasi-static equilibrium distribution (Hefter and Tomkins, 2003) around $pK_{sp°-dol}$ is a function between the time for the fluid to equilibrate in a given environment and the residence time of the fluid. The systematic positive skew observed in the PWGD dataset (fig. 10e) could indicate that equilibrium is more frequently approached from conditions of dolomite undersaturation.

This may reflect a systematic decrease in at-formation-depth temperatures in sedimentary basins after peak burial temperatures. Thus, as temperatures increase during burial, to maintain calcite-dolomite equilibrium $\log_{10}(^aCa^{2+}/^aMg^{2+})$ increases and this typically (being a function of K_{sp-dol} and K_{sp-cal}) corresponds to an increase in dolomite precipitation at the expense of calcite. Peak burial temperatures correspond to peak dolomite abundance. Thereafter, a decrease in at-formation-depth temperatures is reflected in a decrease in equilibrium $\log_{10}(^aCa^{2+}/^aMg^{2+})$ values and dedolomitization. This component of the variation in $\log_{10}(^aCa^{2+}/^aMg^{2+})$ may be relevant for short residence time spring waters, but negligible for samples from wells that have residence times orders of magnitude greater than laboratory-estimated rates of dolomitization.

For test area B the calcite-dolomite equilibrium is attributed to the dolomitization of the limestone Smackover Fm. (Kharaka and others, 1987), yet the fluids are hosted in adjacent sandstones units. Notwithstanding the potential of sandstone units to attain calcite-dolomite equilibrium (as is clearly demonstrated by Hyeong and Capuano, 2001), there exists a scenario, similar to that described earlier with respect to a theoretical clean clastic formation, whereby fluids that have attained calcite-dolomite equilibrium move into clean clastic formations and the $\log_{10}(^aCa^{2+}/^aMg^{2+})$ value remains frozen at the prior value. This situation is particularly problematic when the fluids in the new formation are now undersaturated with respect to calcite and/or dolomite. If the flow is vertical this could then give an anomalous $\log_{10}(^aCa^{2+}/^aMg^{2+})$ value for the reservoir temperature. Moreover, given the retrograde solubility of both calcite and dolomite this scenario is most plausible when fluids migrate upwards. Whilst chemically possible, this effect is not thought to be of practical significance as the distribution of the sandstone population in the PWDB closely mirrors that of the carbonate populations (fig. 10).

C) Ionic strength\solution composition.—There is a differential impact of the ionic strength and solution composition on the separate activities of Ca^{2+} and Mg^{2+} in solution. The strength and specificity of the ion-ion interactions are dissimilar due to separate Pauling ionic radii for the ions, 72pm for Mg^{2+} and 100pm for Ca^{2+} (Ulfsbo and others, 2015). The ion-ion interactions are complex and solved for each ion by the Pitzer model.

We evaluate calcite-dolomite equilibrium at a range of ionic strengths and in both monovalent (NaCl) and divalent (Na_2SO_4) background electrolytes (fig. 11). For both background electrolytes as the ionic strength increases so also do aCa^{2+} and aMg^{2+} values, though the rates of increase are identical for both ions such that $\log_{10}(^aCa^{2+}/^aMg^{2+})$ values are constant for both background electrolytes and at all ionic strengths. This is because calcite-dolomite equilibrium (eqs 5 and 8) buffers solutions to a constant $\log_{10}(^aCa^{2+}/^aMg^{2+})$ value. However, as Ca ion-ion interactions are stronger than Mg ion-ion interactions, with an increase in ionic strength the concentration of Ca^{2+} increases faster than that of Mg^2 to maintain an equivalent aCa^{2+}.

This interpretation that $\log_{10}(^aCa^{2+}/^aMg^{2+})$ values at calcite-dolomite equilibrium are largely insensitive to both the ionic strength and the solution composition is supported by both experimental and groundwater data. For experiments conducted at 200°C Baker and

Kastner (1981), also referencing the experimental data of Rosenberg and Holland (1964), determine that calcite-dolomite equilibrium exists at higher $\frac{[Ca^{2+}]}{[Mg^{2+}]}$ molar ratios at higher ionic strengths. Though they do not evaluate activities, this relationship is consistent with that predicted by thermodynamic modelling (fig. 11).

Hyeong and Capuano (2001) noted substantially different $\log_{10}(^aCa^{2+}/^aMg^{2+})$ values, yet identical ionic strengths, for the Edwards group and the Smackover Fm. brines (the differences attributed to variations in the dolomite phase). The increases in TDS with depth are also substantially different for both the Chocolate/Halls Bayou (from 33g/L to 132g/L) and West Columbia (from 61g/L to 99g/L) fields yet the $\log_{10}(^aCa^{2+}/^aMg^{2+})$ - temperature profiles, as previously discussed, are extremely similar. Möller and De Lucia (2020) also interpret for their global brine dataset (n=242) that the ionic strength of a solution has a negligible influence on $\log_{10}(^aCa^{2+}/^aMg^{2+})$.

We modify the reference model (J21) to additionally include ionic strength (I) as a fixed effect such that the Maier-Kelly formula of the fixed effect terms is;

$$\frac{aCa^{2+}}{aMg^{2+}} = a + bT + \frac{c}{T} + I \qquad (31)$$

This mixed model (J22) determines there to be a 0.007 log unit decrease in $\log_{10}(^aCa^{2+}/^aMg^{2+})$ values per 1 mol/kgw increase in the ionic strength. AIC finds some support (model J22; -3600) for this model in comparison to the reference model (model J21; -3595.4). The relatively minimal decrease in $\log_{10}(^aCa^{2+}/^aMg^{2+})$ values confirms that ionic strength has a negligible effect on calcite-dolomite equilibrium $\log_{10}(^aCa^{2+}/^aMg^{2+})$ values and as such model J22 incorporating ionic strength is not used as the reference model.

Baker and Kastner (1981) note slower rates of dolomitization at lower ionic strengths. Thus the slight decrease in $\log_{10}(^aCa^{2+}/^aMg^{2+})$ values with increasing ionic strength may potentially reflect a kinetic effect that may be sufficient to inhibit attainment of equilibrium, albeit this seems improbable due to long residence times. It is more likely to reflect variation in the composition of the equilibrium dolomite phase; Kaczmarek and Sibley (2011) observe variations in the end state dolomite ordering/composition based on the initial solution composition.

D) Error.—There is likely to be a component of normally distributed random measurement error which is assumed to be normally distributed and incorporated into a formulation of the mixed model by the error term, ε , and thus is of little interest. Systematic errors are of more concern and there are a number of potential sources.

Errors in the geothermal model for calculating at-formation depth temperatures could produce significant variations in $\log_{10}(^aCa^{2+}/^aMg^{2+})$-temperature values. However extensive ground truthing at both high-resolution local scales and a continental scale have established temperatures at-formation depths are broadly in line with literature data.

There is no weighting in the model for samples taken earlier in the production history which may reflect compositions closer to the original connate fluid. The injection of water to stimulate production (waterflooding) from sources other than formation of interest (recycled water) - such as oceans, rivers or separate aquifers - may result in a significant calcite-dolomite disequilibrium for the new mixed fluid which does not resolve on production timescales. Similarly, CO_2 injection of CO_2 , H_2S or mixed gases for the purpose of reservoir stimulation may generate a calcite-dolomite disequilibrium and may significantly effect common ion minerals such as chlorite (see section A above). Han and others (2010) document changes to the fluid composition and the saturation indices of calcite (SI=0.80 → 0.62) and dolomite (SI=2.55 → 2.44) as production shifts from the waterflooding to the CO_2 injection phases in the Cisco and Canyon formations of the Scurry Area Canyon Reef

Operations Committee (SACROC) Unit in the Midland basin, Texas. This pattern of production, with the initial dilution of the formation water, reflected in a drop in the average Na^+ from 27,292 to 24,249 mg/l, and later significant CO_2 injection is a production history common across many basins. Time series analysis may enable further study of mineral dissolution-precipitation kinetics in response to induced disequilibrium. At present it is unclear how much variation in $\log_{10}(^aCa^{2+}/^aMg^{2+})$ values can be attributed to production influences, though Engle and Blondes (2014) offer a solution that could potentially be used to filter samples through the use of principal component analysis.

An additional source of error could relate to the determination of activities by the PHREEQC-Pitzer model. There is a marginal systematic difference in $\log_{10}(^aCa^{2+}/^aMg^{2+})$ values determined by this study, which are higher than those from the Hyeong and Capuano (2001) SOLMINEQ88-Pitzer analysis (supplementary figure 1). The difference in calculated $\log_{10}(^aCa^{2+}/^aMg^{2+})$ values appears to be more pronounced for lower temperature (Miocene Fm.) samples, though this could also be a function of changes in the background fluid compositions which are differently evaluated owing to changes/updates in the Pitzer model incorporating new speciation data. This increases confidence in the $\log_{10}(^aCa^{2+}/^aMg^{2+})$-temperature values calculated here as, whilst the intercept of any model, such as J21, may shift in response to the implementation of new Pitzer activity model, the gradient is unlikely to change significantly.

E) Composition of the dolomite and calcite phase.— Modelling the solubility of LMC (eq 22; 0-300°C), the effect on equilibrium $\log_{10}(^aCa^{2+}/^aMg^{2+})$ for this study's model J23 $K_{sp°-dol}$ is relatively minimal (fig. 5a). In comparison to the value of $pK_{sp°-cal}$ at 25°C, the $pK_{sp°-cal(4\%MgCO_3)}$ for a LMC phase consisting of 4% $MgCO_3$ (upper bound of LMC) that results from ideal mixing between calcite and magnesite (SUPCRT92 phases; table 2) is +0.018 log units higher. Equation 8 dictates that the +0.018 log units increase in the value of $pK_{sp°-cal(4\%MgCO_3)}$ results in an increase of +0.036 log units in the equilibrium $\log_{10}(^aCa^{2+}/^aMg^{2+})$; a +0.036 log unit increase in equilibrium $\log_{10}(^aCa^{2+}/^aMg^{2+})$ values translates to an identical (+0.036 log unit) increase in the estimated value for $pK_{sp°-dol}$. For reference, this is an order of magnitude smaller than the uncertainty associated with this studies reference model J21 ($pK_{sp°-dol}$ = -17.27±0.35), suggesting that the Mg-composition of the equilibrium calcite phase is unlikely to significantly inhibit an accurate determination of $pK_{sp°-dol}$.

The deviation from ideal mixing between $CaCO_3$ and $MgCO_3$ associated with the behaviour of Mg-calcite being closer in reality to being a non-ideal solid solution, will increase the solubility of the Mg-calcite phase and by extension equilibrium $\log_{10}(^aCa^{2+}/^aMg^{2+})$ values. The determination of the thermodynamic properties of non-ideal Mg-calcite across a wide range of temperatures is desirable (though complex). However, at temperatures 50°C ≤ T ≤ 100°C the solubilities of $CaCO_3$ and $MgCO_3$ are very similar. At 73°C $K_{sp°-cal}$ ≡ $K_{sp°-mag}$, which should also be the temperature at which non-ideal behaviour approaches a minimum, while for the ideal LMC model 73°C is the temperature at which $K_{sp°-cal}$ ≡ $K_{sp°-cal(4\%MgCO_3)}$(fig. 5a). At lower (T < 73°C) and higher (T > 73°C) temperatures the calculated $pK_{sp°-dol}$ values are likely to be slight under- and over-estimates respectively. The 25th and 75th percentiles of the PWGD subsurface temperatures are 349.6°C and 79.0°C respectively, suggesting that the majority of sample temperatures should be close to those at which the non-ideal behaviour of Mg-calcite nears a minimum. Overall we suggest that it seems reasonable to determine $K_{sp°-dol}$ assuming a pure calcite end-member.

Were Ca substitution into dolomite ideal, a calcian dolomite with 2% $CaCO_3$ would modify the reference model (model J21) $pK_{sp°-dol}$ from -17.27 to -17.10 which, when in

equilibrium with SUPCRT92-calcite, translates to a difference in $\log_{10}(^aCa^{2+}/^aMg^{2+})$ values of -0.17 (fig. 5a). The greater the calcian composition of the dolomite phase, the lower the $\log_{10}(^aCa^{2+}/^aMg^{2+})$ values for a given temperature. The effect on equilibrium $\log_{10}(^aCa^{2+}/^aMg^{2+})$ values is clearly substantially larger in magnitude than that associated with Mg substitution into calcite but on the same scale Helgeson and others (1978) estimated for substitutional order in dolomite.

Local effects summary.— Whilst acknowledging the potential contributions to $\log_{10}(^aCa^{2+}/^aMg^{2+})$ from sources reviewed above, we suggest that the primary cause of variations in $\log_{10}(^aCa^{2+}/^aMg^{2+})$ values is the dolomite composition.

The primary challenges for this interpretation are reconciling the frequency distributions of natural dolomite compositions (Sperber and others, 1984) with $\log_{10}(^aCa^{2+}/^aMg^{2+})$ values and interpreting the mean $\log_{10}(^aCa^{2+}/^aMg^{2+})$ and values on the shoulders of the distribution in terms of the dolomite composition. This is more extensively evaluated in a separate study.

Mixed Model Global Level Analysis

The reference model (model J21) $\log_{10}(^aCa^{2+}/^aMg^{2+})$-temperature profile (fixed effects) appears to be broadly consistent with a wide variety of prior models that evaluate K_{sp-dol} over a range of temperatures, including the most recent experimental study of Bénézeth and others (2018), the groundwater study of Hyeong and Capuano (2001) and the thermodynamic profiles of Blanc and others (2012) and Miron and others (2017) (fig. 5b). Firstly, the global level fixed effect results are compared to the prior models, highlighting comparison to Bénézeth and others (2018). Thereafter we consider the limitations of mixed models and compare uncertainties to literature. Lastly the thermodynamic properties of the dolomite that reflects the average composition of the PWGD database are determined.

Literature Comparison.— The best method of determining the solubility of a mineral phase is under controlled experimental conditions, and the study of Bénézeth and others (2018) represents the experimental study that is most recent, utilizes the widest experimental range of temperatures (53-253°C) and approaches K_{sp-dol} from conditions of both under- and super-saturation. At reference state conditions (25°C) the $pK_{sp°-dol}$ value of -17.27±0.35 from the reference model (model J23) is comparable to the -17.19±0.3 of Bénézeth and others (2018). However, at temperatures >50°C the models diverge (fig. 5b) until at 200°C the Bénézeth and others (2018) model has a pK_{sp-dol} of -24.02 which is much lower than both this study (model J23) and the ordered dolomite phase of Helgeson and others (1978) which have pK_{sp-dol} values of -23.26 and -23.71 respectively at 200°C. As the divergence is most significant at high temperatures where dolomite solubility is lower (though achieved quicker) we suggest the accurate characterisation of these equilibrium solutions containing lower concentrations of $Ca^{2+}/Mg^{2+}/CO_3^{2-}$ is much more sensitive to measurement error. Moreover, Bénézeth and others (2018) do not leverage the benefits in terms of accurately calculating activities in solution through the use of a thermodynamic program. Möller and De Lucia (2020) re-evaluate the Bénézeth and others (2018) dataset using PHREEQC and determine the pK_{sp-dol} at 200°C to be either -24.7 (llnl.dat) or -25.5 (pitzer.dat). In summary the calcite-dolomite equilibrium $\log_{10}(^aCa^{2+}/^aMg^{2+})$ values generated by the Bénézeth and others (2018) model appear to be spurious in comparison to other profiles (fig. 5b), a poor fit for the $\log_{10}(^aCa^{2+}/^aMg^{2+})$ distribution in PWGD groundwaters, and the highly plausible re-evaluation by Möller and De Lucia (2020), that results in an even more insoluble estimate for dolomite solubility, means the Bénézeth and others (2018) model appears to be unreliable.

We concur with the interpretation of Möller and De Lucia (2020) that the experimental solution of Bénézeth and others (2018) is likely to be primarily buffered by Mg-surface phases. We interpret bulk mineral thermodynamic equilibrium between calcite and dolomite to have been established in long residence time groundwaters, and this is reflected in the global consistency of $\log_{10}(^aCa^{2+}/^aMg^{2+})$- temperature profiles and pK_{sp-dol} values, determined through the groundwater approach (fig. 5b and 9f).

Partial pooling issues.— The partial-pooling approach of mixed modelling, which previously we have advocated as a strength and the ideal compromise between the complete- and no-pooling extremes, has an inherent flaw. Mixed modelling weights groups based on sample sizes, with greater confidence in group-level effects for groups with larger numbers of samples. Groups with smaller sample sizes, and potentially quite different $\log_{10}(^aCa^{2+}/^aMg^{2+})$ - temperature profiles, are judged to carry less information. This has two effects which we exemplify with respect to Test Area A and the Hastings field, a representative field from Test Area A;

1) The population average is more heavily influenced by larger groups. As increasing amounts of high $\log_{10}(^aCa^{2+}/^aMg^{2+})$ data is added to the mixed models there is an increase in the average $\log_{10}(^aCa^{2+}/^aMg^{2+})$ intercept and a decrease in the $\log_{10}(^aCa^{2+}/^aMg^{2+})$ - temperature gradient. This is most notable for the F1 (n=21) and G1 (n=117) models which utilize datasets that comprise respectively Frio Fm. samples from Test Area A that have low $\log_{10}(^aCa^{2+}/^aMg^{2+})$ values (model F1; n=21; $\log_{10}(^aCa^{2+}/^aMg^{2+})$ = -0.01 at 25°C) and the larger set of Frio Fm. samples including those in Test Area A (model G1; n=117; $\log_{10}(^aCa^{2+}/^aMg^{2+})$ = 0.48 at 25°C) which generally have higher $\log_{10}(^aCa^{2+}/^aMg^{2+})$ values (fig. 9d). When considering a representative model for dolomite this is not a problem as the frequency distribution of $\log_{10}(^aCa^{2+}/^aMg^{2+})$ data (fig. 9a and 10) indicates that Test Area A samples have much lower $\log_{10}(^aCa^{2+}/^aMg^{2+})$ values than the PWGD population average.

2) A more significant issue is that RI values for small groups, such as individual fields, will tend closer towards the population average. Samples from the Hastings field (n=4; T=73-76°C) are all from the Frio Fm. and have similar $\log_{10}(^aCa^{2+}/^aMg^{2+})$ - temperature values to other fields in Test Area A (fig. 9d). The Test Area A model (model F1), Frio Fm. model (model G1), and the reference model (model J21) contain a progressively larger number of samples that are not from the Hastings field (and typically have higher $\log_{10}(^aCa^{2+}/^aMg^{2+})$ values). As such the group-level results for $\log_{10}(^aCa^{2+}/^aMg^{2+})$ values (at 25°C) for the Hastings field increase as the population size increases with values of 0.00, 0.21, and 0.23 for F1, G1 and J21 models respectively (fig. 9d). The G1 and J21 group-level model results for the Hastings field do not overlap the Hastings data and these group-level models clearly do not represent the significant divergence of the Hastings data from the population average.

The reference model (model J21) RI value for the Hastings field group is one of the lowest of all fields in the PWGD (RI=-1.98; 2149th lowest RI value out of 2167 fields) yet there is only an offset of 0.07 in $\log_{10}(^aCa^{2+}/^aMg^{2+})$ values from the model J21 population average. RI values are interpreted to be useful as a comparative tool and meaningful relative to one another and the population average. A separate study evaluates group-level results from this relativistic perspective. As shown for the Hastings field, the reference model (model J21) RI values are unlikely to accurately reflect the underlying group-level data and by extension the composition of the local dolomite phase even though, as previously discussed, samples from Test Area A are interpreted to be at calcite-dolomite equilibrium and $\log_{10}(^aCa^{2+}/^aMg^{2+})$ values can theoretically span a wide range depending on the composition of the equilibrium dolomite phase (fig. 5a). At present group-level models,

whilst likely to better reflect dolomite solubility for a given group are likely to be far from accurate models particularly for groups with $\log_{10}(^aCa^{2+}/^aMg^{2+})$ values that are significantly different to the global-level model. This is clearly highly desirable for potential future geochemical modelling applications and future work could address this by application of a Bayesian framework that better preserves information on small sample size groups.

Mixed model uncertainty.— Bénézeth and others (2018) determine an uncertainty for their estimate of K_{sp-dol} (-17.19±0.3) through combining estimates of experimental uncertainties and this is described as a 3 standard deviation uncertainty (confidence interval of 99.7%). Whilst this method may indicate the accuracy of individual measurements of K_{sp-dol}, it reflects neither the uncertainty of the experimental data as determined by the statistical model (the three term Maier-Kelly regression), nor the uncertainty of an extrapolation.

The lowest experimental temperature used by Bénézeth and others (2018) is 53°C, yet the uncertainty for the extrapolated value of $pK_{sp°-dol}$ at 25°C is reported as ±0.3 (99.7% confidence interval level). We model the Bénézeth and others (2018) dataset, specifically the activities as determined by Bénézeth and others (2018) (not those determined by Möller and De Lucia (2020)), using a 3-term linear model (N1) with uncertainty evaluated using 95% confidence intervals. At 25°C this $pK_{sp°-dol}$ is 17.18±0.53 whilst at 100°C (and generally for values inside of the experimental range of Bénézeth and others (2018)) the pK_{sp-dol} is -19.50±0.15 (fig. 5b). Clearly the uncertainty associated with the Bénézeth and others (2018) model extrapolated to reference state conditions is significantly greater than estimated by Bénézeth and others (2018) and we argue that the use of confidence intervals is a better measure of the temperature dependence of model uncertainty.

As the uncertainty associated with the J21 reference model ($pK_{sp°-dol}$ = -17.27±0.35) is comparable to the experimental Bénézeth and others (2018) uncertainty, it seems reasonable to suggest that a $pK_{sp°-dol}$ determined using groundwater data could broadly be considered to be no less uncertain than experimental data.

Thermodynamic properties of reference dolomite model.— For the three-term Maier-Kelly formula (eq 25) the *a*, *b* and *c* coefficients can be converted into the ΔG_r°, ΔH_r° and $\Delta C_{p,r}^\circ$ thermodynamic properties of dolomite as follows (Bénézeth and others, 2018);

$$\Delta G_r^\circ = -R \ln(10)\,(aT + bT^2 + c) \tag{32}$$

$$\Delta H_r^\circ = R\,T\,\ln(10)\,(bT^2 - c) \tag{33}$$

$$\Delta C_{p,r}^\circ = 2R\,T\,\ln(10)\,b \tag{34}$$

For model J23 the coefficients *a*, *b*, and *c* have values of 1.47545×10^1, -6.24959×10^{-2}, and -3.99350×10^3 respectively, which equate to values of ΔG_f°, ΔH_r°, and $C_{p,r}^\circ$ of -2161.34 ± 8.26 kJ mol^{-1}, -2329.61 ± 0.51 kJ mol^{-1}, and 82.04 ± 12.17 J mol^{-1}K^{-1} respectively. These values of ΔG_r° and ΔH_r° are broadly comparable to prior estimations (supplementary table 2); ΔG_r° ranges from -2147.82 ± 2.20 kJ mol^{-1}(Rock and others, 2001) to -2171.75 kJ mol^{-1} (Blasco and others, 2018) whilst ΔH_r° ranges from -2315.89 kJ mol^{-1} (Morrow and others, 1994) to -2332±3 kJ mol^{-1} (Chai and Navrotsky, 1993). However, the $C_{p,r}^\circ$ value is substantially lower than the literature estimates which range from 154.2±2 (Benezeth and others, 2018) to 157.74 J mol^{-1}K^{-1} (Johnson and others, 1992).

Whilst a single inaccurate thermodynamic property, in particular the $C_{p,r}^{\circ}$, does not render other parameters to be in error, following the method of Bénézeth and others (2018), $C_{p,r}^{\circ}$ can be fixed to a constant and the model refitted. Based on a $C_{p,r}^{\circ}$, of $157.51 \text{ J mol}^{-1}\text{K}^{-1}$ (Robie and Hemingway, 1995) which is representative of literature estimates, we set the b coefficient to a value of -0.06919 and the refitted model (model J24) determines the a and c coefficients to be 1.93×10^1 and -4.75×10^3 respectively. These equate to relatively minor shifts in the values of ΔG_r° and ΔH_r° to $-2161.4 \pm 0.66 \text{ kJ mol}^{-1}$ and -2332.67 ± 0.34 respectively.

Between 25 and 150°C there is a relatively minimal difference (fig. 5a) between the two models (models J23 and J24) with the greatest divergence primarily occurring at temperatures >230°C where PWGD data is sparse (fig. 9a). To better constrain $C_{p,r}^{\circ}$ would require modelling a mixed groundwater – experimental dataset that incorporates more high temperature data. However even at temperatures >150°C there persist a wide range of thermodynamic estimates; at 200°C Bénézeth and others (2018) evaluate pK$_{sp-dol}$ to be -24.02$\pm$0.3 compared to -22.21$\pm$0.14 from Baker and Kastner (1981). Unlike estimates of ΔG_r° and ΔH_r°, $C_{p,r}^{\circ}$ is extremely sensitive to the $\log_{10}(^a\text{Ca}^{2+}/^a\text{Mg}^{2+})$ - temperature gradient; notice that the small difference between the gradients of models J23 and J24 (fig. 5a). Whilst higher temperature data may help constrain $C_{p,r}^{\circ}$ further, arguably the groundwater meta-analysis methodology appears to be the least appropriate method for determining $C_{p,r}^{\circ}$ as the noise appears to smooth out these trends. The use of single fields, some of which show steep increases of $\log_{10}(^a\text{Ca}^{2+}/^a\text{Mg}^{2+})$ with temperature, maybe a more appropriate method to accurately estimate $C_{p,r}^{\circ}$, and variations thereof, though the inclusion criteria would need careful justification to avoid selection bias.

CONCLUSIONS

This meta-analysis of the U.S. Geological Survey National Produced Waters Geochemical Database V2 (PWGD) reconstructs at-formation-depth temperatures for each sample (n=11,480) using a new geothermal model that combines subsurface geothermal gradients and mean annual land surface temperature measurements. After screening to ensure quality, the $\log_{10}(^a\text{Ca}^{2+}/^a\text{Mg}^{2+})$ of each sample was evaluated using PHREEQC with the Pitzer database.

- Ground-truthing at-formation-depth temperatures and $\log_{10}(^a\text{Ca}^{2+}/^a\text{Mg}^{2+})$ values to areas of the Texas Gulf Coast basin (Test Area A) and Mississippi Salt Dome basin (Test Area B) we find both are consistent with prior studies suggesting both the new geothermal model and PWGD are reliable data sources.
- The $\log_{10}(^a\text{Ca}^{2+}/^a\text{Mg}^{2+})$-temperature relationship of the vast majority (at least 90%) of subsurface waters in the US, and probably globally, are interpreted to be indicative of calcite-dolomite equilibrium.
- Equilibria with bulk mineral compositions rather than Mg-calcite surface phases is thought to control $\log_{10}(^a\text{Ca}^{2+}/^a\text{Mg}^{2+})$ values. Deviations in $\log_{10}(^a\text{Ca}^{2+}/^a\text{Mg}^{2+})$ values are interpreted to primarily reflect variations in the composition of the equilibrium dolomite phase.
- Other mineral-based processes that might influence $\log_{10}(^a\text{Ca}^{2+}/^a\text{Mg}^{2+})$ values, including equilibration with anhydrite, chlorite group minerals, illitization of smectite, albitization of feldspar are considered but found to be of minor or no significance. Similarly the ionic strength of the solution is not found to be significant.

We identify a subset (n=10,343) of samples which have $\log_{10}(^aCa^{2+}/^aMg^{2+})$ values that are intermediate with respect to SUPCRT92 calcite - ordered dolomite and calcite - disordered dolomite reference equilibriums and are judged most likely to be at calcite-dolomite equilibrium. For this data, the mixed model (models J21/J23) describes both a global population average composition, reported here as the solubility constant for natural dolomite (eqs 2 and 30), and group random intercept values that describe the deviation in $\log_{10}(^aCa^{2+}/^aMg^{2+})$ values away from the global population average for subsets sharing common attributes, such as a common field from which samples are taken (supplementary table 7). The solubility product constant and observations of $\log_{10}(^aCa^{2+}/^aMg^{2+})$ values reported here compare well with both experimentally derived data and groundwater observations. Considering the group random intercept values and the deviation in $\log_{10}(^aCa^{2+}/^aMg^{2+})$ values away from the global population average may offer a novel route for evaluating the stoichiometry of subsurface dolomites.

References

Agemar, T., Schellschmidt, R. and Schulz, R., 2012. Subsurface temperature distribution in Germany. *Geothermics*, *44*, pp.65-77.

Aines, R.D., Wolery, T.J., Bourcier, W.L., Wolfe, T. and Hausmann, C., 2011. Fresh water generation from aquifer-pressured carbon storage: feasibility of treating saline formation waters: *Energy Procedia*, v. *4*, p. 2269-2276.

Althoff, P.L., 1977. Structural refinements of dolomite and a magnesian calcite and implications for dolomite formation in the marine environment: *American Mineralogist*, v. *62*(7-8), p. 772-783.

Al-Helal, A.B., Whitaker, F.F. and Xiao, Y., 2012. Reactive transport modeling of brine reflux: dolomitization, anhydrite precipitation, and porosity evolution. *Journal of Sedimentary Research*, *82*(3), pp.196-215.

Ambrose, W.A., Grigsby, J.D., Hardage, B.A., Langford, R.P., Jirik, L.A., Levey, R.A., Collins, R.E., Sippel, M., Howard, W.E. and Vidal, J., 1992. *Secondary gas recovery: targeted technology applications for infield reserve growth in fluvial reservoirs in the Frio Formation, Seeligson field, South Texas. The University of Texas at Austin, Bureau of Economic Geology*. Topical Report GRI-92/0244, Gas Research Institute, Chicago, Illinois.

Anderson, G.M. and Crerar, D.A., 1993. *Thermodynamics in geochemistry: the equilibrium model*. Oxford University Press on Demand.

André, L., Audigane, P., Azaroual, M. and Menjoz, A., 2007. Numerical modeling of fluid-rock chemical interactions at the supercritical CO2-liquid interface during CO2 injection into a carbonate reservoir, the Dogger aquifer (Paris Basin, France): *Energy Conversion and Management*, v. *48*(6), p. 1782-1797.

Antao, S.M., Mulder, W.H., Hassan, I., Crichton, W.A. and Parise, J.B., 2004. Cation disorder in dolomite, CaMg (CO3) 2, and its influence on the aragonite+ magnesite↔ dolomite reaction boundary: *American Mineralogist*, v. *89*(7), p. 1142-1147.

Baker, P.A. and Kastner, M., 1981. Constraints on the formation of sedimentary dolomite: *Science*, v. *213*(4504), p. 214-216.

Barin, I., 1989. Thermochemical data of pure substances. New York, *VCH Publishers*.

Barin, I., 1995. Thermochemical data of pure substances Third Edition. New York, *VCH Publishers*.

Barnes, I. and Back, W. (1964) Dolomite solubility in ground water: *U.S. Geological Survey Prof. Paper 475-D, v.* 160, p. 179–180.

Bates, D., Maechler, M., Bolker, B. and Walker, S., 2014. lme4: Linear mixed-effects models using Eigen and S4: R package version 1.1-7, p. 1-23.

Bechtel, B., 2015. A new global climatology of annual land surface temperature: *Remote Sensing*, v. *7*(3), p. 2850-2870.

Beckman, J.D. and Williamson, A.K., 1990. *Salt-dome locations in the Gulf Coastal Plain, south-central United States* (Vol. 90, No. 4060). US Geological Survey.

Bell, B.A., Morgan, G.B., Schoeneberger, J.A., Loudermilk, B.L., Kromrey, J.D. and Ferron, J.M., 2010, April. Dancing the sample size limbo with mixed models: How low can you go: *SAS Global Forum,* v. 4, p. 11-14.

Bénézeth, P., Berninger, U.N., Bovet, N., Schott, J. and Oelkers, E.H., 2018. Experimental determination of the solubility product of dolomite at 50–253 ℃: *Geochimica et Cosmochimica Acta*, v. *224*, p. 262-275.

Benjakul, R., Hollis, C., Robertson, H.A., Sonnenthal, E.L. and Whitaker, F.F., 2020. Understanding controls on hydrothermal dolomitisation: insights from 3D reactive transport modelling of geothermal convection: *Solid Earth*, *11*(6), pp.2439-2461.

Bischoff, W.D., Bertram, M.A., Mackenzie, F.T. and Bishop, F.C., 1993. Diagenetic stabilization pathways of magnesian calcites: *Carbonates and Evaporites*, v. *8*(1), p. 82-89.

Blackwell, D., Richards, M., Frone, Z., Batir, J., Ruzo, A., Dingwall, R. and Williams, M., 2011. *Temperature-at-depth maps for the conterminous US and geothermal resource estimates* (GRC Transactions 35. GRC1029452). Southern Methodist University Geothermal Laboratory, Dallas, TX (United States).

Blanc, P., Lassin, A., Piantone, P., Azaroual, M., Jacquemet, N., Fabbri, A. and Gaucher, E.C., 2012. Thermoddem: A geochemical database focused on low temperature water/rock interactions and waste materials. *Applied geochemistry*, *27*(10), pp.2107-2116.

Blasco, M., Gimeno, M.J. and Auqué, L.F., 2017. *Comparison of different thermodynamic databases used in a geothermometrical modelling calculation*: *Procedia Earth and Planetary Science*, v. 17, p. 120–123.

Blasco, M., Gimeno, M.J. and Auqué, L.F., 2018. Low temperature geothermal systems in carbonate-evaporitic rocks: Mineral equilibria assumptions and geothermometrical calculations. Insights from the Arnedillo thermal waters (Spain): *Science of The Total Environment*, v. *615*, p. 526-539.

Blondes, M.S., Gans, K.D., Rowan, E.L., Thordsen, J.J., Reidy, M.E., Engle, M.A., Kharaka, Y.K. and Thomas, B., 2016. US Geological Survey National Produced Waters Geochemical Database v2. 2 (PROVISIONAL) Documentation. *USGS Energy Resources Program: Produced Waters, USGS*, *16*.

Bradley, W.F., Burst, J.F. and Graf, D.L., 1953. Crystal chemistry and differential thermal effects of dolomite: *American Mineralogist: Journal of Earth and Planetary Materials*, v. *38*(3-4), p. 207-217.

Bragg, W.L. and Williams, E.J., 1934. The effect of thermal agitation on atomic arrangement in alloys: *Proceedings of the Royal Society of London. Series A, Containing Papers of a Mathematical and Physical Character*, v. *145*(855), p. 699-730.

Bucher, K. and Grapes, R., 2011. Metamorphism of dolomites and limestones. In *Petrogenesis of Metamorphic Rocks* (pp. 225-255). Springer, Berlin, Heidelberg.
Bulmer, M.G., 1979. *Principles of statistics*. Courier Corporation.

Burnham, K.P. and Anderson, D.R., 2002. A practical information-theoretic approach. *Model selection and multimodel inference, 2nd ed. Springer, New York*, 2.

Busenberg, E. and Plummer, N., 1982. The kinetics of dissolution of dolomite in CO2-H2O systems at 1.5 to 65oC and 0 to 1 atm PCO2: *American Journal of Science*, v. *282*(1), p. 45-78.

Carpenter, A.B., and Trout, M.L., 1978. Geochemistry of bromide-rich brines of the Dead Sea and Southern Arkansas. Oklahoma Geol. Surv., Circ.; USA; DA., v. 79, p. 78-88.

Chai, L. and Navrotsky, A., 1993. Thermochemistry of carbonate-pyroxene equilibria: *Contributions to Mineralogy and Petrology*, v. *114*(2), p. 139-147.

Chai, L., Navrotsky, A. and Reeder, R.J., 1995. Energetics of calcium-rich dolomite: *Geochimica et Cosmochimica Acta*, v. *59*(5), p. 939-944.

Chaikin, P.M., Lubensky, T.C. and Witten, T.A., 1995. *Principles of condensed matter physics* (Vol. 1). Cambridge: Cambridge university press.

Chernosky, J.V. and Berman, R.G., 1989. Experimental reversal of the equilibrium: clinochlore+ 2 magnesite= 3 forsterite+ spinel+ 2 CO 2+ 4 H 2 O and revised thermodynamic properties for magnesite: *American Journal of Science*, v. *289*(3), p. 249-266.
Chiodini, G., Frondini, F. and Marini, L., 1995. Theoretical geothermometers and PCO2 indicators for aqueous solutions coming from hydrothermal systems of medium-low temperature hosted in carbonate-evaporite rocks. Application to the thermal springs of the Etruscan Swell, Italy: *Applied Geochemistry*, v. *10*(3), p. 337-346.

Chou, L.E.I., Garrels, R.M. and Wollast, R., 1989. Comparative study of the kinetics and mechanisms of dissolution of carbonate minerals: *Chemical geology*, v. *78*(3-4), p. 269-282.

Daniilidis, A. and Herber, R., 2017. Salt intrusions providing a new geothermal exploration target for higher energy recovery at shallower depths. *Energy*, *118*, pp.658-670.

Debure, M., Lerouge, C., Warmont, F., Bocher, L., Lundy, M., Madé, B. and Grangeon, S., 2021. On the interaction between calcite and dolomite: Insights from gas and aqueous geochemistry and mineralogical characterization. *Chemical Geology*, 559, p.119921.

Deelman, J.C., 2003. *Low-temperature formation of dolomite and magnesite*. Eindhoven: Compact disc publications.

Derkani, M.H., Fletcher, A.J., Fedorov, M., Abdallah, W., Sauerer, B., Anderson, J. and Zhang, Z.J., 2019. Mechanisms of surface charge modification of carbonates in aqueous electrolyte solutions: *Colloids and Interfaces*, v. *3*(4), p. 62.

Dickson, J.A.D., 1995. Paleozoic Mg calcite preserved: Implications for the Carboniferous ocean: *Geology*, v. *23*(6), p. 535-538.

Dutton, A.R., 1987. Origin of brine in the San Andres Formation, evaporite confining system, Texas Panhandle and eastern New Mexico. *Geological Society of America Bulletin*, *99*(1), pp.103-112.

Engle, M.A. and Blondes, M.S., 2014. Linking compositional data analysis with thermodynamic geochemical modeling: oilfield brines from the Permian Basin, USA: *Journal of Geochemical Exploration*, v. *141*, p. 61-70.

Fang, Y. and Xu, H., 2018. Study of an Ordovician Carbonate with Alternating Dolomite–Calcite Laminations and Its Implication For Catalytic Effects of Microbes On the Formation of Sedimentary Dolomite. *Journal of Sedimentary Research*, *88*(6), pp.679-695.

Fang, Y. and Xu, H., 2019. A new approach to quantify the ordering state of protodolomite using XRD, TEM, and Z-contrast imaging: *Journal of Sedimentary Research*, v. *89*(6), p. 537-551.

Rosner, B., 2015. *Fundamentals of biostatistics*. Nelson Education.

Gamsjäger, H., Königsberger, E. and Preis, W., 2000. Lippmann diagrams: theory and application to carbonate systems: *Aquatic Geochemistry*, v. *6*(2), p. 119-132.

Garrels, R.M. and Drever, R.M., 1952. Mechanism of limestone replacement at low temperatures and pressures: *Geological Society of America Bulletin*, v. *63*(4), p. 325-380.

Garrels, R.M., Thompson, M.E. and Siever, R., 1960. Stability of some carbonates at 25 degrees C and one atmosphere total pressure: *American Journal of Science*, v. *258*(6), p. 402-418.

Gautelier, M., Schott, J. and Oelkers, E.H., 2007. An experimental study of dolomite dissolution rates at 80 C as a function of chemical affinity and solution composition: *Chemical Geology*, v. *242*(3-4), p. 509-517.

Gelman, A. and Hill, J., 2006. *Data analysis using regression and multilevel/hierarchical models*. Cambridge university press.

Goldsmith, J.R. and Heard, H.C., 1961. Subsolidus phase relations in the system CaCO3-MgCO3: *The Journal of Geology*, v. *69*(1), p. 45-74.

Goldsmith, J.R., 1983. Phase relations of rhombohedral carbonates: *Reviews in Mineralogy and Geochemistry*, v. *11*(1), p. 49-76.

Gomez-Rivas, E., Corbella, M., Martín-Martín, J.D., Stafford, S.L., Teixell, A., Bons, P.D., Griera, A. and Cardellach, E., 2014. Reactivity of dolomitizing fluids and Mg source

evaluation of fault-controlled dolomitization at the Benicassim outcrop analogue (Maestrat Basin, E Spain): *Marine and Petroleum Geology*, v. *55*, p. 26-42.

Graf, D.L. and Goldsmith, J.R., 1956. Some hydrothermal syntheses of dolomite and protodolomite: *The Journal of Geology*, v. *64*(2), p. 173-186.

Goldsmith, J.R. and Graf, D.L., 1958. Structural and compositional variations in some natural dolomites. The Journal of Geology, 66(6), pp.678-693.

Gregg, J.M., Howard, S.A. and Mazzullo, S.J., 1992. Early diagenetic recrystallization of Holocene (< 3000 years old) peritidal dolomites, Ambergris Cay, Belize: *Sedimentology*, v. *39*(1), p. 143-160.

Gregg, J.M., Bish, D.L., Kaczmarek, S.E. and Machel, H.G., 2015. Mineralogy, nucleation and growth of dolomite in the laboratory and sedimentary environment: a review: *Sedimentology*, v. *62*(6), p. 1749-1769.

Gresens, R.L., 1981a. The aqueous solubility product of solid solutions: 1. Stoichiometric saturation; partial and total solubility product: *Chemical Geology*, v. *32*(1-4), p. 59-72.

Gresens, R.L., 1981b. The aqueous solubility product of solid solutions: 2. Extension to binary solutions with stoichiometric coefficients greater than unity; analogy with vapor pressure of a binary liquid solution: *Chemical Geology*, v. *32*(1-4), p. 73-86.

Grove, T.L., 1982. Use of exsolution lamellae in lunar clinopyroxenes as cooling rate speedometers: an experimental calibration: *American Mineralogist*, v. *67*(3-4), p. 251-268.

Halla, V.F. and Van Tassel, R., 1965. Auflosungserscheinungen bei erdalkalikarbonaten I. (Dissolution phenomena of alkaline earth aquacarbonates): *Radex-Rundschau*, v. *4*, p. 595-599.

Han, W.S., McPherson, B.J., Lichtner, P.C. and Wang, F.P., 2010. Evaluation of trapping mechanisms in geologic CO2 sequestration: Case study of SACROC northern platform, a 35-year CO2 injection site: *American Journal of Science*, v. *310*(4), p. 282-324.

Harrison, W.E., Luza, K.V., Prater M.L., and Cheung P.K., 1983. Geothermal resource assessment in Oklahoma, Okla: *Geol. Surv. Spec. Publ.*, v. 83 (1), p. 42.

Hefter, G.T. and Tomkins, R.P. eds., 2003. *The experimental determination of solubilities*. John Wiley & Sons.

Helgeson, H.C., Delany, J.M., Nesbitt, H.W., and Bird, D.K., 1978. Summary and critique of the thermodynamic properties of rock-forming minerals: *American Journal of Science*, v. 287-A, p. 1–229.

Hemingway, B.S. and Robie, R.A., 1994. *Enthalpy and Gibbs energy of formation of dolomite, CaMg (CO 3) 2, at 298.15 K from HCl solution calorimetry* (No. 94-575). US Geological Survey.

Hirani, J., Bastesen, E., Boyce, A., Corlett, H., Gawthorpe, R., Hollis, C., John, C.M., Robertson, H., Rotevatn, A. and Whitaker, F., 2018. Controls on the formation of stratabound dolostone bodies, Hammam Faraun Fault block, Gulf of Suez: *Sedimentology*, v. *65*(6), p. 1973-2002.

Hitchon, B. and Brulotte, M., 1994. Culling criteria for "standard" formation water analyses: *Applied Geochemistry*, v. *9*(6), p. 637-645.

Holland, H.D., Kirsipu, T.V., Huebner, J.S. and Oxburgh, U.M., 1964. On some aspects of the chemical evolution of cave waters: *The Journal of Geology*, v. *72*(1), p. 36-67.

Holland, T.J.B. and Powell, R., 1990. An enlarged and updated internally consistent thermodynamic dataset with uncertainties and correlations: the system K2O–Na2O–CaO–MgO–MnO–FeO–Fe2O3–Al2O3–TiO2–SiO2–C–H2–O2: *Journal of metamorphic Geology*, v. *8*(1), p. 89-124.

Holland, T.J.B. and Powell, R., 1998. An internally consistent thermodynamic data set for phases of petrological interest: *Journal of metamorphic Geology*, v. *16*(3), p. 309-343.

Hox, J.J., Moerbeek, M. and Van de Schoot, R., 2017. *Multilevel analysis: Techniques and applications.* Routledge.

Hsu, K.J., 1963. Solubility of dolomite and composition of Florida ground waters: *Journal of Hydrology*, v. *1*(4), p. 288-310.

Huang, Y. and Fairchild, I.J., 2001. Partitioning of Sr2+ and Mg2+ into calcite under karst-analogue experimental conditions: *Geochimica et Cosmochimica Acta*, v. *65*(1), p. 47-62.

Hyeong, K. and Capuano, R.M., 2001. Ca/Mg of brines in Miocene/Oligocene clastic sediments of the Texas Gulf Coast: buffering by calcite/disordered dolomite equilibria: *Geochimica et Cosmochimica Acta*, v. *65*(18), p. 3065-3080.

Inbar, N., Rosenthal, E., Magri, F., Alraggad, M., Möller, P., Flexer, A., Guttman, J. and Siebert, C., 2019. Faulting patterns in the Lower Yarmouk Gorge potentially influence groundwater flow paths: *Hydrology and Earth System Sciences*, v. *23*, p. 763-771.

Johnson, J.W., Oelkers, E.H. and Helgeson, H.C., 1992. SUPCRT92: A software package for calculating the standard molal thermodynamic properties of minerals, gases, aqueous species, and reactions from 1 to 5000 bar and 0 to 1000ºC: *Computers & Geosciences*, v. *18*(7), p. 899-947.

Kaczmarek, S.E. and Sibley, D.F., 2007. A comparison of nanometer-scale growth and dissolution features on natural and synthetic dolomite crystals: implications for the origin of dolomite: *Journal of Sedimentary Research*, v. *77*(5), p. 424-432.

Kaczmarek, S.E. and Sibley, D.F., 2011. On the evolution of dolomite stoichiometry and cation order during high-temperature synthesis experiments: an alternative model for the geochemical evolution of natural dolomites. *Sedimentary Geology*, 240(1-2), pp.30-40.

Kaczmarek, S.E. and Thornton, B.P., 2017. The effect of temperature on stoichiometry, cation ordering, and reaction rate in high-temperature dolomitization experiments. *Chemical Geology*, *468*, pp.32-41.

Karpov, I.K., Kiselev, A.I. and Letnikov, F.A., 1971. Chemical thermodynamics in petrology and geochemistry: *Irkutsk, Akademia Nauka*, p. 385.

Kell-Duivestein, I.J., Baldermann, A., Mavromatis, V. and Dietzel, M., 2019. Controls of temperature, alkalinity and calcium carbonate reactant on the evolution of dolomite and magnesite stoichiometry and dolomite cation ordering degree-An experimental approach. *Chemical Geology*, *529*, p.119292.

Khalaf, F.I., 2007. Occurrences and genesis of calcrete and dolocrete in the Mio-Pleistocene fluviatile sequence in Kuwait, northeast Arabian Peninsula: *Sedimentary Geology*, v. *199*(3-4), p. 129-139.

Khalifa, M.K. and Abed, A.M., 2010. Lithostratigraphy and Microfacies Analysis of the Ajlun Group (Cenomanian to Turonian) in Wadi Sirhan Basin, SE Jordan. *Jordan Journal of Earth and Environmental Sciences*, v. *3*(1), p. 1-16.

Kharaka, Y.K., Maest, A.S., Carothers, W.W., Law, L.M., Lamothe, P.J. and Fries, T.L., 1987. Geochemistry of metal-rich brines from central Mississippi Salt Dome basin, USA: *Applied Geochemistry*, v. *2*(5-6), p. 543-561.

Knacke, O., Kubaschewski, O and Hesselmann, K., 1991. *Thermochemical properties of inorganic substances*. Berlin, New York, Springer-Verlag.

Königsberger, E. and Gamsjäger, H., 1992. Solid-solute phase equilibria in aqueous solution: VII. A re-interpretation of magnesian calcite stabilities: *Geochimica et cosmochimica acta*, v. *56*(11), p. 4095-4098.

Kramer, J.R., 1959. Correction of some earlier data on calcite and dolomite in sea water: *Journal of Sedimentary Research (SEPM)*, v. *29*(3), p. 465-467.

Land, L.S. 1980. The isotopic and trace element geochemistry of dolomite: the state of the art: *Society of Economic Paleontologists and Mineralogists Special Publication*, No. 28, p. 87-110.

Land, L.S. and Prezbindowski, D.R., 1981. The origin and evolution of saline formation water, Lower Cretaceous carbonates, south-central Texas, USA: *Journal of Hydrology*, v. *54*(1-3), p. 51-74.

Land, L.S., 1984. Frio Sandstone Diagenesis, Texas Gulf Coast: A Regional Isotopic Study: Part 1. Concepts and Principles: *AAPG Special Volumes*, p. 47-62.

Land, L.S., 1985. The origin of massive dolomite: *Journal of Geological Education*, v. *33*(2), p. 112-125.

Land, L.S., 1998. Failure to Precipitate Dolomite at 25 °C from Dilute Solution Despite 1000-Fold Oversaturation after 32 Years: *Aquatic Geochemistry*, v. *4*(3-4), p. 361-368.

Langmuir, D., ms, 1965. Stability of carbonates in the system MgO-CO_2- H_2O. PhD thesis. Harvard University.

Langmuir, D., 1971. The geochemistry of some carbonate ground waters in central Pennsylvania. *Geochimica et Cosmochimica Acta*, *35*(10), pp.1023-1045.

Laya J.C., Teoh C.P. , Whitaker F.F., Manche C., Kaczmarek S., Tucker M.E., Gabellone, T., Hasiuk, F., 2021. Dolomitization of a Miocene-Pliocene progradational carbonate platform by mesohaline brine: testing the reflux model on Bonaire Island: *Marine and Petroleum Geology* (in press as of 30th Dec)

Lippmann, F., 1977. The solubility products of complex minerals, mixed crystals, and three-layer clay minerals: *Neues Jahrbuch für Mineralogie Abhandlungen*, v. 130, p. 243-263.

Lippmann, F., 1980. Phase diagrams depicting aqueous solubility of binary mineral systems. *Neues Jahrbuch für Mineralogie Abhandlungen*, v.139 (1), p. 1-25.

Loucks, R.G., Richmann, D.L. and Milliken, K.L., 1980. Factors controlling porosity and permeability in geopressured Frio sandstone reservoirs, General Crude Oil/Department of Energy Pleasant Bayou test wells, Brazoria County, Texas. In *Proceedings of the Fourth Geopressured Geothermal Energy Conference*, v. 1, p. 46-82.

Loucks, R.G., Dodge, M.M. and Galloway, W.E., 1984. Regional controls on diagenesis and reservoir quality in lower Tertiary sandstones along the Texas Gulf Coast: Part 1. Concepts and principles: AAPG Special Volumes, v. 59, p. 14-45.

Lumsden, D.N. and Chimahusky, J.S., 1980. Relationship between dolomite nonstoichiometry and carbonate facies parameters: *Society of Economic Paleontologists and Mineralogists Special Publication*, No. 28, p. 123-137.

Luth, R.W., 2001. Experimental determination of the reaction aragonite+ magnesite= dolomite at 5 to 9 GPa: *Contributions to Mineralogy and Petrology*, v. *141*(2), p. 222-232.

Maier, C.G. and Kelley, K.K., 1932. An equation for the representation of high-temperature heat content data1: *Journal of the American chemical society*, v. *54*(8), p. 3243-3246.

Manche, C.J. and Kaczmarek, S.E., 2019. Evaluating reflux dolomitization using a novel high-resolution record of dolomite stoichiometry: A case study from the Cretaceous of central Texas, USA. *Geology*, *47*(6), pp.586-590

McNaught, A.D., 1997. *Compendium of chemical terminology* (Vol. 1669). Oxford: Blackwell Science.

Miron, G.D., Wagner, T., Kulik, D.A. and Lothenbach, B., 2017. An internally consistent thermodynamic dataset for aqueous species in the system Ca-Mg-Na-K-Al-Si-OHC-Cl to 800 °C and 5 kbar: *American Journal of Science*, v. *317*(7), p. 755-806.

Miser, D.E., Swinnea, J.S. and Steinfink, H., 1987. TEM observations and X-ray crystal-structure refinement of a twinned dolomite with a modulated microstructure: *American Mineralogist*, v. *72*(1-2), p. 188-193.

Möller, P., 1973. Determination of the composition of surface layers of calcite in solutions containing Mg2+: *Journal of Inorganic and Nuclear Chemistry*, v. *35*(2), p. 395-401.

Möller, P. and Sastri, C.S., 1974. Estimation of the number of surface layers of calcite involved in Ca-45Ca isotopic exchange with solution: *Zeitschrift für Physikalische Chemie*, v. *89*(1-4), p. 80-87.

Möller, P. and De Lucia, M., 2020. The impact of Mg2+ ions on equilibration of Mg-Ca carbonates in groundwater and brines: *Geochemistry*, v. 80(2), p.125611.

Morton, R.A. and Land, L.S., 1987. Regional variations in formation water chemistry, Frio Fm. (Oligocene), Texas Gulf Coast: *AAPG bulletin*, v. *71*(2), p.191-206.

Nakagawa, S., Johnson, P.C. and Schielzeth, H., 2017. The coefficient of determination R 2 and intra-class correlation coefficient from generalized linear mixed-effects models revisited and expanded: *Journal of the Royal Society Interface*, v. *14*(134), p. 20170213.

Naumov, G.B., Ryzhenko, B.N. and Khodakovsky, I.L., 1974. Handbook of thermodynamic data. *Transl. into ENGLISH of the publ." Handbook of Thermodyanic Data" Moscow, Atomizdat., 1971*.

Navrotsky, A. and Loucks, D., 1977. Calculation of subsolidus phase relations in carbonates and pyroxenes: *Physics and Chemistry of Minerals*, v. *1*(1), p. 109-127.

Navrotsky, A. and Capobianco, C., 1987. Enthalpies of formation of dolomite and of magnesian calcites: *American Mineralogist*, v. *72*(7-8), p. 782-787.

Navrotsky, A., Dooley, D., Reeder, R. and Brady, P., 1999. Calorimetric studies of the energetics of order-disorder in the system $Mg_{1-x} Fe_x Ca (CO_3)_2$: *American Mineralogist*, v. *84*(10), p.1622-1626.

Nordeng, S.H. and Sibley, D.F., 1994. Dolomite stoichiometry and Ostwald's step rule: *Geochimica et Cosmochimica Acta*, v. *58*(1), p. 191-196.

Parkhurst, D.L. and Appelo, C.A.J., 1999. User's guide to PHREEQC (Version 2): A computer program for speciation, batch-reaction, one-dimensional transport, and inverse geochemical calculations: *Water-resources investigations report*, v. *99*(4259), p. 312.

Pina, C.M., Pimentel, C. and Crespo, Á., 2020. Dolomite cation order in the geological record: *Chemical Geology*, v. 547, p.119667.

Plummer, L.N. and Mackenzie, F.T., 1974. Predicting mineral solubility from rate data; application to the dissolution of magnesian calcites: *American Journal of Science*, v. *274*(1), p. 61-83.

Plummer, L.N. and Busenberg, E., 1982. The solubilities of calcite, aragonite and vaterite in CO_2-H_2O solutions between 0 and 90°C, and an evaluation of the aqueous model for the system $CaCO_3$-CO_2-H_2O: *Geochimica et cosmochimica acta*, v. *46*(6), p. 1011-1040.

Plummer, L.N., Parkhurst, D.L., Fleming, G.W. and Dunkle, S., 1988. PHRQPITZ, a computer program incorporating Pitzer's equations for calculation of geochemical reactions in brines. *US Geological Survey Water Resources Investigation Report*, *88*, p.4153.

Pokrovsky, O.S. and Schott, J., 2001. Kinetics and mechanism of dolomite dissolution in neutral to alkaline solutions revisited: *American Journal of Science*, v. *301*(7), p. 597-626.

Pokrovsky, O.S., Golubev, S.V., Schott, J. and Castillo, A., 2009. Calcite, dolomite and magnesite dissolution kinetics in aqueous solutions at acid to circumneutral pH, 25 to 150 °C and 1 to 55 atm pCO_2: New constraints on CO_2 sequestration in sedimentary basins: *Chemical geology*, v. *265*(1-2), p. 20-32.

Prédali, J.J. and Cases, J.M., 1973. Zeta potential of magnesian carbonates in inorganic electrolytes: *Journal of Colloid and Interface Science*, v. *45*(3), p. 449-458.

Radke, B.M. and Mathis, R.L., 1980. On the formation and occurrence of saddle dolomite: *Journal of Sedimentary Research*, v. *50*(4), p. 1149-1168.

Ray, S., ms, 2016. National evaluation for development and exploration potential of mineral commodities in produced waters. PhD thesis. The University of Texas at El Paso.

Reeder, R.J. and Wenk, H.R., 1983. Structure refinements of some thermally disordered dolomites: *American Mineralogist*, v. *68*(7-8), p. 769-776.

Reeder, R.J., 1992. Carbonates; growth and alteration microstructures: *Reviews in Mineralogy and Geochemistry*, v. *27*(1), p. 380-424.

Reeder, R.J., 2000. Constraints on cation order in calcium-rich sedimentary dolomite: *Aquatic Geochemistry*, v. *6*(2), p. 213-226.

Robie, R.A., Hemingway, B.S. and Fisher, J.R., 1978. *Thermodynamic properties of minerals and related substances at 298. 15 k and 1 bar (10/sup 5/pascals) pressure and at higher temperatures* (No. USGS-BULL-1452). Technical Report, Geological Survey, Washington, DC (USA).

Robie, R.A. and Hemingway, B.S., 1995. *Thermodynamic properties of minerals and related substances at 298.15 K and 1 bar (105 Pascals) pressure and at higher temperatures.* (Vol. 2131). US Government Printing Office.

Rock, P.A., Mandell, G.K., Casey, W.H. and Walling, E.M., 2001. Gibbs energy of formation of dolomite from electrochemical cell measurements and theoretical calculations: *American Journal of Science*, v. *301*(2), p. 103-111.

Rodriguez-Blanco, J.D., Shaw, S. and Benning, L.G., 2015. A route for the direct crystallization of dolomite: *American Mineralogist*, v. *100*(5-6), p. 1172-1181.

Rosenberg, P.E. and Holland, H.D., 1964. Calcite-dolomite-magnesite stability relations in solutions at elevated temperatures: *Science*, v. *145*(3633), p. 700-701.

Shen, Z., Konishi, H., Brown, P.E. and Xu, H., 2013. STEM investigation of exsolution lamellae and "c" reflections in Ca-rich dolomite from the Platteville Formation, western Wisconsin: *American Mineralogist*, v. *98*(4), p.760-766.

Sherman, L.A. and Barak, P., 2000. Solubility and dissolution kinetics of dolomite in Ca–Mg–HCO$_3$/CO$_3$ solutions at 25°C and 0.1 MPa carbon dioxide: *Soil Science Society of America Journal*, v. *64*(6), p. 1959-1968.

Shock, E.L. and Helgeson, H.C., 1988. Calculation of the thermodynamic and transport properties of aqueous species at high pressures and temperatures: Correlation algorithms for ionic species and equation of state predictions to 5 kb and 1000°C: *Geochimica et Cosmochimica Acta*, v. *52*(8), p. 2009-2036.

Shock, E.L., Sassani, D.C., Willis, M. and Sverjensky, D.A., 1997. Inorganic species in geologic fluids: correlations among standard molal thermodynamic properties of aqueous ions and hydroxide complexes: *Geochimica et Cosmochimica Acta*, v. *61*(5), p. 907-950.

Shope, E.N., Reber, T.J., Stutz, G.R., Aguirre, G.A., Jordan, T.E. and Tester, J.W., 2012, February. Geothermal resource assessment: A detailed approach to low-grade resources in the states of New York and Pennsylvania. In *Proceedings, Thirty-Seventh Workshop on Geothermal Reservoir Engineering* (p. 885-893). Stanford, California: Stanford University.

Siebert, C., Möller, P., Geyer, S., Kraushaar, S., Dulski, P., Guttman, J., Subah, A. and Rödiger, T., 2014. Thermal waters in the Lower Yarmouk Gorge and their relation to surrounding aquifers: *Geochemistry*, v. *74*(3), p. 425-441.

Siebert and others (*in prep*): From Möller and De Lucia (2020)

Sinclair, D.J., 2011. Two mathematical models of Mg and Sr partitioning into solution during incongruent calcite dissolution: implications for dripwater and speleothem studies: *Chemical Geology*, v. *283*(3-4), p. 119-133.

Sinclair, D.J., Banner, J.L., Taylor, F.W., Partin, J., Jenson, J., Mylroie, J., Goddard, E., Quinn, T., Jocson, J. and Miklavič, B., 2012. Magnesium and strontium systematics in tropical speleothems from the Western Pacific: *Chemical Geology*, v. *294*, p. 1-17.

Sperber, C.M., Wilkinson, B.H. and Peacor, D.R., 1984. Rock composition, dolomite stoichiometry, and rock/water reactions in dolomitic carbonate rocks: *The Journal of Geology*, v. *92*(6), p. 609-622.

Spötl, C. and Pitman, J.K., 1998. Saddle (baroque) dolomite in carbonates and sandstones: a reappraisal of a burial-diagenetic concept: *Carbonate Cementation in Sandstones: Distribution Patterns and Geochemical Evolution*, v. *26*, p. 437-460.

Stoessell, R.K., Klimentidis, R.E. and Prezbindowski, D.R., 1987. Dedolomitization in Na-Ca-Cl brines from 100° to 200° C at 300 bars: *Geochimica et Cosmochimica Acta*, v. *51*(4), p. 847-855.

Stout, J.W. and Robie, R.A., 1963. Heat capacity from 11 to 300 K., entropy, and heat of formation of dolomite: *The Journal of Physical Chemistry*, v. *67*(11), p. 2248-2252.

Strand, S., Høgnesen, E.J. and Austad, T., 2006. Wettability alteration of carbonates—Effects of potential determining ions (Ca^{2+} and SO_4^{2-}) and temperature: *Colloids and Surfaces A: Physicochemical and Engineering Aspects*, v. *275*(1-3), p. 1-10.

Team, R.C., 2000. R language definition. *Vienna, Austria: R foundation for statistical computing*.

Tesmer, M., Moeller, P., Wieland, S., Jahnke, C., Voigt, H. and Pekdeger, A., 2007. Deep reaching fluid flow in the North East German Basin: origin and processes of groundwater salinization: *Hydrogeology Journal*, v. *15*(7), p. 1291-1306.

Thieling, S.C. and Moody, J.S., 1997. Atlas of shallow Mississippi salt domes.

Thorstenson, D.C. and Plummer, L.N., 1977. Equilibrium criteria for two-component solids reacting with fixed composition in an aqueous phase; example, the magnesian calcites: *American Journal of Science*, v. *277*(9), p. 1203-1223.

Ulfsbo, A., Abbas, Z. and Turner, D.R., 2015. Activity coefficients of a simplified seawater electrolyte at varying salinity (5–40) and temperature (0 and 25° C) using Monte Carlo simulations: *Marine Chemistry*, v. *171*, p. 78-86.

Usdowski, H.E., 1967. *Die Genese von Dolomit in Sedimenten* (Vol. 4). Springer.

Usdowski, E., 1989. Synthesis of dolomite and magnesite at 60 °C in the system Ca^{2+}-Mg^{2+}-Co_3^{2-}-Cl_2^{2-}-H_2O: Naturwissenschaften (NW), v. *76*(8), p. 374-375.

Usdowski, E., 1994. Synthesis of dolomite and geochemical implications. In *Dolomites: A Volume in Honour of Dolomieu* (Vol. 21, pp. 345-360). Oxford UK, Blackwell Scientific Publications.

Van Tendeloo, G., Wenk, H.R. and Gronsky, R., 1985. Modulated structures in calcian dolomite: A study by electron microscopy: *Physics and Chemistry of Minerals*, v. *12*(6), p. 333-341.

Vespasiano, G., Apollaro, C., Muto, F., Dotsika, E., De Rosa, R. and Marini, L., 2014. Chemical and isotopic characteristics of the warm and cold waters of the Luigiane Spa near Guardia Piemontese (Calabria, Italy) in a complex faulted geological framework: *Applied Geochemistry*, v. *41*, p. 73-88.

Wagman, D.D., Evans, W.H., Parker, V.B., Schumm, R.H. and Halow, I., 1982. *The NBS tables of chemical thermodynamic properties. Selected values for inorganic and C1 and C2 organic substances in SI units*. National Standard Reference Data System.

Warren, J., 2000. Dolomite: occurrence, evolution and economically important associations: *Earth-Science Reviews*, v. *52*(1-3), p. 1-81.

Westfall, P.H., 2014. Kurtosis as peakedness, 1905–2014. RIP. *The American Statistician*, *68*(3), pp.191-195.

Whitaker, F.F. and Xiao, Y., 2010. Reactive transport modeling of early burial dolomitization of carbonate platforms by geothermal convection: *AAPG bulletin*, *94*(6), pp.889-917.

Wolery, T.J., Jackson, K.J., Bourcier, W.L., Bruton, C.J., Viani, B.E., Knauss, K.G. and Delany, J.M., 1990. Current status of the EQ3/6 software package for geochemical modelling: ACS Symposium Series, v. 416 (Chapter 8), p. 104-116.

Wright, K., Cygan, R.T. and Slater, B., 2002. Impurities and nonstoichiometry in the bulk and on the (1014) surface of dolomite: *Geochimica et cosmochimica acta*, v. *66*(14), p. 2541-2546.

Xu, T., 2008. *TOUGHREACT testing in high ionic strength brine sandstone systems* (No. LBNL--1051E). Ernest Orlando Lawrence Berkeley National Laboratory.

Yanat'eva, O.K., 1952. Solubility of dolomite in water salt solutions: *Izvestiya Sektora FkhA Akademii Nauk SSSR*, v. *20*, p. 252-268.

Zhang, S., Yang, L., DePaolo, D.J. and Steefel, C.I., 2015. Chemical affinity and pH effects on chlorite dissolution kinetics under geological CO2 sequestration related conditions. *Chemical Geology*, *396*, pp.208-217.

Figure captions

Fig. 1 A) Calcite can be described by both the hexagonal unit cell (17.06Å in height) and the rhombohedral unit cell (superimposed in black lines). Perpendicular to the c-axis are alternating planes of Ca^{2+} cations and CO_3^{2-} groups. B) Dolomite hexagonal unit cell (16.01Å in height) with rhombohedral unit cell superimposed. Cation ordering results in the alternating layers of Ca^{2+} and Mg^{2+} cations. Reproduced with permission from Gregg and others (2015).

Fig.2 Temperature dependence of the theoretical ordering parameter of dolomite (s) as defined in equation (12). There are four solutions (Chaikin et al., 1995); (1) $s = 0$ at and above the critical temperature (T_c) which is here 1473K, equating to a synthetic, ideal dolomite (Goldsmith and Heard, 1961) (2) $s = \pm\sqrt{\frac{3(T_c-T)}{T}}$ for the asymptotic approach to T_c. (3) $s = 1$ at T = 0K, (4) $s = \tanh\left(\frac{T_c}{T}\right)$ for the asymptotic approach to T = 0K. For the Bragg-Williams model well-ordered dolomite ($s \geq 0.96$) is the most stable state at conditions $\leq$ 500°C. Dashed line for Helgeson and others (1978) represents their estimation of naturally ordered ($s = 0.7$) dolomite. Gregg and others (1992) determine $0.7 < s < 0.9$ for Holocene dolomites. Dashed line for Hyeong and Capuano (2001) represents their estimate for a partially ordered ($s = 0.4$) dolomite. Modified from Helgeson and others (1978).

Fig. 3 Relative frequencies of dolomite stoichiometry for; a) Pliocene Bonaire dolomite (n=72; samples with >90% dolomite) (Laya and others, 2021) b) Phanerozoic dolomites from North America (n=55) (Sperber and others, 1984). c) Global dolomites based on samples (n=654) from a wide variety of localities and ages compiled by Sperber and others, (1984); Triassic of northwestern Germany (n=48), Phanerozoic of North America (n=345), Tertiary of Libya (n=139), Upper Jurassic of Germany (n=76), Upper Permian of Germany (n=43), Upper Devonian of Belgium (n=3).

Fig. 4 a) Total concentrations of Ca^{2+} and Mg^{2+} in the bulk solution as a function of the square root of time during the dissolution of HMC algal calcite (Plummer and Mackenzie, 1974). $[Ca^{2+}]$ and $[Mg^{2+}]$ are non-linear in stage one suggesting congruent dissolution. In stage two both are linear suggesting release to bulk solution is controlled by diffusion through a product layer. In stage three $[Mg^{2+}]$ is linear but obeys a parabolic rate law and the non-linear decrease in $[Ca^{2+}]$ indicates a transition towards formation of a more Mg-rich incongruent phase from a more Ca-rich (~ pure calcite) incongruent phase precipitating during stage two. b) The re-evaluation by Thorstenson and Plummer (1977) of data from Plummer and Mackenzie (1974) was notably critiqued by Gresens (1981a) for producing too great a range in equilibrium $\log_{10}(^aCa^{2+}/^aMg^{2+})$ values (note this data is plotted on a separate y-axis). The inclusion of this data by Möller and De Lucia (2020) led to their erroneous interpretation that the Bénézeth and others (2018) data is comparable to that of Möller (1973), though this is clearly an artifact of being plotted on the same scale as the Thorstenson and Plummer (1977) data. The difference between the studies for a similar composition (~50%) is ~0.5-1.0 log units which is substantial. Redrawn from Möller and De Lucia (2020).

Fig. 5 a) Effects of ideal mixing on solubilities and equilibrium $\log_{10}(^aCa^{2+}/^aMg^{2+})$ for solutions buffered by $LMC_{(4\%MgCO_3)}$ and calcian dolomite$_{(2\%CaCO_3)/(4\%CaCO_3)}$ (and SUPCRT92 calcite and J23 dolomite). This study's reference model (J21) of

$\log_{10}(^{a}Ca^{2+}/^{a}Mg^{2+})$ values between the SUPCRT92-Filter is solid purple with the model (K1) of values not subject to the SUPCRT92-Filter (n=11,480) in dashed green. The model (J24) utilizing a fixed β_1 coefficient of -0.06919 is in dashdot purple. b) Blue lines and symbols represent K_{sp-dol} estimations and $\log_{10}(^{a}Ca^{2+}/^{a}Mg^{2+})$ observations from groundwater studies. Lime green markers denote a determination of $\mathbf{K_{sp-dol}}$ only though dolomite precipitation (we include the Moller (1973) surface experiments in this category). Red markers represent approaches from dolomite dissolution. Dark green lines and symbols represent approaches from both dolomite precipitation and dissolution. Black symbols are derived through thermal decomposition of dolomite or components or minimizing free energies of components through a database type approach (see supplementary table 2).

Fig. 6 a) This study's geothermal gradient interpolation (0.1x0.1° Lat/Long resolution) using the SMUH dataset (Blackwell and others, 2011). b) Number of SMUH samples per US county (for counties with ≥1 sample). Large counties in historically prolific oil producing states have the highest number of temperature measurements, with a maximum n=3,739 for Crockett county, south Texas. c) The SMUH interpolation (Blackwell and others, 2011) for heat flow which is based on the same data used for this study's interpolation of geothermal gradients, which are most similar in areas with a high spatial resolution of temperature measurements. d) Number of filtered PWGD samples (n=11,480) per US county (for counties with ≥1 sample). Large counties in historically prolific oil producing states have the highest number of temperature measurements, with a maximum n=519 for Fremont county, Wyoming. e) Mean annual land surface temperature (MAST) (°C) for North America between 2003-2014 (Bechtel, 2015) interpolated at 0.1x0.1° Lat/Lon resolution. All maps, aside from c, are WGS 84.

Fig. 7 a) Map showing Test Areas A and B (black boxes) in the south-eastern USA, and the locations of Frio formation samples (crosses). b) Location of fields in Test Area A (W94°48'-W96°00'/N28°48'-N29°30'). c) Location of fields in Test Area B (W88°12'-W90°00'/N31°30'-N32°12'). Open triangles are fields contained in the PWGD. Filled triangles in are fields for which data has previously been published (Kharaka and others, 1987; Hyeong and Capuano, 2001). The unfilled squares in c) (Soso and Raleigh fields) represent fields included in both the literature and PWGD datasets. Some fields located outside of the bounding boxes are included in the analysis after sample locations are rounded to the nearest 0.1° Lat/Long. Circles in b) and c) mark salt dome locations from Beckman and Williamson (1990) and Thieling and Moody (1997). Colours for b) and c) show this study's geothermal gradients (fig. 5b).

Fig. 8 a) Comparison of temperatures measured at formation depth observed by Hyeong and Capuano, (2001) and those predicted for PWGD samples in Test Area A by this study's methodology. A geothermal gradient representing the average geothermal gradient (SMUH data – mean 33°C/km; range 29-35°C/km shaded grey) and the average surface temperature (MAST data - mean 16°C; range 15-16°C;) calculated for the PWGD samples in Test Area A shows a reasonable fit to the measured temperatures. Samples from the shallower (651-921m) Miocene sediments have measured temperatures significantly above the upper range of geothermal gradients calculated for Test Area A, emphasizing the limitation of assuming linear geothermal gradients. b) Comparison of temperatures at

formation depth measured by Kharaka and others, (1987) and those predicted for PWGD samples in Test Area B. A geothermal gradient representing the average geothermal gradient (SMUH data – mean 27°C/km; range 22-34°C/km shaded grey) and the average surface temperature (MAST data - mean 13°C; range 12-14°C;) calculated for the PWGD samples in Test Area B shows a reasonable fit to the measured temperatures.

Fig. 9 All plots include this studies' reference mixed model (model J21) (95% confidence intervals shaded light grey), this studies mixed model of the Hyeong and Capuano (2001) dataset (model A4) (95% confidence intervals shaded dark grey) and the SUPCRT92 ordered dolomite-calcite & disordered dolomite-calcite phases. Literature datasets; L & P (1981) – Land and Prezbindowski (1981), K (1987) – Kharaka and others (1987), H & C (2001) – Hyeong and Capuano (2001), M & D (2020) – Moller and DeLucia (2020) a) The Hyeong and Capuano (2001) linear model (A1) is near identical to the linear model (A2; confidence intervals shaded blue) of the Hyeong and Capuano (2001) dataset recalculated by this study using PHREEQC. The three-term Maier-Kelly regression (model A3) produces a spurious fit outside the experimental range. The A4 mixed model calculates a unique intercept $\log_{10}(^aCa^{2+}/^aMg^{2+})$ for each group whilst the gradient for the increase in $\log_{10}(^aCa^{2+}/^aMg^{2+})$ with temperature is constant for all groups (random intercept model); for the A5 mixed model the group gradient can also vary (random slope model). b) There are relatively significant changes from the linear models of the Chocolate/Halls Bayou (B1) and West Columbia (model C1) fields to the A4 mixed model group-level results for these fields. c) For the small Miocene Fm. dataset (n=6) the transition from the linear model (model E1) to the mixed model (A4) group results is pronounced. The Frio Fm. (n=45; Hyeong and Capuano (2001) dataset) linear model (D1) is relatively similar to the mixed model (A4) group result. d) The mixed model (F1) of PWGD samples contained within Test Area A (n=21) shows a similar profile to the mixed model (A4) of the Hyeong and Capuano (2001) dataset, with typically low $\log_{10}(^aCa^{2+}/^aMg^{2+})$ values, whilst Frio Fm. samples elsewhere (model G1) are clearly very different. This comparability at a local scale suggests that the PWGD dataset is reliable. e) Samples from Kharaka and others, (1987) (n=16) (model H1), including the Reedy (n=5) and Soso (n=4) samples, and in general samples from Test Area B (n=204) (model I1) have higher $\log_{10}(^aCa^{2+}/^aMg^{2+})$ values than those present in Test Area A (F1) being closer to the model average of the reference model (J21). f) Yarmouk gorge dataset from Möller and De Lucia (2020) (from Siebert and others (2014) and Siebert and others (in prep)) with models including all samples (model L1; n=42) and excluding samples with temperatures <25°C (M1; n=36). Also shown with dotted box is area represented in figs a, b and c.

Fig. 10 a) 2D Histogram for all (n=11,480) PWGD samples with bin dimensions 10°C x 0.05 $\log_{10}(^aCa^{2+}/^aMg^{2+})$ b) Modal, c) mean, d) kurtosis and e) skewness values for each lithology based on 10°C bin. Modal and mean values for temperatures >120°C are not shown as these samples represent <2.6% of the PWGD data (n=302) and, like kurtosis and skewness values for temperature range (see text), this data is relatively uninformative as there is a high degree of scatter. Kurtosis and skewness values for whole populations are recorded in the legends. f) Standard deviation. g) Cumulative sum of samples. h) Limestone frequency distribution for 60-70°C showing unimodal positive skew. i) Sandstone frequency distribution for 80-90°C showing possible bimodal distribution.

Fig. 11 Comparison of calcite-dolomite (model J23) equilibrium $a\text{Ca}^{2+}$, $a\text{Mg}^{2+}$ and $\log_{10}(^a\text{Ca}^{2+}/^a\text{Mg}^{2+})$ calculated using Pitzer with background electrolytes (NaCl and Na_2SO_4) and common ions (CaSO_4) of varying compositions and concentrations at 25 °C. Equilibrium is approached from conditions of undersaturation of dolomite, calcite and anhydrite (CaSO_4) in the case of the common ion equilibrium. For an equivalent ionic strength, a divalent background electrolyte (Na_2SO_4) in comparison to a monovalent background electrolyte (NaCl) generates a greater amount of dissolution of both calcite and dolomite and lower overall $a\text{Ca}^{2+}$ and $a\text{Mg}^{2+}$ activities due to the greater overall strength of ion-ion interactions. However, whilst activities change and $a\text{Ca}^{2+}$ is always higher than $a\text{Mg}^{2+}$, the difference between them ($\log_{10}(^a\text{Ca}^{2+}/^a\text{Mg}^{2+})$) remains constant.
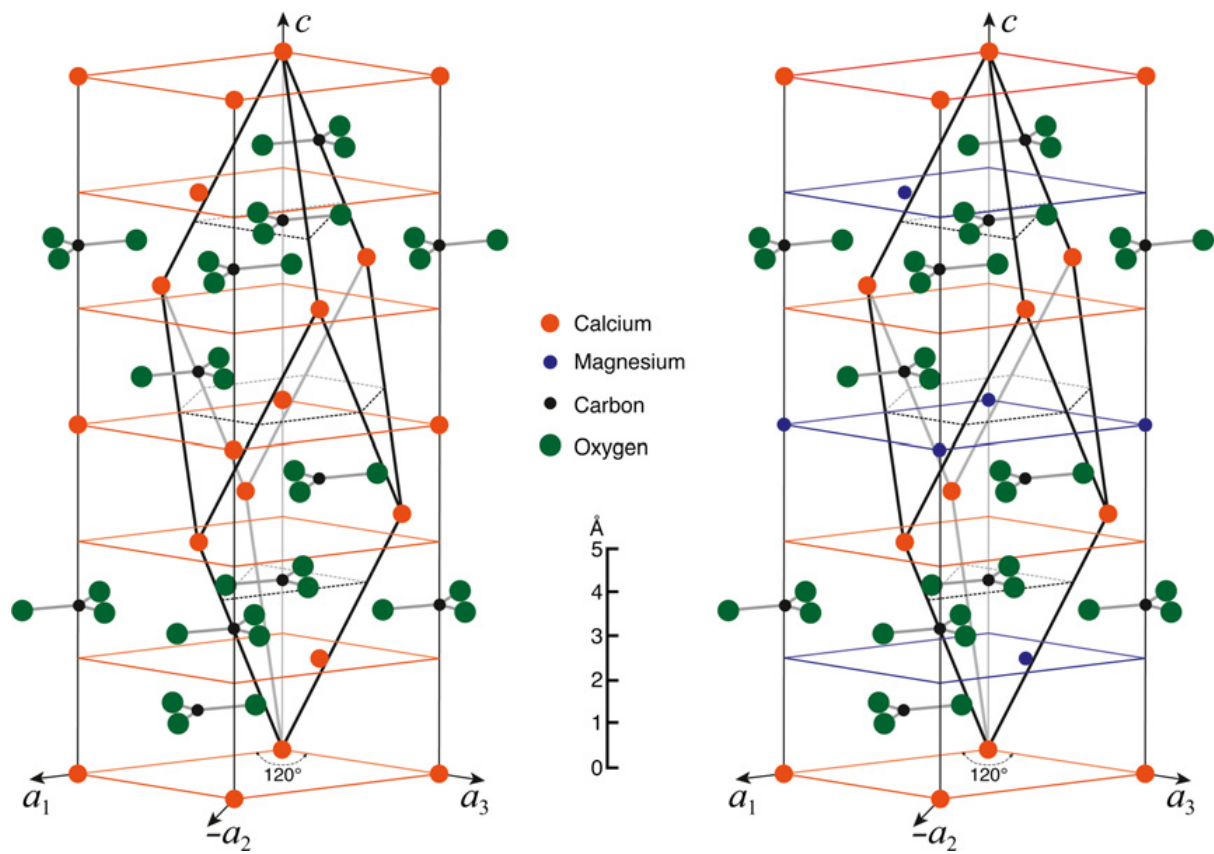
Fig.1
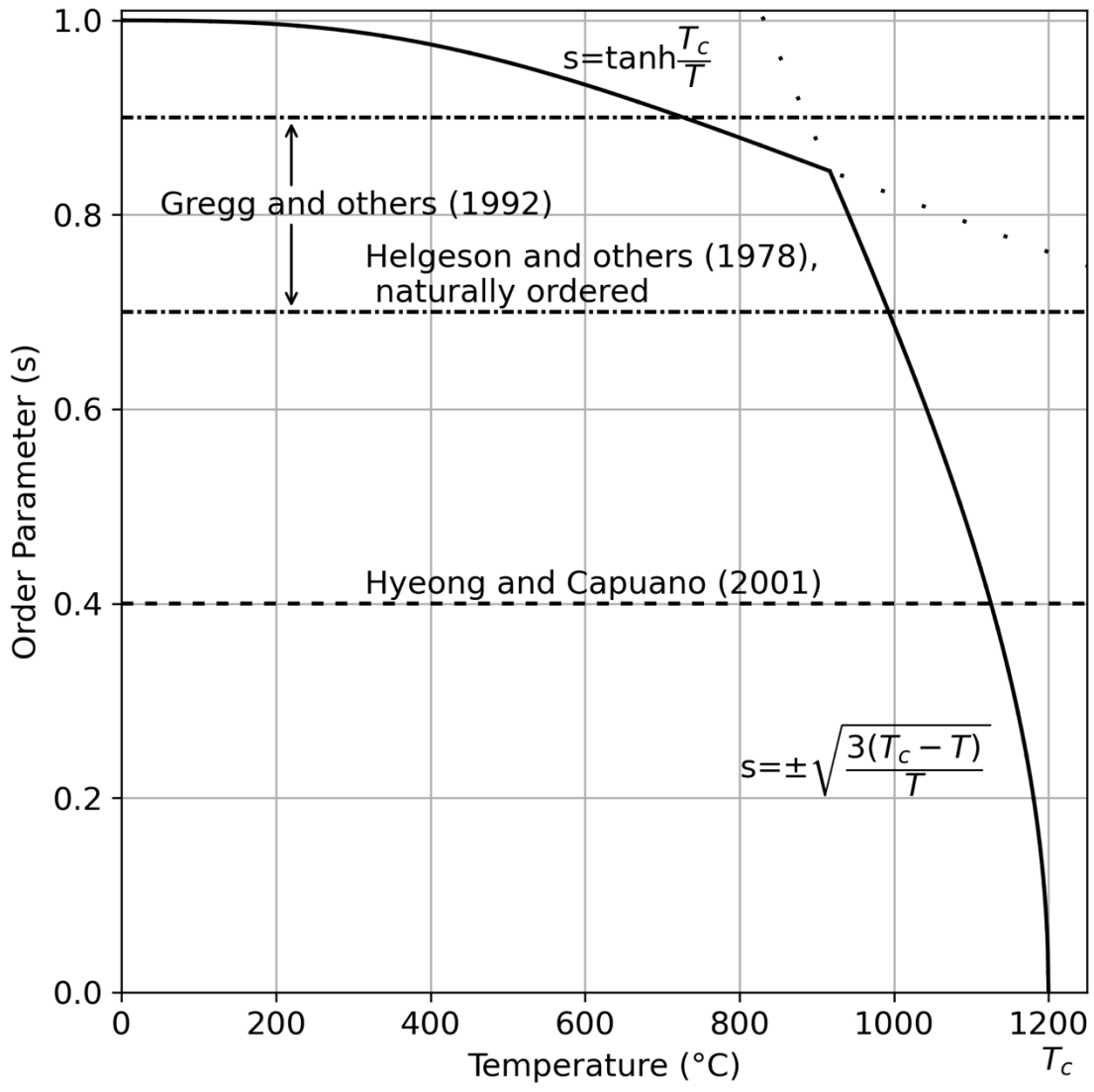
Fig.2
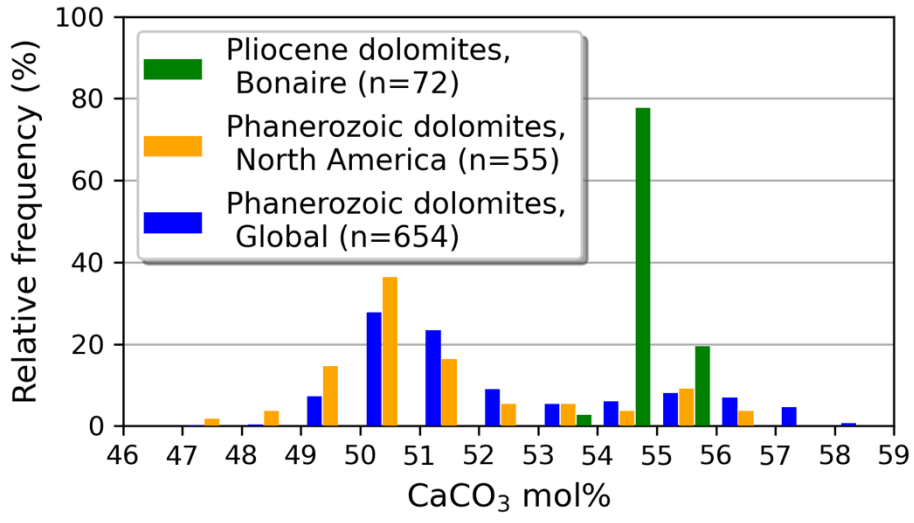
Fig.3

Fig.4

Fig.5

Fig.6

Fig.7
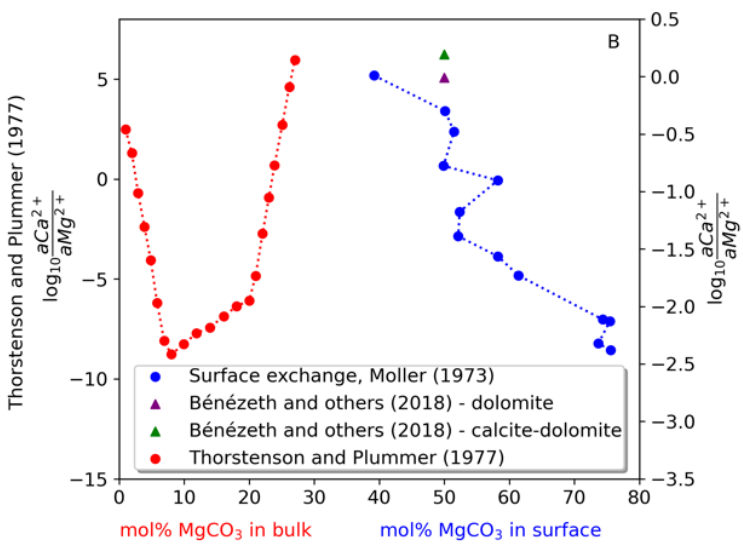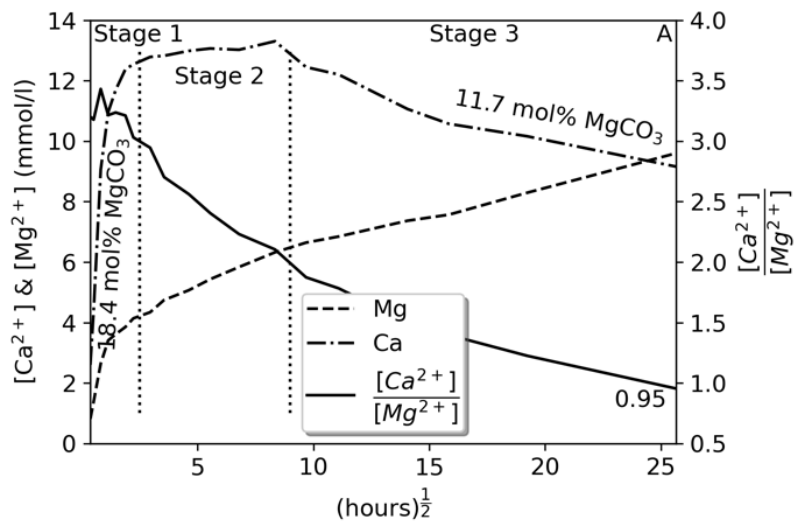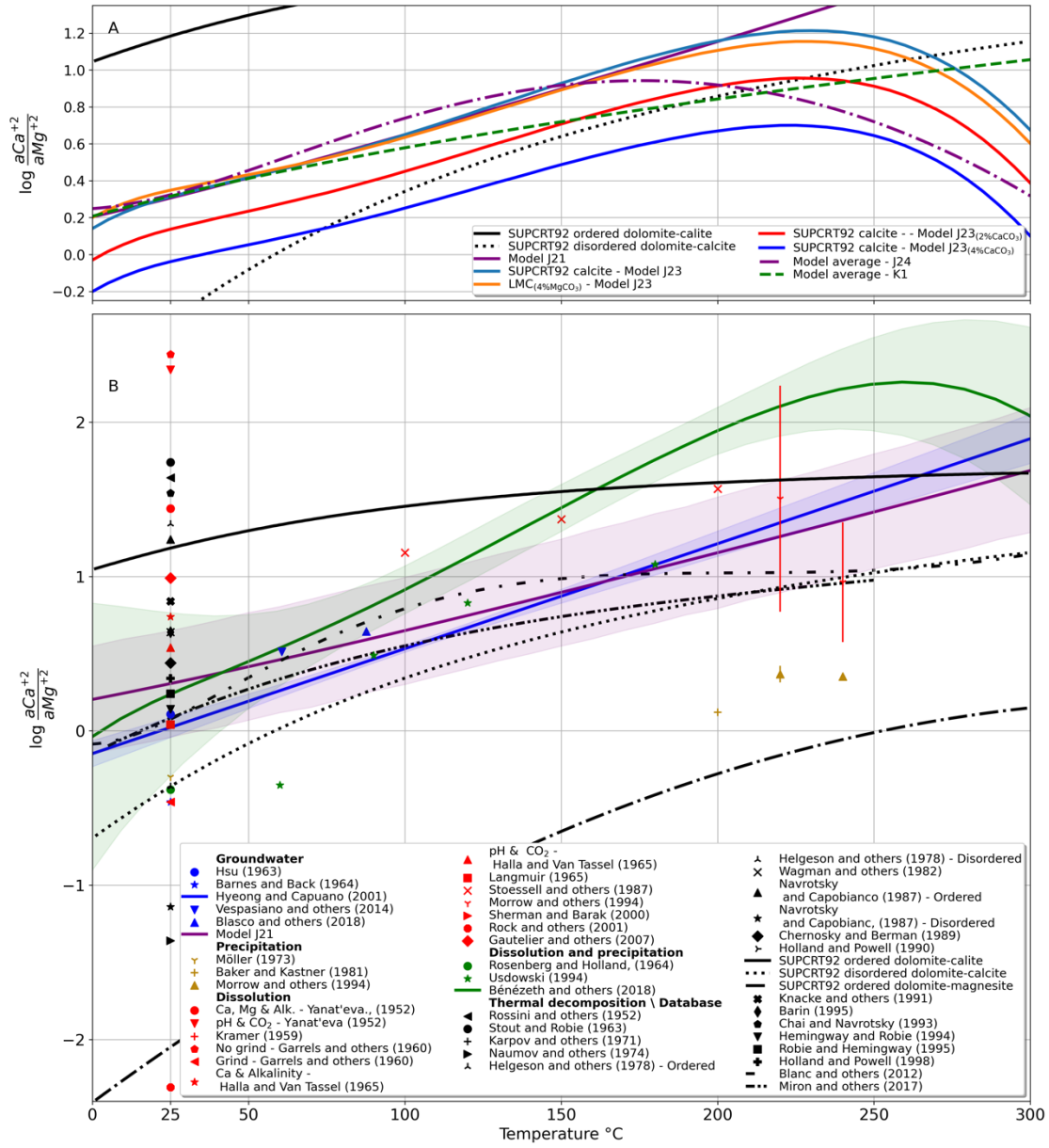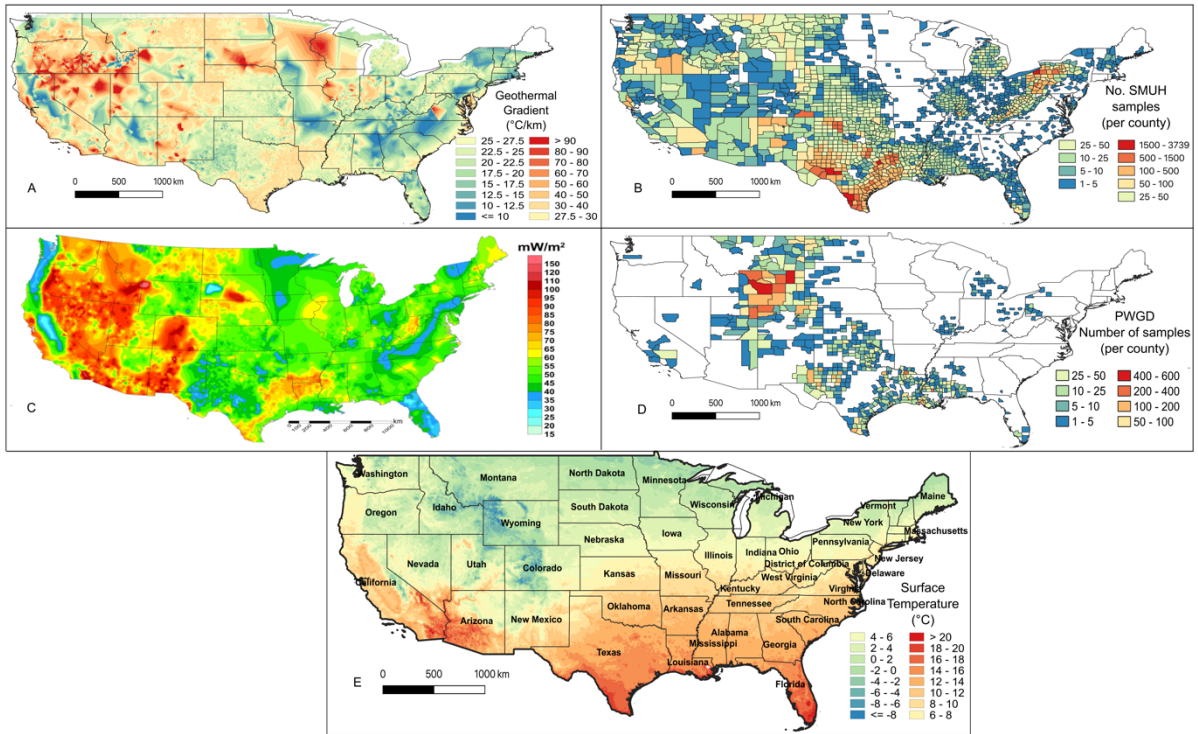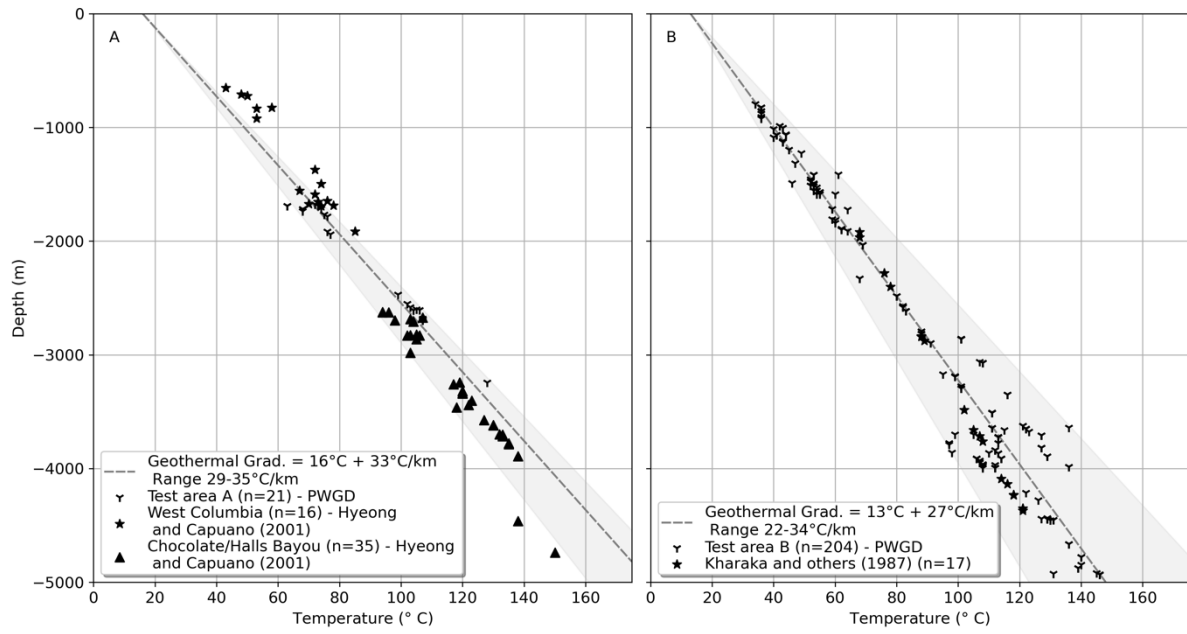
Fig.8
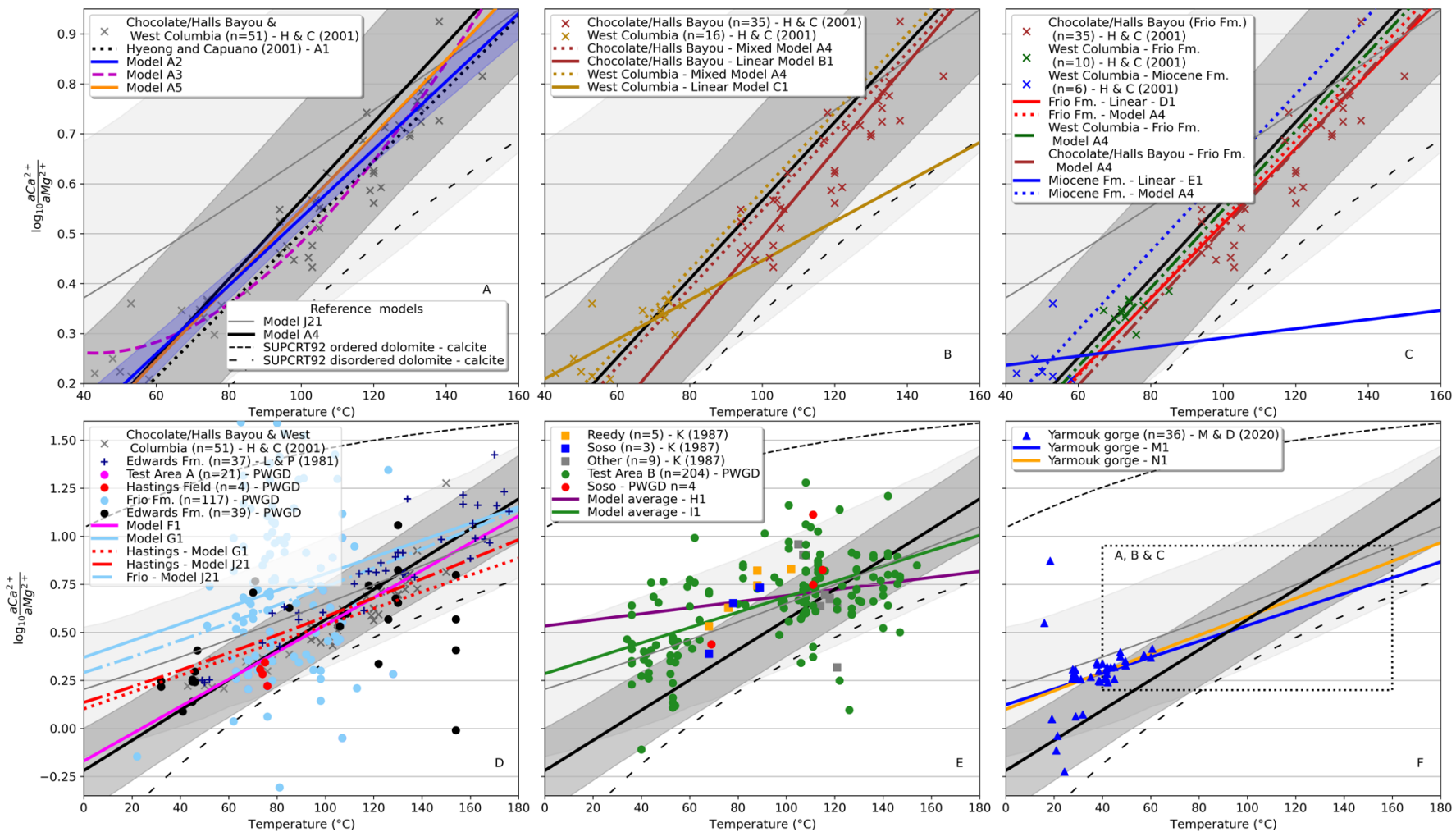
Fig.9
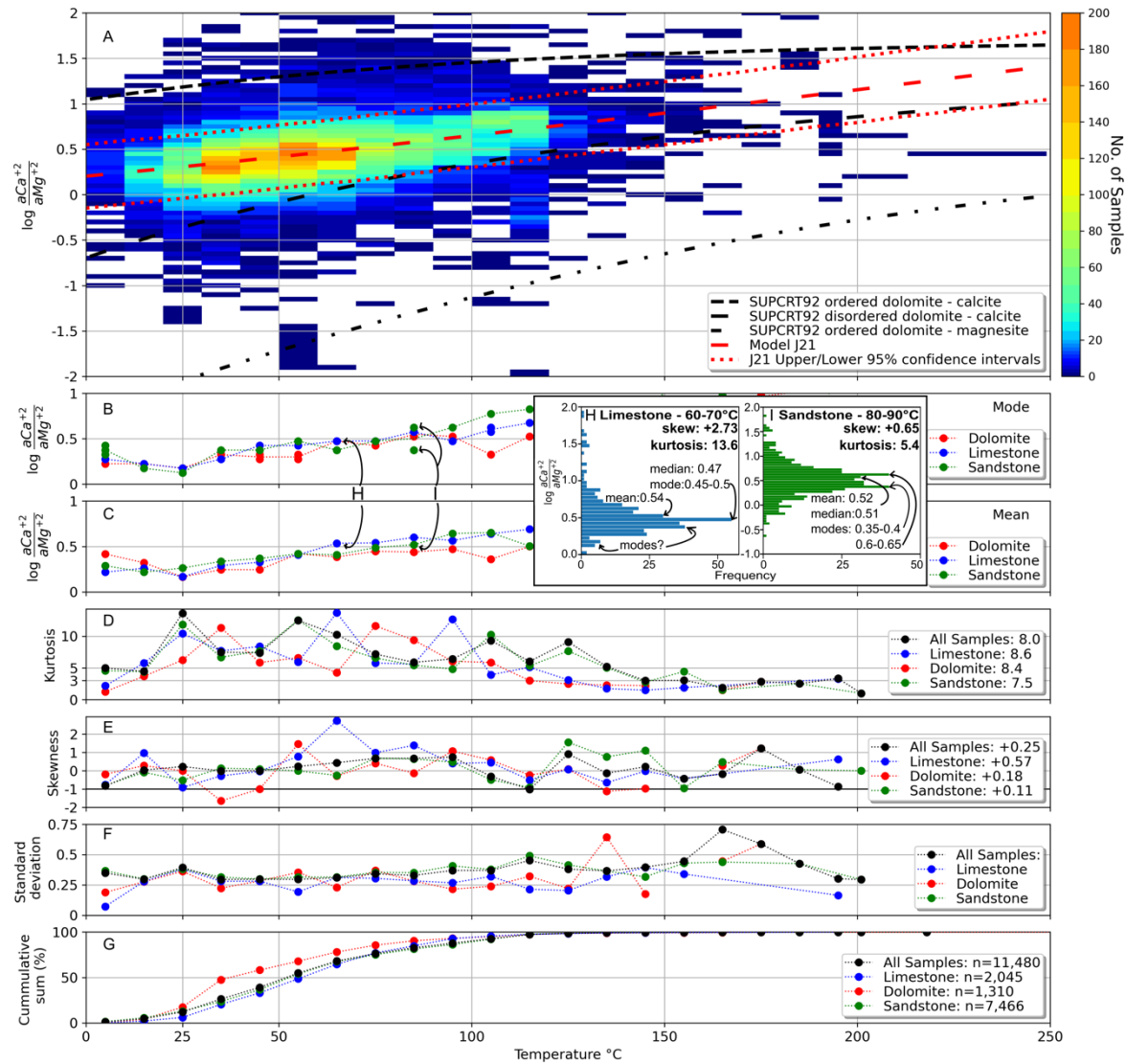
Fig.10
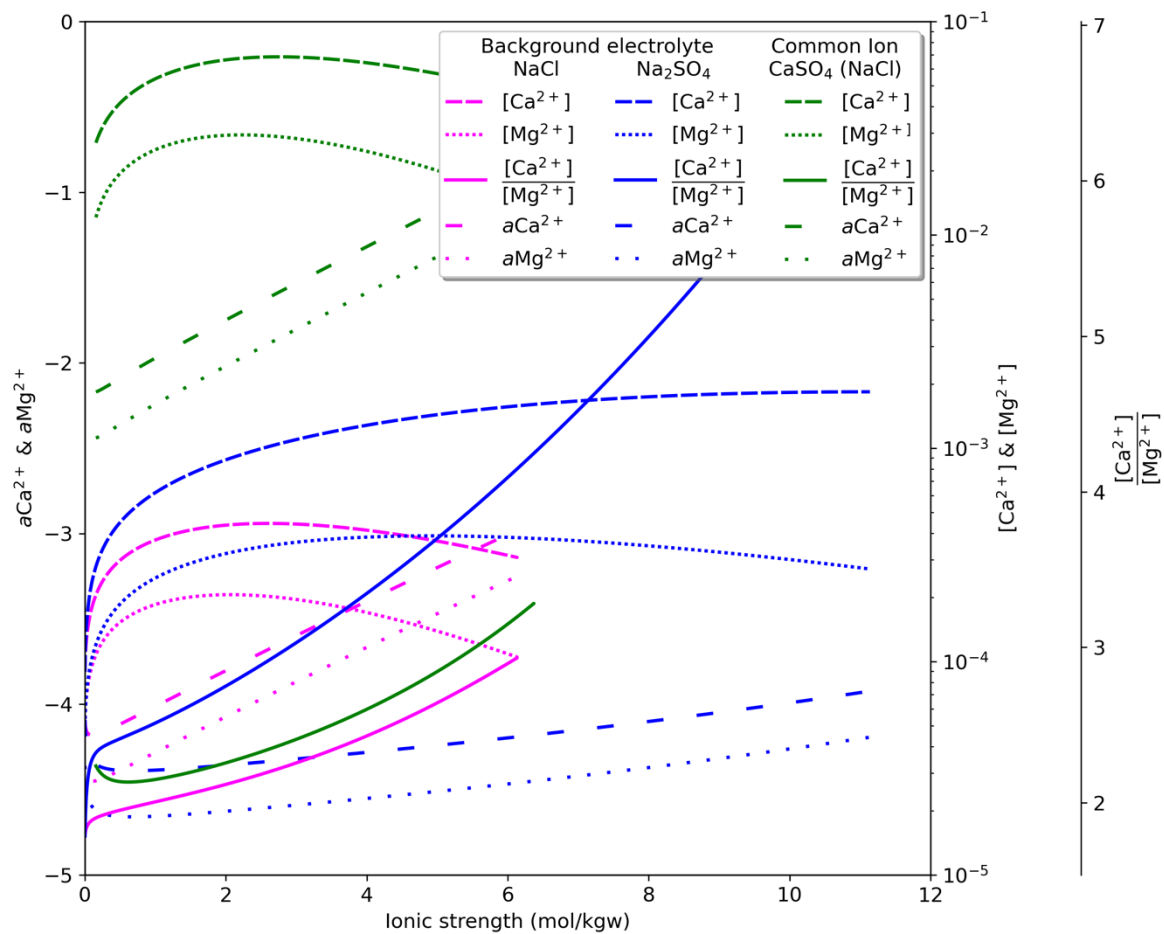
Fig.11
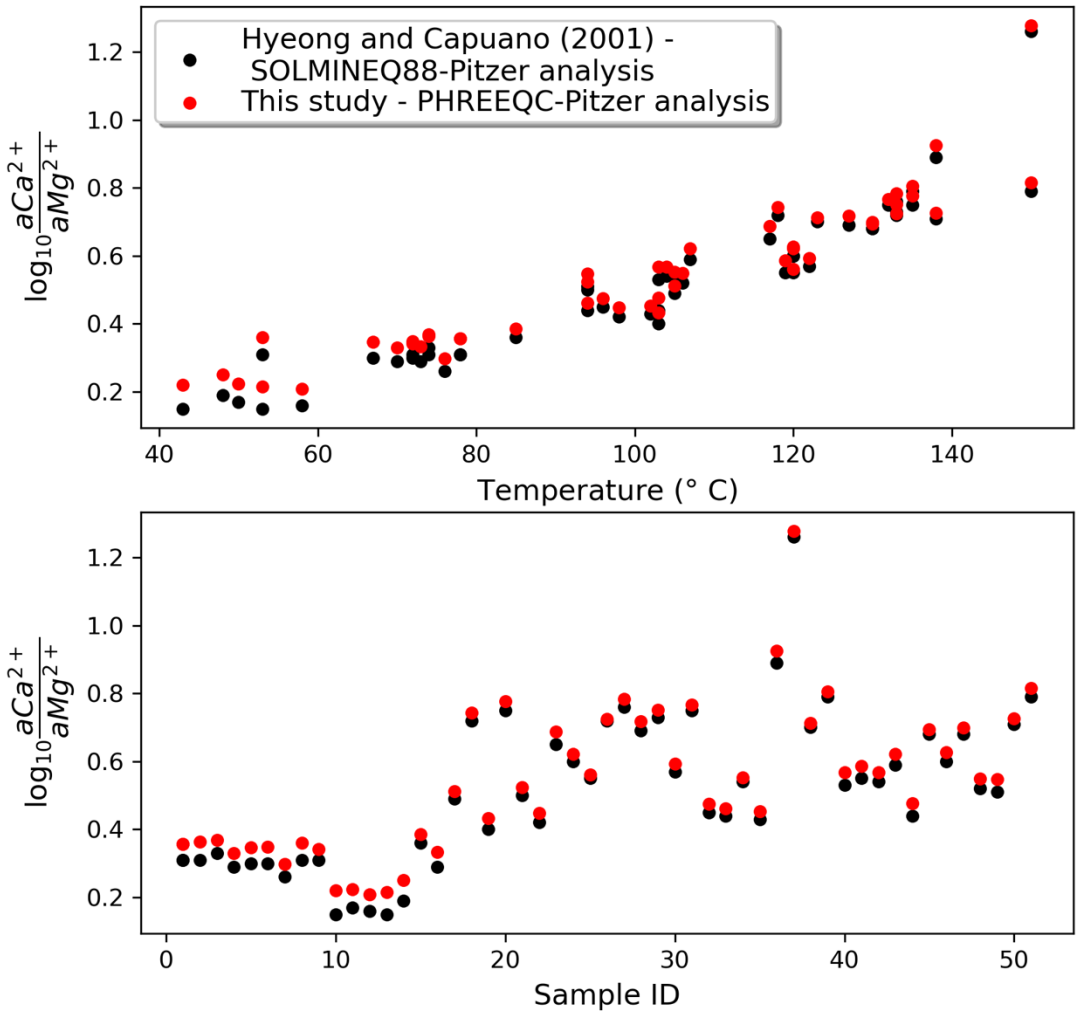
Supplementary Figure.1

Table 1. Reference thermodynamic data for aqueous ions from Plummer and Busenberg (1982), Shock and Helgeson (1988), SUPCRT92-Johnson and others, (1992), Shock and others (1997). a,b,c are Maier-Kelly coefficients.

	Calcite	Magnesite	Mg^{2+}	Ca^{2+}	CO_3^{2-}
$\Delta_f G^{\circ}_{298.15}$ kJ mol^{-1}	-1129	-92.47	-453.98	-552.79	-527.98
$S^{\circ}_{298.15}$ J mol^{-1} K^{-1}	-92.47	-65.69	-138.10	-56.48	-50.00
$\Delta_f H^{\circ}_{298.15}$ kJ mol^{-1}	-1207	-1111	-465.96	-543.08	-675.24
$C^{\circ}_{p\ 298.15}$ J mol^{-1} K^{-1}	82.01	75.73	-21.76	-30.96	-289.53
pK_{sp}	-8.480	-8.035	-	-	-
a(10^0)	24.980	19.731	-	-	-
b (10^3)	5.240	12.539	-	-	-
c (10^{-5})	-6.200	-4.748	-	-	-

Table.2 Model (M#) summaries. H&C – Hyeong and Capuano (2001). M&D – Möller and DeLucia (2020). Type L –linear model; M – mixed model (random intercept model); M(RS) – mixed model (random slope model). Random effects: Fi – field; Fo – Formation; D – depth ; B – basin; L – lithology; P – time-period; S – time-series. MK – Number of Maier-Kelly (fixed effect) terms. *J22 uses ionic strength as fourth fixed effect term. ^J24 β_1 term is fixed to -0.06919.

M#	Dataset - Model	Size	Type	Random	MK	$pK_{sp°-dol}$	AIC
A1	H&C - Literature model	51	L	-	2	-16.92	-
A2	H&C	51	L	-	2	-16.98±0.07	-107.1
A3	H&C	51	M	Fi,Fo	3	-17.25±0.23	-107.4
A4	H&C	51	M	Fi,Fo	2	-16.98±0.20	-84.4
A5	H&C	51	M[1]	Fi,Fo	2	-16.94±0.21	-77.1
B1	H&C - C/H Bayou	35	L	-	2	-16.80±0.18	-
C1	H&C - W.Columbia	16	L	-	2	-17.11±0.08	-
D1	H&C - Frio Fm.	45	L	-	2	-16.92±0.09	-
E1	H&C - Miocene Fm.	6	L	-	2	-17.18±0.41	-
F1	PWGD – Test Area A	21	M	Fi	2	-16.97±0.94	-
G1	PWGD – Frio Fm.	117	M	Fi	2	-17.44±0.84	-
H1	Kharaka and others (1987)	16	L	-	2	-17.52±0.40	-
I1	PWGD – Test Area B	204	M	Fi,Fo	2	-17.34±0.39	-
J1	PWGD	10,343	L	-	3	-17.24±0.36	-1455
J2	PWGD – no interval	10,343	M	D	3	-17.24±0.25	-2754
J3	PWGD – 10m	10,343	M	D	3	-17.24±0.31	-2846
J4	PWGD – 50m	10,343	M	D	3	-17.25±0.34	-3034
J5	PWGD – 100m	10,343	M	D	3	-17.25±0.34	-3086
J6	PWGD – 200m	10,343	M	D	3	-17.25±0.35	-3138
J7	PWGD – 300m	10,343	M	D	3	-17.25±0.36	-3197
J8	PWGD – 400m	10,343	M	D	3	-17.25±0.36	-3147
J9	PWGD – 500m	10,343	M	D	3	-17.25±0.36	-3153
J10	PWGD	10,343	M	Fi	3	-17.24±0.39	-2828
J11	PWGD	10,343	M	B	3	-17.26±0.44	-1815
J12	PWGD	10,343	M	Fo	3	-17.26±0.40	-2640
J13	PWGD	10,343	M	L	3	-17.23±0.45	-1524
J14	PWGD	10,343	M	P	3	-17.24±0.45	-1482
J15	PWGD	10,343	M	S	3	-17.24±0.44	-1501
J16	PWGD	10,343	M	D,Fi	3	-17.25±0.36	-3262
J17	PWGD	10,343	M	D,Fi,Fo	3	-17.26±0.34	-3534
J18	PWGD	10,343	M	D,Fi,Fo,B	3	-17.27±0.35	-3591
J19	PWGD	10,343	M	D,Fi,Fo,B,L	3	-17.27±0.35	-3590
J20	PWGD	10,343	M	D,Fi,Fo,B,L,P	3	-17.27±0.35	-3594
J21	**PWGD**	**10,343**	**M**	**D,Fi,Fo,B,L,P,S**	**3**	**-17.27±0.35**	**-3595**
J22	PWGD	10,343	M	D,Fi,Fo,B,L,P,S	4*	-17.28±0.35	-3600
J23	**PWGD – $pK_{sp°-dol}$ model**	**10,343**	**M**	**D,Fi,Fo,B,L,P,S**	**3**	**-17.27±0.35**	**-3587**
J24	PWGD – $pK_{sp°-dol}$ model	10,343	M	D,Fi,Fo,B,L,P,S	3^	-17.28±0.35	-3562
K1	PWGD	11,480	M	D,Fi,Fo,B,L,P	3	-17.28±0.51	-
K2	PWGD	11,480	M	D,Fi,Fo,B,L,P	3	-17.28±0.51	-
L1	Yarmouk; M&D (2020)	42	L	-	2	-17.19±0.08	-
M1	Yarmouk >25ºC; M&D (2020)	36	L	-	2	-17.17±0.04	-
N1	Bénézeth and others (2018)	28	L	-	3	-17.18±0.53	-

Supplementary Table 1. For selected samples and constants from table 5 of Hsu (1963); a comparison of $K_{sp°-dol}$ values calculated by Hsu (1963) and that recalculated in this study using SUPCRT92 (Johnson and others, 1992). The use of SUPCRT92 $K_{sp°-cal}$ increases the calculated $K_{sp°-dol}$ by 0.38 log units compared to that calculated with the Garrells and Drever (1952) constant. This shifts the $K_{sp°-dol}$ value from -16.69 (Hsu, 1963) to -17.07.

Eq (1) $K_{sp°-dol} = [Ca^{2+}] [\gamma Ca^{2+}] [Mg^{2+}] [\gamma Mg^{2+}] (CO_3^{2-})^2$ (from eq (4) Hsu, 1963). Hsu (1963) determines this $K_{sp°-dol}$ value to demonstrate the effect of loss of CO_2 during sampling, which produces a more soluble (larger) estimate for $K_{sp°-dol}$, and the advantage of assuming calcite-dolomite equilibrium.

Eq (2) $K_{sp°-dol}=[Mg^{2+}] [Ca^{2+}] K_{sp°-cal}{}^2$ ($K_{sp°-cal}= 5.1×10^{-9}$) (from eq (8) Hsu, 1963). Hsu (1963) determines $K_{sp°-dol}$ using the $K_{sp°-cal}$ value from Garrells and Drever (1952) of $5.1×10^{-9}$.

Eq (3) $K_{sp°-dol}=[Mg^{2+}] [Ca^{2+}] K_{sp°-cal}{}^2$ ($K_{sp°-cal} = 3.311×10^{-9}$) This studies calculation of the Hsu (1963) dataset using the $K_{sp°-cal}$ value from Plummer and Busenberg (1982) as implemented in SUPCRT92 (table 1; Johnson and others, 1992).

		Sample		Hsu., (1963) average
		57-28	57-111	
Hsu (1963) observed	$Ca^{2+}×10^{-3}$	5.5	3.35	
	$Mg^{2+}×10^{-3}$	3.69	2.95	
	$CO_3^{2-}×10^{-6}$	1.05	3.0	
Hsu (1963) calculated	Mg:Ca			0.78
	Eq.1	$1.6×10^{-15}$	$5.7×10^{-16}$	
	Eq.2	$1.9×10^{-17}$	$2.3×10^{-17}$	$2.0×10^{-17}$
This study calculated	Eq.2 $pK_{sp°-dol}$	16.73	16.64	16.69
	Eq.3	$7.77×10^{-18}$	$9.65×10^{-18}$	$8.55×10^{-18}$
	Eq.3 $pK_{sp°-dol}$	17.11	17.02	17.07

Supplementary Table 2. Literature reported standard state thermodynamic properties of dolomite and $pK_{sp°-dol}$ values largely compiled from Sherman and Barak (2000) and Bénézeth and others (2018). Minor discrepancies between the two are due mostly to differing methods and reference thermodynamic data sets used during calculation from the sources. We report the original author $pK_{sp°-dol}$, $pK_{sp°-dol}$ values where they differ from those recalculated by Sherman and Barak (2000) or Bénézeth and others (2018), and any recalculations by this study (using reference data from table 1) that represent or entirely new values or significant refinements (**change in $pK_{sp°-dol} > 0.1$**). Estimates for pK_{sp-dol} that are not at reference temperature (25°C) are reported in parentheses. Some entries, such as Robie and Hemingway (1995) and Johnson and others (1992), represent notable significant recalculations of original experimental data (Robie and others (1978) and Helgeson and others (1978) in this case respectively) and multiple studies are listed in the 'authors column' that synthesize and reflect the heritage of the more frequently referenced analyses; the $pK_{sp°-dol}$ value for the most recent study is given in the $pK_{sp°-dol}$ column. Sherman and Barak (2000) present multiple recalculations of $pK_{sp°-dol}$ using different methods/data sources and these are reported here in the order they appear in the original source. Apart from Kramer (1959), unique in using a synthetic seawater composition, experimental solubility is determined using distilled/pure water ('Water') or a solution ('soln.') consisting of a specific electrolyte (e.g. $MgCl_2$).

Authors	Experimental conditions	Thermodynamic results	K_{sp-dol} source	$pK_{sp°-dol}$
Solubility (experimental)				
Yanat'eva (1952) *	25°C, CO_2=0.1 MPa, Water, 100 days, dissolution	$\Delta_f G°_{298.15} = -2161.29$ kJ mol^{-1}	(Ca,Mg & Alk.) Sherman and Barak (2000)[1] Sherman and Barak (2000)[2] (pH & CO_2) Sherman and Barak (2000)[1] Sherman and Barak (2000)[2] Bénézeth and others (2018)	-17.8 -18.4 -18.5 -19.3 -18.37
Kramer (1959)	25°C, CO_2=atmospheric, artificial seawater, variable salinity, dissolution	$K_{sp°-dol} = 1.5 \times 10^{-17}$ ¶	Sherman and Barak (2000)[1] & Bénézeth and others (2018) Sherman and Barak (2000)[2]	-16.8 -17.2
Garrels and others (1960)	25°C, CO_2=0.1 MPa,	$\Delta_f G°_{298.15} = -2175.26$ kJ mol^{-1} from Garrels and others (1960)	(No grind) Sherman and Barak (2000)[1]	-19.3

	Water, 18 hours, dissolution	$\Delta_f G^\circ_{298.15} = -2173.08 \text{ kJ mol}^{-1}$ using table 1 $\Delta_f G^\circ_{298.15} = -2161.7 \text{ kJ mol}^{-1}$ per Bénézeth and others (2018)	Sherman and Barak (2000)[2] Bénézeth and others (2018) (Grind) Sherman and Barak (2000) Bénézeth and others (2018)	-19.4 -19.34 -16.5 -16.44
Rosenberg and Holland (1964)	275-420°C, CaCl$_2$-MgCl$_2$ soln, precipitation & dissolution	$\log_{10}(^aCa^{2+}/^aMg^{2+})$ $= \dfrac{-1000}{T(\text{K})} + 2.98$	This study at 25°C	-16.58
Langmuir (1965) Langmuir (1971)	25°C, Water & MgCl$_2$ soln., dissolution	$\Delta_f H^\circ_{298.15} = -2320.69 \text{ kJ mol}^{-1}$	Langmuir (1965)	-17.0
Halla and Van Tassel (1965)	21°C, CO$_2$=0.1 MPa, Water, 546 days, dissolution		(Ca & Alk.) Sherman and Barak (2000)[1] Sherman and Barak (2000)[2] (pH &CO$_2$) Sherman and Barak (2000)[1] Sherman and Barak (2000)[2] Bénézeth and others (2018)	 -17.0 -17.7 -16.6 -17.5 -17.76
Baker and Kastner (1981)†	200°C, CaCl$_2$-MgCl$_2$ soln., 2 weeks, precipitation	$-0.03 < \log_{10}(^aCa^{2+}/^aMg^{2+}) < 0.26$	This study at 200°C (using $\log\frac{a Ca^{2+}}{a Mg^{2+}}$=0.12)	(-22.21± 0.14)
Stoessell and others (1987)	100-200°C, CaCl$_2$, 300 bars, 7-8 weeks, dissolution	$\log_{10}(^aCa^{2+}/^aMg^{2+})$ 100°C : 1.16 150°C : 1.37 200°C : 1.57	This study at 100°C (using $\log_{10}(^aCa^{2+}/^aMg^{2+})$=-0.35)	(-19.77)
Morrow and others (1994)†	220-240°C, CO$_2$ variable, CaCl$_2$-MgCl$_2$ soln., 300-600 hours, precipitation &	$0.4 < \log\dfrac{a Ca^{2+}}{a Mg^{2+}} < 0.9$	This study at 230°C (using $\log_{10}(^aCa^{2+}/^aMg^{2+})$ =0.65)	(-24.06± 0.25)

	dissolution			
Usdowski (1967), Usdowski (1989), Usdowski (1994)	60-180°C, $CaCl_2$-$MgCl_2$ soln., < 372 weeks, precipitation & dissolution	$\log_{10}(^aCa^{2+}/^aMg^{2+})$ 60°C : -0.35 $\phantom{\log_{10}(^aCa^{2+}/^aMg^{2+})}$ 90°C : 0.49 $\phantom{\log_{10}(^aCa^{2+}/^aMg^{2+})}$ 120°C : 0.83 $\phantom{\log_{10}(^aCa^{2+}/^aMg^{2+})}$ 180°C : 1.08	This study at 60°C (using $\log_{10}(^aCa^{2+}/^aMg^{2+}) = -0.35$)	(-17.25)
Sherman and Barak (2000)	25°C, CO_2=0.101 MPa, Ca-Mg-HCO_3/CO_3 soln., 672 days, dissolution		Sherman and Barak (2000)	-17.2±0.2
Rock and others (2001)	25°C, Cd-Hg electrodes, $CaCl_2$-$MgCl_2$ soln., Electrochemical cell, dissolution	$\Delta_f G^{\circ}_{298.15} = -2147.82$ $\phantom{\Delta_f G^{\circ}_{298.15} =} \pm 2.20 \text{kJ mol}^{-1}$	This study at 25°C	-14.65± 0.39
Gautelier and others (2007)	80°C, HCL-$NaHCO_3$ soln., dissolution		Gautelier and others (2007) at 80°C	(-17.95± 0.1)
Bénézeth and others (2018)	53-253°C, CO_2=variable, NaCl soln. 72-1320 hours precipitation & dissolution	$\Delta_f G^{\circ}_{298.15} = -2160.9$ $\phantom{\Delta_f G^{\circ}_{298.15} =} \pm 2.0 \text{ kJ mol}^{-1}$ $S^{\circ}_{298.15} = 156.9 \pm 2.0 \text{ J mol}^{-1}$ $\Delta_f H^{\circ}_{298.15} = -2323.1$ $\phantom{\Delta_f H^{\circ}_{298.15} =} \pm 2.0 \text{ kJ mol}^{-1}$ $C^{\circ}_{p\,298.15} = 154.2$ $\phantom{C^{\circ}_{p\,298.15} =} \pm 2.0 \text{ J mol}^{-1}\text{ K}^{-1}$	Bénézeth and others (2018) Möller and De Lucia (2020)[1] Möller and De Lucia, (2020)[2] This study statistical reanalysis of activities determined by Bénézeth and others (2018)	-17.19±0.3 -17.8 -17.5 -17.18± 0.53
Debure and others (2021)	Calcite-dolomite equilibrium, NaCl soln., 25°C & 80°C, up to 517 days	$\log_{10}(^aCa^{2+}/^aMg^{2+})$ 25°C : -0.35 $\phantom{\log_{10}(^aCa^{2+}/^aMg^{2+})}$ 80°C : 0.49		

Solubility (groundwater)				
Hsu (1963)	22-27°C (n=28)	Average $\frac{[Ca^{2+}]}{[Mg^{2+}]} = 0.78$	Hsu (1963) Sherman and Barak (2000) This study	-16.7 -17.1 -17.07
Barnes and Back (1964)‡	No temperature reported (presumably 25°C) (n=87)	$K_{sp°-dol} = (2.5 \pm 0.5) \times 10^{-17}$ $K_{sp°-dol} = 2.87 \times 10^{-17}$ $K_{sp°-dol} = 2.89 \times 10^{-17}$	Sherman and Barak (2000) Bénézeth and others (2018) This study	-16.5 -16.54 -16.60±0.09
Hyeong and Capuano (2001) $	43 - 150°C (n=51)	$\Delta_f G°_{298.15} = -2159.15$ kJ mol^{-1} $\Delta_f H°_{298.15} = -2318.77$ kJ mol^{-1} $s = 0.4$ per eqs (129&130) of Helgeson and others (1978)	Hyeong and Capuano (2001)	-16.92
Vespasiano and others (2014) $	60.6°C (chalcedony geothermometer) (n=33)	$\Delta_f G°_{333.75} = -2166.96$ kJ mol^{-1} 22% ordered dolomite per eq (10.2) of Anderson and Crerar (1993)	This study at 61°C	(-18.13)
Blasco and others (2018) $	87°C (combination geothermometer) (n=5)	$\Delta_f G_{360.15} = -2171.75$ kJ mol^{-1} 18.4% ordered dolomite per eq (10.2) Anderson and Crerar (1993)	This study at 87°C	(-18.93)
This study ¢	1.7-254.9°C (n=10,343)	Model J23 $\Delta_f G°_{298.15} = -2161.34 \pm 8.26$ kJ mol^{-1} $\Delta_f H°_{298.15} = -2329.61 \pm 0.51$ kJ mol^{-1} $C°_{p\,298.15} = 82.04 \pm 12.17$ J mol^{-1} K^{-1} Model J24 $\Delta_f G°_{298.15} = -2161.40 \pm 0.66$ kJ mol^{-1} $\Delta_f H°_{298.15} = -2332.67 \pm 0.34$ kJ mol^{-1}	 J24 – fixed $C°_{p\,298.15} = 157.51$ J mol^{-1} K^{-1}	-17.27±0.35 -17.28±0.35
Thermal decomposition				

Rossini and Rossini (1952)*		$\Delta_f G^\circ_{298.15} = -2169.3$ kJ mol^{-1}	Sherman and Barak (2000)	-18.6
Stout and Robie (1963)	Bomb calorimetry	$S^\circ_{298.15} = 155.18$ J mol^{-1} K^{-1} $C^\circ_{p\ 298.15} = 157.53$ J mol^{-1} K^{-1}	Sherman and Barak (2000) Bénézeth and others (2018)	-18.7 -18.2
Karpov and others (1971) *		$\Delta_f G^\circ_{298.15} = -2170.0$ kJ mol^{-1}	Sherman and Barak (2000)	-18.7
Naumov and others (1974) *		$\Delta_f G^\circ_{298.15} = -2151.9$ kJ mol^{-1}§ $\Delta_f G^\circ_{298.15} = -2121.9$ kJ mol^{-1}§	Sherman and Barak (2000)	-15.6
Helgeson and others (1978) SUPCRT92 – slop07.dat Johnson and others (1992)	Method of Navrotsky and Loucks (1977). Using data from Goldsmith and Heard (1961)	Disordered $\Delta_f G^\circ_{298.15} = -2157.49$ kJ mol^{-1} $\Delta_f H^\circ_{298.15} = -2316.70$ kJ mol^{-1} $S^\circ_{298.15} = 166.69$ J mol^{-1} $C^\circ_{p\ 298.15} = 157.74$ J mol^{-1} Ordered(Natural) ¥ $\Delta_f G^\circ_{298.15} = -2166.31$ kJ mol^{-1} $\Delta_f H^\circ_{298.15} = -2328.94$ kJ mol^{-1} $S^\circ_{298.15} = 155.18$ J mol^{-1} $C^\circ_{p\ 298.15} = 157.74$ J mol^{-1}	This study Sherman and Barak (2000) ◆ Bénézeth and others (2018) This study	-16.60 -18.09 -18.15 -18.14
Wagman and others (1982)		$\Delta_f G^\circ_{298.15} = -2163.4$ kJ mol^{-1} $\Delta_f H^\circ_{298.15} = -2326.3$ kJ mol^{-1} $S^\circ_{298.15} = 155.18$ J mol^{-1} $C^\circ_{p\ 298.15} = 157.53$ J mol^{-1}	Sherman and Barak (2000) This study	-17.6 -17.63
Navrotsky and Capobianco (1987) Morrow and others (1994)	HCl solution, 358K	Disordered $\Delta_f G^\circ_{298.15} = -2166.31$ kJ mol^{-1} $\Delta_f H^\circ_{298.15} = -2328.94$ kJ mol^{-1} Ordered $\Delta_f G^\circ_{298.15} = -2167.02$ kJ mol^{-1} $\Delta_f H^\circ_{298.15} = -2315.89$ kJ mol^{-1}	This study This study Sherman and Barak, 2000	-15.82 -18.26 -18.2
Chernosky and		$\Delta_f G^\circ_{298.15} = -2162.4$ kJ mol^{-1}	Sherman and Barak, 2000	-17.4

Berman (1989)				
Knacke and others (1991) *		$\Delta_f H^\circ_{298.15} = -2327.9 \ \text{kJ mol}^{-1}$	Sherman and Barak, 2000	-17.8
Chai and Navrotsky (1993)	PbO-B$_2$O$_3$ melt, 973K	$\Delta_f H^\circ_{298.15} = -2332 \pm 3 \ \text{kJ mol}^{-1}$	Sherman and Barak (2000)	-18.5
Barin (1995)		$\Delta_f G^\circ_{298.15} = -2163.57 \ \text{kJ mol}^{-1}$ $\Delta_f H^\circ_{298.15} = -2326.30 \ \text{kJ mol}^{-1}$ $S^\circ_{298.15} = 155.23 \ \text{J mol}^{-1}$ $C^\circ_{p \ 298.15} = 157.53 \ \text{J mol}^{-1}$	This study Sherman and Barak, 2000	-17.66 -17.6
Robie and others (1978) Hemingway and Robie (1994) Robie and Hemingway (1995)	300.15K, HCl soln.	$\Delta_f G^\circ_{298.15} = -2161.3 \pm 1.7 \ \text{kJ mol}^{-1}$ $\Delta_f H^\circ_{298.15} = -2324.5 \pm 1.6 \ \text{kJ mol}^{-1}$ $S^\circ_{298.15} = 155.2 \ \text{J mol}^{-1}$ $C^\circ_{p \ 298.15} = 157.51 \ \text{J mol}^{-1}\text{K}^{-1}$	Robie and others (1978) & Hemingway and Robie (1994) 1) Sherman and Barak (2000) 2) Sherman and Barak (2000) Bénézeth and others (2018) This study	-17.09±0.37 -17.1 -17.2 -17.12 17.26± 0.3
Database				
Holland and Powell (1990)		$\Delta_f H^\circ_{298.15} = -2325.72 \ \text{kJ mol}^{-1}$ $S^\circ_{298.15} = 155.2 \ \text{J mol}^{-1}$ $C^\circ_{p \ 298.15} = 157.52 \ \text{J mol}^{-1}\text{K}^{-1}$	Sherman and Barak, 2000	-17.4
Holland and Powell (1998)		$\Delta_f G^\circ_{298.15} = -2161.51 \ \text{kJ mol}^{-1}$ $\Delta_f H^\circ_{298.15} = -2324.56 \ \text{kJ mol}^{-1}$ $S^\circ_{298.15} = 156.0 \ \text{J mol}^{-1}$ $C^\circ_{p \ 298.15} = 157.28 \ \text{J mol}^{-1}\text{K}^{-1}$	This Study	-17.30
Blanc and others (2012) Thermoddem v.2017			Dolomite Ordered Dolomite Disordered Dolomite	-17.12 -17.90 -16.35
Miron and others (2017)			New aqueous model using Holland and Powell (1998)	-17.0

			mineral data	

*The original source for Yanat'eva (1952), Rossini and Rossini (1952), Karpov and others (1971), Naumov and others (1974), Knacke and others (1991) were not available and we report the data as sourced from Sherman and Barak (2000) and Bénézeth and others (2018).

¶The data for Kramer (1959) reported by Sherman and Barak (2000) and Bénézeth and others (2018) this study believes is in error, and instead $K_{sp°-dol}=1.5\times10^{-17}$ is reported from the original source.

†Baker and Kastner (1981) and Morrow and others (1994) do not regress the high temperature experimental data to reference state conditions and instead report experimental ranges; a single average value determined by this study is used to represent the $pK_{sp°-dol}$.

‡The value of $K_{sp°-dol}= 2.89 \times 10^{-17}$ reported by Sherman and Barak (2000) appears to be a transcription error. Barnes and Back (1964) present a range ($K_{sp°-dol} = 2\text{-}3 \times 10^{-17}$) over which they interpret $K_{sp°-dol}$. The value $K_{sp°-dol}=2.87 \times 10^{-17}$ represents the maximum ion activity product for dolomite as reported by Barnes and Back (1964) and corresponds to the $pK_{sp°-dol}$ reported by Bénézeth and others (2018).

§There is likely a transcription error on the part of either Sherman and Barak (2000) ($\Delta_f G^°_{298.15} = -2151.9 \text{ kJ mol}^{-1}$) or Bénézeth and others (2018) ($\Delta_f G^°_{298.15} = -2121.9 \text{ kJ mol}^{-1}$).

◆ The $pK_{sp°-dol}$ from Sherman and Barak (2000) uses the original Helgeson and others (1978) thermodynamic properties not reported here.

¢ Reported uncertainties associated with the thermodynamic properties are derived using the standard error otherwise uncertainties associated $pK_{sp°-dol}$ values are computed using 95% confidence intervals.

$ There are two distinct (but related) methods of estimating ordering parameter; a) the standard Helgeson and others (1978) method as used by Hyeong and Capuano (2001) and easily relatable to crystallographic measurements and b) the Anderson and Crerar (1993) % of ordered dolomite method as used by Vespasiano and others (2014) and Blasco and others (2018). However the Anderson and Crerar (1993) method, though initially easier to calculate is not easily converted to *s* values (and is not attempted here as this study discounts the influence of natural dolomite order and favoring dolomite stoichiometry). Equilibrium $\log_{10}(^aCa^{2+}/^aMg^{2+})$ values are higher for both Vespasiano and others (2014) and Blasco and others (2018) compared to Hyeong and Capuano (2001) which classically suggests the presence of a 'more ordered' or, as this study interprets, a more stoichiometric dolomite phase.

¥ - Most databases, such as slop07, have the same properties for the ordered and natural (i.e. just 'Dolomite') phases suggesting the natural (*s*=0.7) phase has fallen out of usage though Blanc and others (2012) preserved a natural dolomite phase which we presume is related to the Helgeson (1978) phase.

Supplementary Table 3. Geochemical and geospatial/other rejection criteria used to filter the PWGD and the rejection criteria used by Hitchon and Brulotte (1994) and Blondes and others (2016). Of the entire database (n=165,960) 93% of all samples failed to meet the criteria specified in this study, leaving a final population of n=11,840. N/A is not applicable; this criteria is not used to discriminate against a sample's inclusion in the dataset.

This study	Failing criteria (%)	Hitchon and Brulotte (1994)	Blondes and others (2016)	Possible causes/Reason for criteria
3.5>pH>11	26.8	5>pH >11	4.5>pH >10.5	Low pH due by acid wash treatment. High pH caused by cement wash or mud filtrate
Charge balance > ±15%	43.1	Charge balance >±15%	Charge balance >±15%	Poor quality analysis or transcription errors
Mg or Ca concentrations missing	22.4	Any of Ca, Mg, Cl or SO4, with either HCO3 or alkalinity, zero, missing, or reported as <or >value	N/A	Incomplete analysis, insufficient sample or very low concentration.
N/A	-	Mg>=Ca	Mg>Ca	Loss of CO^2 (and Ca^{2+} in solution) and precipitation of $CaCO_3$ due to delayed analysis. Low overall concentrations. Incorrect entry of Ca+Mg as equivalent Ca, as separate Ca and Mg values.
N/A	-	OH reported	N/A	Wash from cement. Poor analysis
N/A	-	CO_3 reported	N/A	Drilling mud contamination (without significant effect on pH). Poor sampling of separator or treater.
N/A	-	$(K/Na) \times 10^3$ >stratigraphic unit value	K>Cl or K>5×Na	Contamination by KCl mud
N/A	-	Fe >100mg/l	N/A	Contamination from corrosion products of well
No depth	29.9	N/A	N/A	Must be assignable to a specific depth
No aquifer lithology	84.84	N/A	N/A	Lithologies such as 'other', 'conglomerate', coal (n=33) and anhydrite (n=18) are culled.
No Lat/Lon	7.1	N/A	N/A	Presence of Lat/Lon is required to estimate temperature at formation-depth.

Supplementary Table 4. Classification of samples by lithology. Two datasets are presented; 1) the PWGD dataset (n=11,480) which is simulated using PHREEQC 2) the 90.89% of these samples (n=10,343) with $\log_{10}(^a\text{Ca}^{2+}/^a\text{Mg}^{2+})$ ratios between SUPCRT92-ordered-calcite-dolomite & disordered-dolomite - calcite equilibriums (temperature-dependent) which were used in the principal regression analysis.

Lithology	Description	Pre-SUPCRT (n=11,480)	Post-SUPCRT (n=10,343)
Sandstone	All sand and siltstone lithologies, including those with mention of subsidiary anhydrite and shale. No carbonate can be reported.	7466 (65.0%)	6675 (64.5%)
Dolomite	Dolomite lithologies including those with mention of subsidiary anhydrite, sandstone, siltstone, shale or chert. No limestone can be reported.	1310 (11.4%)	1176 (11.4%)
Limestone	Limestone lithologies including those with mention of subsidiary anhydrite, sandstone, siltstone, shale or chert. No dolomite can be reported.	2045 (17.8%)	1907 (18.4%)
Mixed Carbonate	Dolomite and limestone lithologies including those with mention of subsidiary anhydrite, sandstone, siltstone, shale or chert. Also includes 'carbonate', chalk and chert lithologies.	500 (4.4%)	439 (4.2%)
Shale	Shale lithology. Can mention only 1 other minor lithology e.g. anhydrite, chert	159 (1.4%)	146 (1.4%)

Supplementary Table 5: Summary statistics describing the PWGD dataset (n=11,480), including the number of samples (count), mean value, 1 standard deviation (std), minimum (min) and maximum (max), together with percentiles P25, P50 and P75. Variables denoted by [1] are from the PWGD (Blondes and others, 2016). Geothermal gradients[2] are derived from the interpolation of SMUH dataset (Blackwell and others, 2011). Mean annual land surface temperatures at well sites[3] derive from a reprocessing of the MAST dataset for North America (Bechtel, 2015). Temperature at formation-depth[4] is calculated using the depth, geothermal gradient and the surface temperature. Because of the minimal amount of available pressure data and generally negligible effect on $\log_{10}(^{a}Ca^{2+}/^{a}Mg^{2+})$, this data is excluded from the PHREEQC analysis. Activities and ionic strengths of fluids[5] calculated in this study using by PHREEQC with the Pitzer database are determined at formation-depth temperatures.

	count	mean	std	min	P25	P50	P75	max
Depth[1] (km)	11480	1.955	0.930	0.028	1.301	1.854	2.529	6.779
Geothermal gradient[2] (°C/km)	11480	27.81	6.1	11.0	23.6	27.3	32.0	87.5
Mean Annual Surface Temperature[3] (°C)	11480	7.6	6.4	-5.0	1.0	9.0	13.0	21.0
Temperature at formation-depth[4] (°C)	11480	61.9	29.3	1.7	39.6	57.6	79.0	254.9
Pressure[1] (psi)	188	3504	1417	456	2488	3480	4308	10929
Specific Gravity[1] (g/cm^3)	8233	1.1	0.1	1.0	1.0	1.0	1.1	1.5
Resistivity[1] (S/m)	9057	0.8	1.2	0.0	0.1	0.2	0.9	8.0
pH[1]	11480	7.05	1.1	3.5	6.4	7.1	7.9	11.0
Total dissolved solids[1] (mg/l)	11480	84200	92125	784	9025	42745	140876	409204
Charge Balance (%)[1]	11480	0.3	2.0	-14.9	0.0	0.0	0.0	14.7
Mg[1] (mg/l)	11480	886	1613	1	43	282	1123	26210
Ca[1] (mg/l)	11480	5353	9135	2	196	1280	6160	74200
Ionic Strength[5] (mol/kgw)	11480	2.05	2.57	0.02	0.18	0.85	3.05	13.81
aMg^{2+} [5]	11480	-2.46	1.23	-5.35	-3.39	-2.51	-1.70	2.17
aCa^{2+} [5]	11480	-2.04	1.25	-4.89	-2.94	-2.11	-1.19	2.24

Supplementary Table. 6. For each coefficient estimate (e.g. 'a'); (SE) represents the standard error associated with the estimate. For each coefficient the 't/p' represents; 't' – the t-test associated with the significance of the coefficient estimate and 'p' – the p-value for that t-test. # The intraclass correlation coefficient (ICC) reports the adjusted and conditional ICC. Both ICC values account for all sources of uncertainty but the conditional ICC differs from the adjusted ICC by incorporating the variance associated with the fixed effects; as is common practice we report only the adjusted value. At small sample sizes, using mixed models suffering from singularity in regression analysis, ICC sometimes fails to report. *Reported R^2 values are the marginal (m) and conditional (c) R^2 values for mixed models and the adjusted (a) R^2 for linear models. [†]The lower (l) and upper (u) confidence intervals (CI) are accompanied by a calculation of the difference between them (dif).^For each random effect usually only the $\log_{10}(^{a}Ca^{2+}/^{a}Mg^{2+})$ intercept 'I.' is reported; these are termed random intercept models and the most common type of model used by this study. For random slope models both the intercept 'I.' and also the gradient for the increase in $\log_{10}(^{a}Ca^{2+}/^{a}Mg^{2+})$ with temperature '(G.)' are reported. If a random effect is implemented it is reported; in some cases, e.g. Field for M2, a random effect has zero effect but is still reported as 0.00. For clarity and convenience, the total number of random effects '(RE)' implemented is reported in the brackets for the Model Type. Unless otherwise stated models use a 2,3 or 4 term formulation of the Maier-Kelly regression formulae eq (25) with the total number of terms used reflected by the number of coefficients (a, b, c and d) reported. A1. Original Hyeong and Capuano (2001) model for Hyeong and Capuano (2001) dataset. Activities calculated by SOLMINEQ88-Pitzer and fit to eq (28) (note equation is in celsius-see text). A2. Linear model of the Hyeong and Capuano (2001) dataset with activities calculated using PHREEQC-Pitzer. A3. Three term (fixed effect) mixed model of Hyeong and Capuano (2001) dataset. The model incorporates the field and formation attributes as random effects. This three-term model produces a clearly spurious fit (fig. 5a). A4. Two term (fixed effect) mixed model of Hyeong and Capuano (2001) dataset. A5. A random slope (all others are random intercept) mixed model of the Hyeong and Capuano (2001) dataset.

Model	A1	A2	A3	A4	A5
Model Type (RE)	Linear	Linear	Mixed (2)	Mixed (2)	Mixed (2)
Samples	51	51	51	51	51
a (SE)	-2.20×10^{-1}	-2.01 (1.49×10^{-1})	-1.59×10^{1} (4.00)	-2.37 (2.44×10^{-1})	-2.26 (2.38×10^{-1})
t/p	-	-13.44, $<2.22\times10^{-16}$	-3.97, 1.04×10^{-1}	-9.69, 8.64×10^{-5}	-9.49, 2.00×10^{-1}
b (SE)	7.21	6.80×10^{-3} (3.97×10^{-4})	2.56×10^{-2} (5.36×10^{-3})	7.86×10^{-3} (6.66×10^{-4})	7.53×10^{-3} (6.06×10^{-4})
t/p	-	17.13, $<2.22\times10^{-16}$	4.77, 6.37×10^{-2}	11.80, 2.03×10^{-5}	12.42, 1.01×10^{-4}
c (SE)	-	-	2.56×10^{3} (7.41×10^{2})	-	-
t/p	-	-	3.45, 1.41×10^{-1}	-	-
^Field I.(G.)	-	-	0.00	3.57×10^{-2}	1.93×10^{-1} (4.63×10^{-4})
^Formation I.(G.)	-	-	2.76×10^{-2}	5.91×10^{-2}	8.64×10^{-2} (1.23×10^{-4})
Residual	-	-	7.21×10^{-2}	7.77×10^{-2}	7.76×10^{-2}
#ICC	-	-	-	0.441	-
*R^2 m/c & a	0.94	0.86	0.87/0.88	0.83/0.90	0.85/0.89
$pK_{sp°-dol}$ 25°C	-16.92	-16.98	-17.25	-16.98	-16.94
†CI 25°C l/u (dif)	-	-16.92/-17.05 (0.13)	-17.48/-17.03 (0.45)	-17.15/-16.76 (0.39)	-17.15/-16.73 (0.42)
$pK_{sp°-dol}$ 200°C	-23.32	-23.31	-23.69	-23.45	-23.40
CI 200°C l/u (dif)	-	-23.23/-23.40 (0.17)	-23.95/-23.43 (0.52)	-23.55/-23.15 (0.39)	-23.60/-23.19 (0.41)
AIC	-	-107.1	-107.4	-84.4	-77.1

B1. Model of the Chocolate/Halls Bayou subset from the Hyeong and Capuano (2001) dataset. C1. Model of the West Columbia subset from the Hyeong and Capuano (2001) dataset. D1. Model of the Frio Fm. subset from the Hyeong and Capuano (2001) dataset. E1. Model of the Miocene Fm. subset from the Hyeong and Capuano (2001) dataset. F1. Model of PWGD samples contained within Test Area A (all samples are from the Frio Fm.).

Model	B1	C1	D1	E1	F1
Model Type	Linear	Linear	Linear	Linear	Mixed (1)
Samples	35	16	45	6	21
a (SE)	-2.75 (3.56×10^{-1})	-1.03 (2.81×10^{-1})	-2.28 (1.96×10^{-1})	-5.06×10^{-2} (1.81)	-2.11 (1.55)
t/p	-7.73, 6.62×10^{-9}	-3.65, 2.65×10^{-3}	-11.65, 6.84×10^{-15}	-2.79×10^{-2}, 9.79×10^{-1}	-1.36, 0.21
b (SE)	8.69×10^{-3} (9.08×10^{-4})	3.94×10^{-3} (8.30×10^{-4})	7.51×10^{-3} (5.13×10^{-4})	9.17×10^{-4} (5.60×10^{-3})	7.09×10^{-3} (4.29×10^{-3})
t/p	9.57, 4.82×10^{-11}	4.75, 3.11×10^{-4}	14.65, 2.22×10^{-16}	1.64×10^{-1}, 8.78×10^{-1}	1.65, 1.37×10^{-1}
Field I.(G.)	-	-	-	-	8.02×10^{-2}
Formation I.(G.)	-	-	-	-	-
Residual	8.65×10^{-2}	4.05×10^{-2}	8.01×10^{-2}	6.40×10^{-2}	3.43×10^{-1}
ICC	-	-	-	-	-
R^2 m/c & a	0.74/0.73	0.62/0.59	0.83/0.83	6.66×10^{-3}/-0.24	0.13/0.18
$pK_{sp°-dol}$ 25 °C	-16.80	-17.11	-16.92	-17.18	-16.97
CI 25°C l/u (dif)	-16.63/-16.98 (0.35)	-17.04/17.19 (0.15)	-16.83/17.01 (0.18)	-16.73/-17.59 (0.82)	-16.03/-17.90 (1.87)
$pK_{sp°-dol}$ 200 °C	-23.46	-22.94	-23.37	-22.48	-23.35
CI 200°C l/u (dif)	-23.31/-23.61 (0.31)	-22.70/-23.18 (0.48)	-23.27/-23.47 (0.20)	-20.16/-24.80 (4.64)	-22.12/-24.57 (2.45)
AIC	-	-	-	-	-

G1. Model of all Frio Fm. samples present in PWGD. H1. Model of the Kharaka and others (1987) dataset. I1. Model of all PWGD samples contained within Test Area B.

Model	G1	H1	I1
Model Type	Mixed (2)	Linear	Mixed (2)
Samples	117	16	204
a (SE)	-8.20×10^{-1} (1.01)	4.02×10^{-2} (9.24×10^{-1})	-8.09×10^{-1} (3.04×10^{-1})
t/p	-8.08×10^{-1}, 4.21×10^{-1}	4.35×10^{-2}, 9.66×10^{-1}	-2.66 (9.33×10^{-3})
b (SE)	4.36×10^{-3} (2.84×10^{-3})	1.75×10^{-3} (2.49×10^{-3})	4.00×10^{-3} (8.50×10^{-4})
t/p	1.54, 1.28×10^{-1}	7.05×10^{-1}, 4.92×10^{-1}	4.71, 9.26×10^{-6}
Field I.(G.)	2.63×10^{-1}	-	1.69×10^{-1}
Formation I.(G.)	-	-	1.31×10^{-1}
Residual	3.77×10^{-1}	1.80×10^{-1}	1.82×10^{-1}
ICC	0.328	-	0.579
R^2 m/c & a	0.02/0.34	-0.03	0.19/0.66
$pK_{sp°-dol}$ 25 °C	-17.44	-17.52	-17.34
CI 25°C l/u (dif)	-16.61/-18.27 (1.67)	-17.92/-17.12 (0.80)	-16.96/-17.73 (0.77)
$pK_{sp°-dol}$ 200 °C	-23.34	-22.97	-23.18
CI 200°C l/u (dif)	-22.35/-24.33 (1.98)	-22.41/-23.52 (1.11)	-22.76/-23.60 (0.84)
AIC	-	-	-

J1. Model of SUPCRT92-Filtered PWGD dataset. J2. Model of SUPCRT92-Filtered PWGD utilizing only the depth random effect. No clustering of samples into defined depth ranges. J3. Model of SUPCRT92-Filtered PWGD utilizing only the depth random effect. Samples are clustered into 10m interval depth groups. J4. Model of SUPCRT92-Filtered PWGD utilizing only the depth random effect. Samples are clustered are clustered into 50m interval depth groups. J5. Model of SUPCRT92-Filtered PWGD utilizing only the depth random effect. Samples are clustered into 100m interval depth groups. J6. Model of SUPCRT92-Filtered PWGD utilizing only the depth random effect. Samples are clustered into 200m interval depth groups.

Model	J1	J2 – n=(8201)	J3 – 10m (n=6217)	J4 – 50m (n=4574)	J5 - 100m (n=3985)
Model Type	Linear	Mixed (1)	Mixed (1)	Mixed (1)	Mixed (1)
Samples	10343	10343	10343	10343	10343
a (SE)	-3.76 (4.87×10^{-1})	-3.64 (5.58×10^{-1})	-3.62 (5.97×10^{-1})	-3.65 (6.34×10^{-1})	-3.58 (6.48×10^{-1})
t/p	-7.71, 1.37×10^{-14}	-6.53, 6.93×10^{-11}	-6.07, 1.38×10^{-9}	-5.76, 9.14×10^{-9}	-5.52, 3.52×10^{-8}
b (SE)	8.90×10^{-3} (7.20×10^{-4})	8.72×10^{-3} (8.26×10^{-4})	8.61×10^{-3} (8.85×10^{-4})	8.63×10^{-3} (9.38×10^{-4})	8.52×10^{-3} (9.58×10^{-4})
t/p	1.24×10^{1}, $<2.22 \times 10^{-16}$	1.06×10^{1}, $<2.22 \times 10^{-16}$	9.74, $<2.22 \times 10^{-16}$	9.20, $<2.22 \times 10^{-16}$	8.89, $<2.22 \times 10^{-16}$
c (SE)	4.13×10^{2} (8.21×10^{1})	3.93×10^{2} (9.37×10^{1})	3.99×10^{2} (1.00×10^{2})	4.07×10^{2}, 1.07×10^{2}	3.96×10^{2} (1.09×10^{2})
t/p	5.03, 4.89×10^{-7}	4.19, 2.79×10^{-5}	3.98, 7.05×10^{-5}	3.82, 1.37×10^{-4}	3.63, 2.86×10^{-4}
Depth I.(G.)	-	1.91×10^{-1}	1.71×10^{-1}	1.62×10^{-1}	1.55×10^{-1}
Residual	2.25×10^{-1}	1.26×10^{-1}	1.57×10^{-1}	1.70×10^{-1}	1.76×10^{-1}
ICC	-	0.696	0.541	0.474	0.439
R^2 m/c & a	0.30/0.30	0.29/0.79	0.28/0.67	0.27/0.61	0.27/0.59
$pK_{sp°-dol}$ 25 °C	-17.24	-17.24	-17.24	-17.25	-17.25
CI 25°C l/u (dif)	-16.89/-17.60 (0.71)	-16.99/-17.48 (0.50)	-16.94/-17.56 (0.62)	-16.91/-17.59 (0.67)	-16.90/-17.59 (0.68)
$pK_{sp°-dol}$ 200 °C	-23.42	-23.41	-23.40	-23.39	-23.39
CI 200°C l/u (dif)	-22.99/-23.72 (0.72)	-23.16/-23.67 (0.51)	-23.08/-23.71 (0.63)	-23.05/-23.73 (0.68)	-23.03/-23.74 (0.71)
AIC	-1455.3	-2754.0	-2845.5	-3034.2	-3085.8

J7. Model of SUPCRT92-Filtered PWGD dataset. Samples are clustered into 300m interval depth groups. J8. Model of SUPCRT92-Filtered PWGD dataset. Samples are clustered into 400m interval depth groups. J9. Model of SUPCRT92-Filtered PWGD dataset. Samples are clustered into 500m interval depth groups.

Model	J6 - 200m (n=3544)	J7 - 300m (n=3296)	J8 - 400m (n=3175)	J9 - 500m (n=3040)
Model Type	Mixed (1)	Mixed (1)	Mixed (1)	Mixed (1)
Samples	10343	10343	10343	10343
a (SE)	-3.78 (6.64×10^{-1})	-3.64 (6.76×10^{-1})	-3.70 (6.80×10^{-1})	-3.61 (6.81×10^{-1})
t/p	-5.69, 1.35×10^{-8}	-5.38, 7.87×10^{-8}	-5.44, 5.66×10^{-8}	-5.30, 1.21×10^{-7}
b (SE)	8.81×10^{-3} (9.82×10^{-4})	8.57×10^{-3} (1.00×10^{-3})	8.66×10^{-3} (1.00×10^{-3})	8.53×10^{-3} (1.00×10^{-3})
t/p	8.98, $<2.22\times10^{-16}$	8.58, $<2.22\times10^{-16}$	8.62, $<2.22\times10^{-16}$	8.47, $<2.22\times10^{-16}$
c (SE)	4.29×10^{2} (1.12×10^{2})	4.09×10^{2} (1.14×10^{2})	4.19×10^{2} (1.14×10^{2})	4.05×10^{2} (1.15×10^{2})
t/p	3.84, 1.23×10^{-4}	3.59, 3.34×10^{-4}	3.66, 2.51×10^{-4}	3.53, 4.22×10^{-4}
Depth I.(G.)	1.52×10^{-1}	1.51×10^{-1}	1.49×10^{-1}	1.47×10^{-1}
Residual	1.78×10^{-1}	1.80×10^{-1}	1.82×10^{-1}	1.83×10^{-1}
ICC	0.418	0.411	0.400	0.393
R^2 m/c & a	0.27/0.57	0.26/0.57	0.26/0.56	0.26/0.55
$pK_{sp°-dol}$ 25 °C	-17.25	-17.25	-17.25	-17.25
CI 25°C l/u (dif)	-16.89/-17.60 (0.70)	-16.90/-17.61 (0.71)	-16.89/-17.61 (0.72)	-16.89/-17.61 (0.72)
$pK_{sp°-dol}$ 200 °C	-23.40	-23.38	-23.38	-23.38
CI 200°C l/u (dif)	-23.04/-23.75 (0.72)	-23.02/-23.74 (0.72)	-23.02/-23.74 (0.73)	-23.01/-23.75 (0.74)
AIC	-3137.9	-3196.5	-3147.0	-3152.6

J10. Model of SUPCRT92-Filtered PWGD dataset. Only the field random effect is used. J11. Model of SUPCRT92-Filtered PWGD dataset. Only the basin random effect is used. J12. Model of SUPCRT92-Filtered PWGD dataset. Only the formation random effect is used J13. Model of SUPCRT92-Filtered PWGD dataset. Only the lithology random effect is used. J14. Model of SUPCRT92-Filtered PWGD dataset. Only the time-period random effect is used.

Model	J10	J11	J12	J13	J14
Model Type	Mixed (1)	Mixed (1)	Mixed (1)	Mixed (1)	Mixed (1)
Samples	10343	10343	10343	10343	10343
a (SE)	-2.98 (6.16×10^{-1})	-2.88 (5.07×10^{-1})	-1.89 (5.37×10^{-1})	-3.88 (4.89×10^{-1})	-3.68 (4.87×10^{-1})
t/p	-4.83, 1.43×10^{-6}	-5.68, 1.42×10^{-8}	-3.52, 4.32×10^{-4}	-7.94, 2.18×10^{-15}	-7.55, 4.82×10^{-14}
b (SE)	7.57×10^{-3} (9.14×10^{-4})	7.52×10^{-3} (7.49×10^{-4})	5.71×10^{-3} (7.95×10^{-4})	9.03×10^{-3} (7.21×10^{-4})	8.77×10^{-3} (7.21×10^{-4})
t/p	8.29, $<2.22\times10^{-16}$	1.00×10^{1}, $<2.22\times10^{-16}$	7.18, 7.40×10^{-13}	1.25×10^{1}, $<2.22\times10^{-16}$	1.22×10^{1}, $<2.22\times10^{-16}$
c (SE)	2.98×10^{2} (1.04×10^{2})	2.79×10^{2} (8.54×10^{1})	1.47×10^{2} (9.04×10^{1})	4.36×10^{2} (8.23×10^{1})	4.00×10^{2} (8.21×10^{1})
t/p	2.88, 4.02×10^{-3}	3.27, 1.09×10^{-3}	1.62, 1.04×10^{-1}	5.29, 1.23×10^{-7}	4.88, 1.09×10^{-6}
Basin I.(G.)	-	6.99×10^{-1}	-	-	-
Field I.(G.)	1.27×10^{-1}	-	-	-	-
Formation I.(G.)	-	-	1.29×10^{-1}	-	-
Lithology I.(G.)	-	-	-	3.48×10^{-2}	-
Series I.(G.)	-	-	-	-	-
Period I.(G.)	-	-	-	-	2.25×10^{-2}
Residual	1.95×10^{-1}	2.20×10^{-1}	2.03×10^{-1}	2.24×10^{-1}	2.25×10^{-1}
ICC	0.297	0.091	0.288	0.024	0.010
R^2 m/c & a	0.26/0.48	0.27/0.34	0.21/0.44	0.29/0.31	0.30/0.31
$pK_{sp°-dol}$ 25 °C	-17.24	-17.26	-17.26	-17.23	-17.24
CI 25°C l/u (dif)	-16.86/-17.62 (0.77)	-16.83/-17.69 (0.87)	-16.86/-17.66 (0.80)	-16.79/-17.68 (0.89)	-16.79/-17.68 (0.89)
$pK_{sp°-dol}$ 200 °C	-23.34	-23.37	-23.22	-23.41	-23.41
CI 200°C l/u (dif)	-22.95/-23.72 (0.77)	-22.94/-23.81 (0.87)	-22.82/-23.61 (0.79)	-22.97/-23.86 (0.89)	-22.97/-23.86 (0.89)
AIC	-2828.3	-1815.0	-2639.5	-1524.2	-1481.8

J15. Model of SUPCRT92-Filtered PWGD dataset. Only the time-series random effect is used. J16. Model of SUPCRT92-Filtered PWGD dataset. The depth (300m interval) and the field random effects are used. J17. Model of SUPCRT92-Filtered PWGD dataset. The depth (300m interval), field, and formation random effects are used. J18. Model of SUPCRT92-Filtered PWGD dataset. The depth (300m interval), field, formation, and basin random effects are used. J19. Model of SUPCRT92-Filtered PWGD dataset. The depth (300m interval), field, formation, basin and lithology random effects are used.

Model	J15	J16	J17	J18	J19
Model Type	Mixed (1)	Mixed (2)	Mixed (3)	Mixed (4)	Mixed (5)
Samples	10343	10343	10343	10343	10343
a (SE)	-3.59 (4.91×10^{-1})	-3.33 (6.88×10^{-1})	-2.31 (6.97×10^{-1})	-1.86 (7.19×10^{-1})	-1.89 (7.19×10^{-1})
t/p	-7.31, 2.87×10^{-13}	-4.85, 1.29×10^{-6}	-3.31, 9.49×10^{-4}	-2.59, 9.74×10^{-3}	-2.62, 8.79×10^{-3}
b (SE)	8.65×10^{-3} (7.25×10^{-4})	8.11×10^{-3} (1.02×10^{-3})	6.42×10^{-3} (1.03×10^{-3})	5.77×10^{-3} (1.06×10^{-3})	5.81×10^{-3} (1.06×10^{-3})
t/p	1.92×10^{1}, $<2.22\times10^{-16}$	7.97, 2.20×10^{-15}	6.21, 5.88×10^{-10}	5.43, 6.09×10^{-8}	5.47, 4.93×10^{-8}
c (SE)	3.85×10^2 (8.27×10^2)	3.59×10^2 (1.16×10^2)	2.07×10^2 (1.17×10^2)	1.33×10^2 (1.21×10^2)	1.37×10^2 (1.21×10^2)
t/p	4.65, 3.29×10^{-6}	3.10, 1.94×10^{-3}	1.76, 7.78×10^{-2}	1.10, 2.73×10^{-1}	1.13, 2.57×10^{-1}
Depth I.(G.)	-	1.21×10^{-1}	1.09×10^{-1}	1.09×10^{-1}	1.09×10^{-1}
Field I.(G.)	-	8.86×10^{-2}	6.90×10^{-2}	6.98×10^{-2}	6.97×10^{-2}
Formation I.(G.)	-	-	9.12×10^{-2}	7.70×10^{-2}	7.68×10^{-2}
Basin I.(G.)	-	-	-	6.14×10^{-2}	6.17×10^{-2}
Lithology I.(G.)	-	-	-	-	8.53×10^{-3}
Series I.(G.)	3.39×10^{-2}	-	-	-	-
Period I.(G.)	-	-	-	-	-
Residual	2.24×10^{-1}	1.80×10^{-1}	1.77×10^{-1}	1.77×10^{-1}	1.77×10^{-1}
ICC	0.022	0.409	0.445	0.459	0.459
R^2 m/c & a	0.30/0.31	0.26/0.56	0.23/0.57	0.22/0.58	0.22/0.58
$pK_{sp°-dol}$ 25 °C	-17.24	-17.25	-17.26	-17.27	-17.27
CI 25°C l/u (dif)	-16.80/-17.68 (0.87)	-16.89/-17.60 (0.71)	-16.92/-17.60 (0.68)	-16.92/-17.62 (0.69)	-16.92/-17.61 (0.70)
$pK_{sp°-dol}$ 200 °C	-23.41	-23.36	-23.26	-23.25	-23.25
CI 200°C l/u (dif)	-22.97/-23.86 (0.89)	-22.99/23.72 (0.72)	-22.91/-23.63 (0.72)	-22.90/-23.60 (0.71)	-22.89/-23.61 (0.72)
AIC	-1501.2	-3261.5	-3533.8	-3590.9	-3589.7

J20. Model of SUPCRT92-Filtered PWGD dataset. The depth (300m interval), field, formation, basin, lithology and time-period random effects are used. J21. Model of SUPCRT92-Filtered PWGD dataset. The depth (300m interval), field, formation, basin, lithology, time-period and time-series random effects are used. This is the reference model for the relationship between $\log_{10}(^aCa^{2+}/^aMg^{2+})$-temperature for the PWGD. J22. Model of SUPCRT92-Filtered PWGD dataset with ionic strength included as a fixed effect. The same 7 random effects used in model J21 used here. J23. Model of $pK_{sp°-dol}$ values calculated for SUPCRT92-Filtered PWGD dataset. Statistical goodness of fit functions (AIC, R^2) and t/p values are thought to be somewhat spurious due to the pre-modelling conversion to $pK_{sp°-dol}$. The same 7 random effects used in model J22 used here. J24. Model of $pK_{sp°-dol}$ values calculated for SUPCRT92-Filtered PWGD dataset where the b term is fixed to -0.06919. The same 7 random effects used in model J22 used here. There appears to be an unresolvable bug in how R calculates confidence intervals for offset models, with the width of the interval which appear to be reliable but not the absolute values (which are significantly incorrect).

Model	J20	J21	J22	J23 - $pK_{sp°-dol}$	J24 - $pK_{sp°-dol}$
Model Type	Mixed (6)	Mixed (7)	Mixed (7)	Mixed (7)	Mixed (7)
Samples	10343	10343	10343	10343	10343
a (SE)	-1.94 (7.21×10^{-1})	-1.91 (7.21×10^{-1})	-1.86 (7.21×10^{-1})	1.47545×10^{1} (7.22×10^{-1})	1.93×10^{1} (5.67×10^{-2})
t/p	-2.70, 7.07×10^{-3}	-2.65, 8.16×10^{-3}	-2.58, 9.84×10^{-3}	2.04×10^{1}, $<2.22\times10^{-16}$	339.6, $<2.22\times10^{-16}$
b (SE)	5.89×10^{-3} (1.06×10^{-3})	5.84×10^{-3} (1.07×10^{-3})	5.85×10^{-3} (1.07×10^{-3})	-6.24959×10^{-2} (1.07×10^{-4})	-6.919×10^{-2} (fixed value)
t/p	5.53, 3.42×10^{-8}	5.49, 4.44×10^{-8}	5.49, 4.32×10^{-8}	-5.86×10^{1}, $<2.22\times10^{-16}$	-
c (SE)	1.47×10^{2} (1.21×10^{2})	1.41×10^{2} (1.21×10^{2})	1.31×10^{2} (1.21×10^{2})	-3.99350×10^{3} (1.22×10^{2})	-4.75×10^{3} (1.75×10^{1})
t/p	1.21, 2.26×10^{-1}	1.16, 2.46×10^{-1}	1.08, 2.82×10^{-1}	-3.29×10^{1}, $<2.22\times10^{-16}$	270.7, $<2.22\times10^{-16}$
Ionic strength (SE)	-	-	-7.14×10^{-3} (1.49×10^{-3})	-	-
t/p	-	-	-4.79, 1.68×10^{-6}	-	-
Depth I.(G.)	1.09×10^{-1}	1.09×10^{-1}	1.10×10^{-1}	1.10×10^{-1}	1.12×10^{-1}
Basin I.(G.)	6.30×10^{-2}	6.35×10^{-2}	6.40×10^{-2}	6.47×10^{-2}	6.22×10^{-2}
Field I.(G.)	6.99×10^{-2}	7.01×10^{-2}	6.86×10^{-2}	6.94×10^{-2}	6.90×10^{-2}
Formation I.(G.)	7.65×10^{-2}	7.66×10^{-2}	7.67×10^{-2}	7.70×10^{-2}	7.66×10^{-2}
Lithology I.(G.)	8.86×10^{-3}	8.05×10^{-3}	9.80×10^{-3}	7.77×10^{-3}	9.33×10^{-3}
Series I.(G.)	-	1.70×10^{-2}	1.74×10^{-2}	1.70×10^{-2}	1.66×10^{-2}
Period I.(G.)	1.80×10^{-2}	1.38×10^{-2}	1.44×10^{-2}	1.36×10^{-2}	1.35×10^{-2}
Residual	1.77×10^{-1}	1.76×10^{-1}	1.76×10^{-1}	1.76×10^{-1}	1.76×10^{-1}
ICC	0.464	0.466	0.469	0.469	0.467
R^2 m/c & a	0.22/0.58	0.22/0.58	0.21/0.58	0.91/0.95	0.96/0.98
$pK_{sp°-dol}$ 25°C	-17.27	-17.27	-17.28	-17.27	-17.28
CI 25°C l/u (dif)	-16.92/-17.61 (0.69)	-16.92/-17.62 (0.70)	-16.93/-17.62 (0.69)	-16.93/-17.62 (0.69)	(0.69)
$pK_{sp°-dol}$ 200°C	-23.25	-23.25	-23.28	-23.26	-23.50

| CI 200°C l/u (dif) | -22.90/-23.61 (0.72) | -22.89/-23.61 (0.72) | -22.92/-23.63 (0.71) | -22.90/-23.61 (0.71) | (0.69) |
| AIC | -3593.6 | -3595.4 | -3599.8 | -3587.1 | -3562.0 |

K1. Model of PWGD database not filtered using the SUPCRT92-Filter. The model (and K2) are unable to reliably calculate the time series random effect term so it is omitted. K2. Model of $pK_{sp°-dol}$ values for the PWGD database with values not filtered using the SUPCRT92-Filter. L1. Model of Yarmouk gorge samples from Möller and De Lucia (2020) dataset; samples are taken from Siebert and others (2014) and Siebert and others (in prep). The p-value of this model is 7.73×10^{-2} (identical also to p value on the b-term). We do not report model p-values as they are only output for linear models. The p-values given(reported t/p) are those that describe the significance of model coefficients. M1. Model of Yarmouk gorge samples from Möller and De Lucia (2020) without samples <25°C. The p-value for this model is 4.23×10^{-5} (again identical to the to p value on the b-term). N1. Reanalysis of the Bénézeth and others (2018) dataset using activities calculated by Bénézeth and others (2018).

Model	K1	K2 - $pK_{sp°-dol}$	L1	M1	N1
Model Type	Mixed (6)	Mixed (6)	Linear	Linear	Linear
Samples	11480	11480	42	36	28
a (SE)	8.31×10^{-1} (9.07×10^{-1})	1.19×10^{1} (9.09×10^{-1})	-1.01 (7.07×10^{-1})	-1.22 (3.21×10^{-1})	-1.74×10^{1} (5.25)
t/p	9.17×10^{-1}, 3.59×10^{-1}	1.31×10^{1}, $<2.22\times10^{-16}$	-1.42, 1.63×10^{-1}	-3.79, 5.93×10^{-4}	3.33, 2.70×10^{-3}
b (SE)	1.18×10^{-3} (1.33×10^{-3})	-5.76×10^{-2} (1.33×10^{-3})	4.13×10^{-3} (2.28×10^{-3})	4.82×10^{-3} (1.03×10^{-3})	-6.88×10^{-2} (6.36×10^{-3})
t/p	8.88×10^{-1}, 3.75×10^{-1}	-4.34×10^{1}, $<2.22\times10^{-16}$	1.81, 7.73×10^{-2}	4.70, 4.23×10^{-5}	-1.08×10^{1}, 6.37×10^{-11}
c (SE)	-2.58×10^{2} (1.54×10^{2})	-3.58×10^{3} (1.54×10^{2})	-	-	-4.22×10^{3} (1.07×10^{3})
t/p	-1.68, 9.34×10^{-2}	-2.32×10^{1}, $<2.22\times10^{-16}$	-	-	-3.95, 5.66×10^{-4}
Depth I.(G.)	1.38×10^{-1}	1.39×10^{-1}	-	-	-
Field I.(G.)	1.30×10^{-1}	1.30×10^{-1}	-	-	-
Formation I.(G.)	1.00×10^{-1}	1.00×10^{-1}	-	-	-
Basin I.(G.)	8.29×10^{-2}	8.54×10^{-2}	-	-	-
Lithology I.(G.)	2.43×10^{-2}	2.39×10^{-2}	-	-	-
Period I.(G.)	1.30×10^{-1}	1.28×10^{-2}	-	-	-
Residual	2.56×10^{-1}	2.56×10^{-1}	1.65×10^{-1}	5.78×10^{-2}	0.29
ICC	0.449	0.452	-	-	-
R^2 m/c & a	0.08/0.49	0.84/0.91	0.05	0.38	0.99
$pK_{sp°-dol}$ 25°C	-17.28	-17.28	-17.19	-17.17	-17.18
CI 25°C l/u (dif)	-16.77/-17.78 (1.00)	-16.78/-17.79 (1.00)	-17.11/-17.26 (0.15)	-17.14/-17.22 (0.07)	-16.66/-17.71 (0.53)
$pK_{sp°-dol}$ 200 °C	-22.94	-22.94	-23.05	-23.16	-24.00
CI 200°C l/u (dif)	-22.43/-23.47 (1.04)	-22.42/-23.47 (1.05)	-22.30/-23.80 (0.72)	-22.83/-23.50 (-0.67)	-23.85/-24.15 (0.15)
AIC	-	-	-	-	-